Studies on structure, microstructure, mechanical, optical and transport properties of sub-stoichiometric and Nb-substituted nanostructured Titanium Nitride thin films

By
K. Vasu

Thesis submitted to

UNIVERSITY OF HYDERABAD

in partial fulfillment of the requirements

for the degree of

DOCTOR OF PHILOSOPHY

in

PHYSICS

School of Physics

University of Hyderabad

Hyderabad, 500046

INDIA

May 2012

DECLARATION

I hereby declare that the content embodied in this thesis entitled **"Studies on structure, microstructure, mechanical, optical and transport properties of sub-stoichiometric and Nb-substituted nanostructured Titanium Nitride thin films"** submitted to University of Hyderabad for the award of **Doctor of Philosophy in Physics** is a record of original research work carried out by me under the supervision of **Dr M. Ghanashyam Krishna**, School of Physics, University of Hyderabad, Hyderabad. This work has not been submitted partially or fully for any degree in any other university.

Date: K. Vasu
Station: Hyderabad

CERTIFICATE

This is to certify that the research work presented in this thesis entitle **"Studies on structure, microstructure, mechanical, optical and transport properties of sub-stoichiometric and Nb-substituted nanostructured Titanium Nitride thin films"** for the award of **DOCTOR OF PHILOSOPHY** is an original work carried out by **Mr. K. Vasu** under my supervision at school of Physics, University of Hyderabad, Hyderabad. This thesis work has not been submitted to this or any other university partially or fully for the award of any degree or diploma.

Date: Dr M. Ghanashyam Krishna
Station: Hyderabad   (Thesis supervisor)

Dean
School of Physics

DEDICATED.......

TO MY COUNTRY

Acknowledgements

It's my pleasure to write this part of my thesis and express my gratitude to one and all for helping me in a long run. Many people have directly or indirectly contributed to the successfully completion of this thesis and I thank all of them.

First of all, I would like to express my deepest gratitude and admiration to my supervisor, **Dr M. Ghanashyam Krishna** for his guidance and support throughout my research. I am deeply indebted to him for his guidance, patience and encouragement. The way he has guided me has improved my ability of understanding the concepts of the problems. Without his valuable discussions and objective criticism I would not have been able to complete this task. Everything I know about research has come from him. The facilities, freedom he has given me to work is ultimate and unlimited and I hope that it was utilized in a proper way.

I am very happy to say an Eminent Scientist and National Metallurgist Prof. **K.A.Padmanabhan,** Chair Professor, School of Engineering Science and Technology (SEST). I express my sincere thanks to him for giving me an opportunity to work with him. The way he encouraged and inspired me is unforgettable ever.

N. K. Viswanathan, Dr. Surajit Dhara and **Dr. V. Ashoka** for excelent tecahing.

I thank **all faculty** from School of Physics

I thank **Mr. T. Abraham**, School of Physics and **Ms. Grace**, Centre for nanotechnology for his timely help and encouragement on every occasion. I also thank all non-teaching staff from School of Physics and N.R.S hostel.

I thank all the Central Instrumentation Lab staff and all Science Complex workshop staff. I also thank technical staff from School of Physics and Centre for Nanotechnology namely **Mr. Lakshmi Narayana** (FE-SEM), **Mr. Tirumalaiah** (GI-XRD), **Mr. Ravi Sankar** (XRD) **Mr. Durga Prasad** (TEM) and **B. Sandhya** (Surface profilometer) for their help in obtaing data from various instruments.

The hepl from my seniors namely **Dr. K. Uma Mahindra Kumar, Dr. M. S. R. N. Kiran, Dr. Prasanth Kumar, Dr. Rajeeb Brahma, Dr. D. Pamu, Dr. K. Sudheendran, Dr. K.Venkata Saravanan** is greatly acknowledged. Their valueble discussion/suggestions in the lab made easy of analyzing the data and writing manuscripts and thesis as well.

I thank postdoctoral fellows in thin films laboratory **Dr. K. D. Sachin**, **Dr. Ahmed Mohiuddin** and **Dr. Prashanth S. Vachhani** for their help in academic issues.

I feel happy to have nice working labmates **Mr. K. Lakshmi Narayana, Mr. A. Rambabu, Mr. K. Lakshun Naidu, Mr. S. Ramakanth, Mr. K. Rama Obulesu, Mr. T. Anil, Mr. S. Bashaiah, Mr. Sk. Umar Pasha, Mr. Varma, Mr. M. Sandeep Kumar, Mr. Sankarnath, Mr. G.M. Gopikrishnana and Mr. V. Santosh** for helping me in various academic and personal issues.

I thank all my 2006 bathmates namely Mr. B. Yugandar, Mr. N. Sankaraiah, Mr. A. Rambabu, Mr. M. Venkaiah, Mr. D. Vijayan, Mr. Anil, Mr. A. Sendil Kumar, Mr. R. Parthasarathy, Dr. K. L. N. Deepak, Dr. G. Devaraju, Mr. T. Arun Kumar, Mr. Bheemalingam, Mr. Sadik Ali, Ms. B. Sita lakshmi, Y. Balaji and P. Rangababu.

I thank all research scholars from School of Physics

I thank M.Sc friends from Andhra University Mr. M. Balamurali Krishna, Mr. Anjeneyulu, Mr. K. Ramesh Babu, Mr. G. Srinivasa Rao, Mr. A. Rambabu, Ch. Rajasekhar, Dr. K. Koteswara Rao, Dr. T. Bhaskra Rao, Mr. D. Kishor, Mr. R. Girish Kumar, Mr. Venumadhav, Mr. Praveen, Ms. Kavitha and Ms. N. Sujatha

I express my sincere thank all my relatives and friends S. Shanmuk rao, K.Narayana Swamy, T. Vamsi, N. Sailaja, Prasad for their help and encouragment for the completion of my thesis.

CONTENTS

2.2   Characterization

CHAPTER-3: Ti AND TiN THIN FILMS

**CHAPTER-4: SUB-STOICHIOMETRIC
TITANIUM NITRIDE THIN FILMS**

**CHAPTER-5: Nb-SUBSTITUTED
TITANIUM NITRIDE THIN FILMS**

CHAPTER-6: CONDUCTIVE-ATOMIC FORCE MICROSCOPY STUDY ON TiN_x AND $Ti_{1-x}Nb_xN$ THIN FILM

CHAPTER-7: SUMMARY AND SCOPE FOR FUTURE WORK

CHAPTER-1

INTRODUCTION

Abstract

This chapter presents the various applications and physical properties of stoichiometric and sub-stoichiometric titanium nitride thin films. From the literature study, the formation and stability of various metal-substituted TiN thin films are discussed. Motivation and objectives of the research work and then finally the outline of the thesis is presented, including a brief summary of the contents therein.

1.1 Background

Thin films find application in a diverse range of technologies that includes electronic, optical, photonic, semiconductor, tribology, and medical applications. The advent of nanoscience and technology has further increased the range of applications of thin films. One of the more important applications of thin films are in the areas of tribology, enhanced protection of bulk materials in harsh environments and increasing the life time of mechanical components. Material systems generally employed for such applications are based on metal oxides, metal carbides, metal borides and metal nitrides. A recurring theme in thin film work is the multi-functionality of a given material. The current thesis focuses on the growth of sub-stoichiometric and metal-substituted titanium nitride thin films and demonstrating their use in mechanical, optical, optoelectronic and electronic applications, thus establishing the multifunctional nature of the material.

1.2 Titanium nitride

Binary transition metal nitrides (MeN, Me = Ti, Zr, Hf, V, Nb, Ta, Cr ………etc.) are known as refractory compounds with major interest as functional coatings in surface engineering applications. Thin films of these transition nitrides (TMN) are the subject of intense studies both theoretically and experimentally. TiN is regarded as a prototype transition-metal nitride system that has received by far the most attention [1-2]. TiN thin film exhibits a unique combination of properties like high hardness, high wear resistance, high melting point, good chemical inertness and gold-like color. These properties are a consequence of the

complex chemical bonding which has covalent, ionic and metallic contributions. TiN thin films are widely used in variety of applications such as hard, protective, wear resistance and decorative coatings. TiN shows a metallic luster and have a thermal and electrical conductivity of the order of magnitude of pure metals. It is also used very successfully in semiconductor industry as interconnector and diffusion barriers in ULSI circuits [3-7]. In addition, TiN films have been used for cosmetic gold surface [8] wavelength selective transparent optical films [9-11], thin film resistors [12-14], tool bit coatings, and, due to its strong infrared reflection, energy-saving coating for windows and also used in biomedical applications [15-18].

Recent experimental and theoretical investigations have disclosed interesting and extended application of TiN thin film in microelectronics and biotechnology industries. For example, use of TiN as a potential gate metal in metal-oxide-semiconductors (MOS) devices with high k-gate dielectric [19-21] and corrosion-resistance metal layer in complementary metal-oxide-semiconductors (CMOS) bioelectronics devices is reported [22-23]. In addition, a further application of TiN as a Ohmic contact material in n-type semiconductors such as Si, Ge and CdS [24-27] and charge collector in dye-sensitized solar cells [28-31] has been demonstrated.

TiN has good superconducting properties with a relatively high transition temperature (T_C) about 6 K [32-33], which extended its use to superconducting waveguide microresonators [34-35]. Disorder-driven superconductor-insulator transition (by decreasing the film thickness) was observed in TiN thin films recently [36-38]. Below a certain critical temperature and in the presence of a magnetic field TiN becomes a

superinsulator, *i.e.* it reaches a state of zero electrical conductance. The electrical resistance of superinsulator is become infinity, opposite to the superconductor of zero resistance at low temperature. The superinsulator nature in titanium nitride thin film was first discovered by Vinokur [39-40] *et al.* from Argonne National Laboratory, USA. Titanium nitride thin films are, thus, an ideal example of multi-functionality.
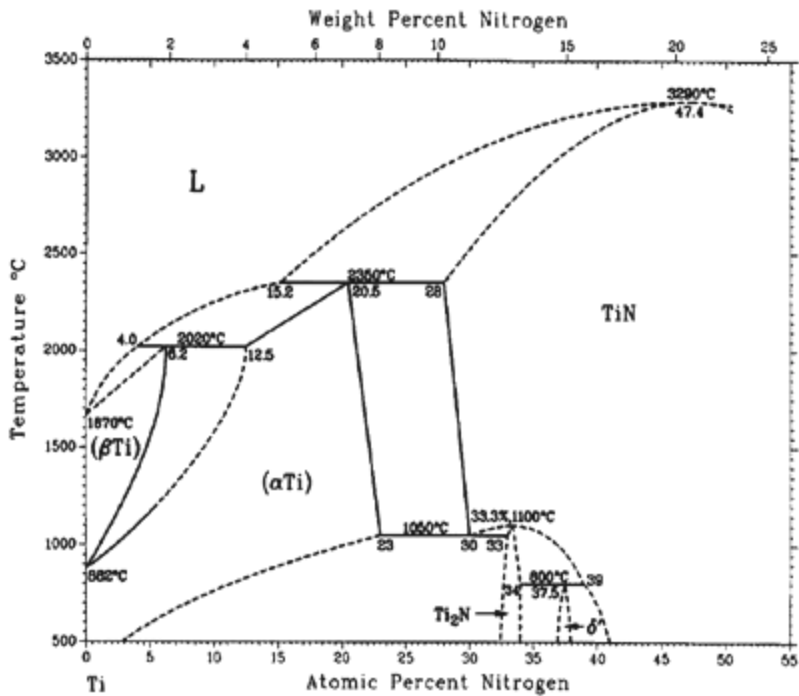
Figure 1.1. Temperature and nitrogen atomic percentage dependent phase diagram of Ti-N system (reference 41)

1.3 Physical and chemical characteristics of titanium nitride (bulk and thin films)

Some important properties of TiN have been summarized in Table 1.1. Several crystallographic phases of TiN exist depending on temperature and nitrogen atomic percentage as shown in the phase diagram of the Ti-N system in figure 1.1 [41] . The primary nitride phase TiN, crystallizes in the rock salt structure (Fm3m) with a lattice parameter of 4.24A° for the stoichiometric TiN (N/Ti=1). Sub-stoichiometric Ti_2N (N/Ti=0.5), the other major Ti-N compound, has two known phases, ε-Ti_2N and δ'-Ti_2N. The rocksalt structure of TiN is indicative of an increase in the number of valence electrons from Ti to TiN. Clearly, this suggests that N is responsible for the increase in valence electrons. The unit cell of stoichiometric TiN is shown in the figure 1.2.
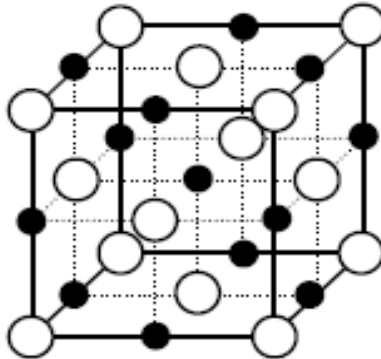
Figure 1.2 Unit cell of TiN (Open circles: Ti atoms, Solid circles: N atoms)

Table 1 .1 Physical properties of stoichiometric TiN thin films

Crystal structure	Face Centered Cubic (FCC)
Appearance	Gold color
Density	5.40 g/cm^3
Melting Point	2930°C
Thermal conductivity	30 Watt/m. K
Thermal Expansion Coefficient	9.4×10^{-6} /°C
Electrical resistivity	$20 \pm 6 \mu\Omega$-cm
Hall-coefficient	-6.7×10^{11} m^3/C
Temperature Resistance	Begins to oxidize around 600 °C in air. More resistant in an inert atmospheric
Chemical Resistance	Highly inert to acid, base, solvents, caustic etc
Hardness	Values of 25 – 28 GPa
Young' s modulus	590 GPa
Coefficient of Friction	TiN generally provides low friction against steels, carbides, ceramics and plating. A typical value is 0.65 for TiN against steel
Adhesion	The TiN coating forms a metallurgical bond to the substrate that will not flake, blister, chip or peel. In fact, the coating is actually implanted slightly into the surface layer of the substrate
Non-stick	TiN is an excellent non-stick surface against most of the materials

The ε-Ti$_2$N phase crystallizes in the anti-rutile" (P42/mnm) structure at temperatures below 900°C, which consists of a bcc Ti lattice, with N atoms filling one-half of the available octahedral sites (rather than all of the octahedral sites as in TiN). In general, transition metal nitrides are Hagg compounds in which the crystal structure is either hcp or fcc. However, the ε-TiN$_x$ is a non-Hagg type transition metal nitride with an unusual tetragonal structure which is related to both to the bcc β-Ti and to the hcp α-Ti [42]. The unit cell is tetragonal with a=4.945 A^o and c=3.034 A^o. ε-Ti$_2$N can be obtained from the disordered δ-TiN$_x$ only at high temperatures because the transition is kinetically hindered and high activation energy must be provided to initiate it. The δ'-Ti$_2$N phase is, however, only metastable and transforms by ageing into thermodynamically stable ε-Ti$_2$N which crystallizes in the tetragonal primitive antirutile structure. It is essentially a vacancy-ordered form of the rocksalt structure with a small tetragonal distortion. Thus, as N is added to Ti, Ti transforms from the hcp α-Ti phase to the tetragonal ε-Ti$_2$N phase, and finally to fcc δ'-Ti$_2$N and δ -TiN phases. Again, this also suggests that as the N fraction increases, the number of valence electrons increases. The color of the Ti$_2$N phases has been reported as a bright yellow [43], as opposed to the golden yellow for TiN [44]. The units cells of tetragonal δ'-Ti$_2$N and ε-Ti$_2$N phases have been shown in the figure 1.3. Table 1.2 presents the structural information of Ti-N system of different crystal structures.

Table 1.2. Complete structural information of Ti-N system with various crystallographic phases

phase		$x = N/Ti$	Crystal structure	Lattice parameters
α-Ti (N)		$0 < x < 0.40$	Hexagonal	a=2.956 A° ' c=4.765 A°
Ti$_2$N	ε-Ti$_2$N	$0.40 < x < 0.52$	Tetragonal	a=4.945 A° , c=3.034 A°
	δ'-Ti$_2$N	$0.52 < x < 0.59$		a= 4.140 A° , c= 8.805A°
δ-TiN		$0.6 < x < 1.2$	Cubic (NaCl)	a=4.24A°
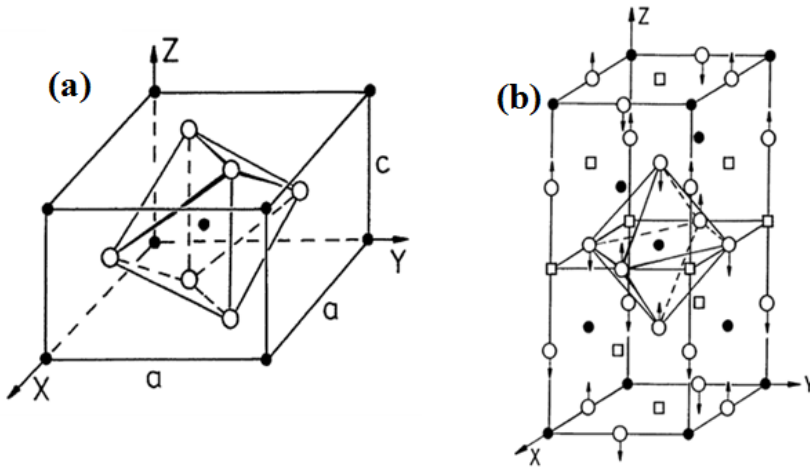
Figure 1.3 (a) Tetragonal unit cell of ε-Ti$_2$N. Full circles: N atoms; empty circles: Ti atoms (b) tetragonal unit cell of δ'-Ti$_2$N. Full circles: N atoms; squares: N vacancies; empty circles: Ti atoms. (reference R. Eibler, *J. Phys: Cond. Matter*, **10** (1998) 10223)

Nanocrystalline TiN thin films possess different microstructural features depending on the method of preparation. The physical properties of the film are in turn dependent on the microstructure. For example, hardness of TiN is inversely proportional to the grain size according to the famous Hall-Petch relation. The hardness of TiN is intimately connected to the chemical bonding and electronic structure is a key to the unusual behavior of hardness in the rock salt structure. Many theoretical studies of their electronic structure have revealed an unusual mixture of covalent, metallic, and ionic contributions to bonding [45-49]. It is reported that the high hardness of TiN is due to a favorable occupancy of the hybridized Ti3d and N2p states leading to the covalent character [50].

TiN thin film exhibits high reflectance in the visible and IR region due to free electron intraband absorption. In contrast, interband transitions are responsible for colors, and other optical properties of these compounds. According to the band structure diagram of TiN [51], four transitions take place at $\Gamma'_{25} \rightarrow \Gamma_{12}$, $\Gamma_{15} \rightarrow \Gamma_{12}$, $X_5 \rightarrow X_2$ and $L_3 \rightarrow L'_3$ critical points in the Brillouin zone which correspond to the interband transitions at 1.0, 2.3, 3.9, and 5.6 eV. The lowest band gap transition ($\Gamma''_{25} \rightarrow \Gamma_{12}$) located at 1.0 eV is very weak and is responsible for the color of TiN film. In stoichiometric TiN this energy transition occurs at the same energy as in gold and thus it exhibits the golden-yellow color [51, 52]. In nanocrystalline TiN films this weak interband transition cannot be experimentally observed and discriminated from the strong dominating contribution of the intraband absorption in the SE spectra at low photon energy [53]. An optical energy transition at 3.5 eV has been assigned to Ti-N2p transition. Figure 1.4 shows the band structure of diagram of a nanocrystalline TiN thin film.
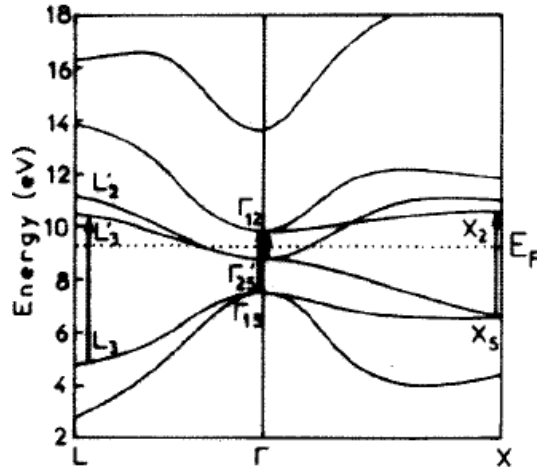
Figure 1.4 Band structure diagram around the centre of the Brillouin zone and the possible assignment of interband transition at Γ and in the vicinity of L and X points (reference 51)

The electrical conductivity of TiN is due to the intersection of the valence band of the Ti 3d electrons' with the Fermi level (E_F) [51]. The electrical resistivity of TiN thin films strongly depends on experimental parameters and film properties such as defects, impurities, microstructure, composition and structure as well. The presence of point defects together with the grain boundaries modifies the electron interactions with the Ti and N atoms and the electronic structure of the pure stoichiometric TiN.

Stoichiometric face centered cubic TiN possesses inversion symmetry, which forbids the first-order Raman scattering. However, TiN with defects or substitutional impurities, breaks the crystal symmetry and defect (impurity)-induced first-order Raman scattering can be observed

[54]. Previous studies of Raman scattering of TiN thin films have reported that low frequency scattering below 370 cm^{-1} is caused by acoustical phonons and the high frequency scattering above 500 cm^{-1} is due to optical phonons [32]. The scattering intensities in the acoustical branch are largely determined by the vibrations of the heavy Ti ions, while the scattering in the optical branch is mainly due to the lighter N ions [55]. Figure 1.5 shows the Raman spectra of TiN thin films.
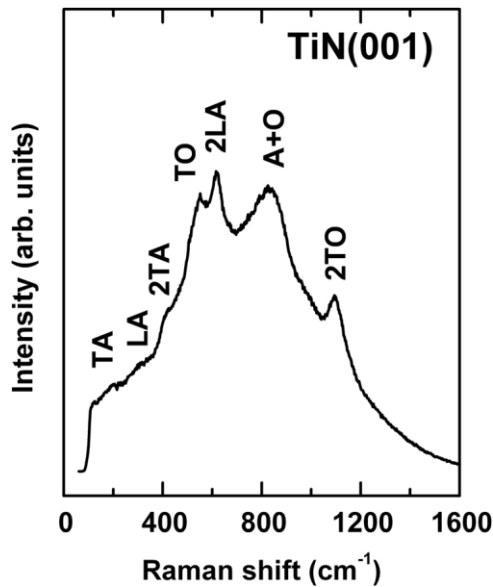
Figure 1.5 Raman spectrum of stoichiometric single-crystal TiN (001) (reference 54)

1.4 Sub-stoichiometric TiN$_x$

The properties discussed in the previous section, for stoichiometric TiN, vary significantly in non-stoichiometric TiN$_x$ ([N] / [Ti] $\neq$1) phases. Varying nitrogen content of the film causes the

introduction of sub-stoichiometric Ti-N phases leading to a wide range of compositions. The stoichiometry/composition variations in TiN_x thin films lead to change in crystal structure, chemical bonding and free electron concentration. The major source of non-stoichiometry in TiN_x thin film is anion vacancies for x<1 and interstitial N atoms for x>1 [56] where the cation vacancies are present at the Ti sub lattice.

Stoichiometric crystalline TiN is a good conductor of electricity whereas amorphous or nitrogen deficient (sub-stoichiometric) TiN is a very good insulator [57-59]. Both amorphous and sub-stoichiometric TiN film exhibits high electrical resistivity and high transmission of light in the visible region. One of the main factors that cause the deviation of physical properties of TiN thin films from those of the bulk is the presence of sub-stoichiometric impurities. The properties of TiN are extremely sensitive not only to nitrogen fraction, but to impurities as well, especially oxygen. Controlling oxygen content is of extreme importance, since the free energy of formation for titanium oxides is much lower than that for TiN [60-61] and some amount of undesirable titanium oxides may form even with a small amount of oxygen present. Oxygen presence alone has been shown to adversely affect many properties, including conductivity, hardness, adhesion, as well as optical properties. Other impurities, such as water vapor, can cause similar problems. Thus, it is of key importance that some attempt be made to determine what nitride phases and impurities are present.

The rock salt cubic crystalline phase (δ-TiN) is stable for a wide range of x in TiN_x ($0.6 \leq x \leq 1.2$). The lattice parameter varies appropriately with nitrogen composition [56, 62]. Figure 1.6 shows the increase of lattice constant with nitrogen composition. In the

substoichiometric range, high density of nitride vacancies are known to be formed in the crystal lattice, leading to shrinkage of the cubic lattice parameter as x decreases.
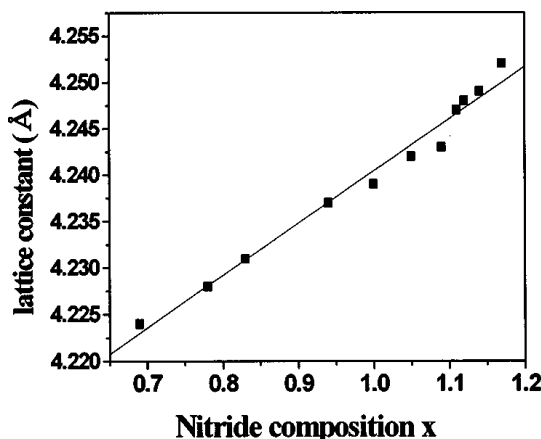
Figure 1.6 Variation of lattice constant with nitride composition x of substoichiometric TiN_x (reference 62)

Information about the electronic or mechanical properties of the ε and δ' phases, and even less of the other sub-stoichiometric Ti-N phases is limited. However, due to the large number of N vacancies in both phases of Ti_2N, it is expected that the electronic properties will be quite adversely affected. The hardness of sub-stoichiometric TiN_x is reduced due to the presence of nitrogen vacancies.

The colour of TiN also varies strongly with composition. With increasing nitrogen content the color changes from a titanium grey to light yellow (Ti_2N) to golden (TiN) to brown to bronze, and finally red [43], with the presence of H_2O or O_2 adding a purple hue [63]. Such variations of color and other properties with composition implies that

when composition may not be directly measured, external properties such as lattice parameter and colour may be used to get a rough idea of composition.

Reflectance spectrum of TiN_x film exhibits a minimum in the visible region [64]. The reflectance minimum is strongly dependent on the nitrogen composition. Variation in colour of the films is due to the change in reflectance minimum position which is very sensitive to the defects and impurity levels. There have been several studies [44, 65-66] to explain the color variation from the alteration in reflectance minima. Therefore, reflectance spectrum is a powerful tool to characterize the TiN thin films (estimate the composition and predicting the color) [64]. Typical reflectance spectrum of TiN_x films are shown in figure 1.7.
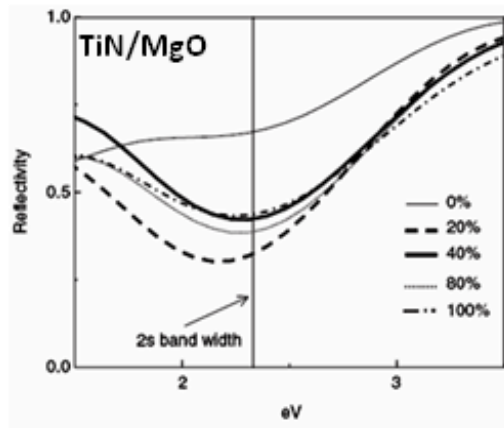
Figure 1.7   Variation of reflectance minima of TiN_x thin films with nitrogen atomic percentage (reference 64)

TiN films exhibit a minimum in resistivity for N/Ti =1 which increases for sub-stoichiometric and over-stoichiometric phases. This is because of the presence of nitrogen and titanium vacancies in sub-

stoichiometric and over-stoichiometric phases respectively. The resistivity of sub (over)-stoichiometric TiN_x is mainly due to two kinds of carrier scattering, one due to nitrogen (titanium) atoms randomly distributed at vacant interstitials, another attributable to grain boundary scattering [67]. Typical variation of resistivity as a function of nitrogen stoichiometry x, is shown in figure 1.8
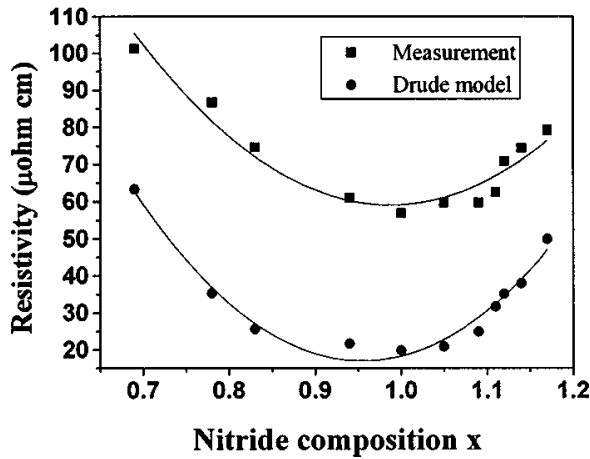
Figure 1.8 Variation dc four probe resistivity of TiN_x film with nitrogen composition. The film has minimum resistivity for x=1 (reference 62)

1.5 Metal substituted TiN thin films

The addition of a metal or multilayer stack of TiN and another metal nitride improves the physical and chemical properties. Ternary and multinary transition metal nitrides (TMN) have gained special attention because they provide a broader range of nitride structure types for a fine-tuning of mechanical and electrical properties. These materials may form multiphase (nanocomposite) or single-phase (solid solution) structures,

depending on the properties of the substituting metallic element, process parameters, or post growth treatments. In metal substituted TiN thin films, the Ti atoms are replaced by substituted metal atoms (Me=Zr, V, Cr, Ta, W, Mo and Nb) and stabilizing the ternary $Ti_{1-x}Me_xN$ phase over the entire range. Depending on the mutual solubility between the binary nitrides (TiN-MeN), these solid solutions may be either stable or metastable [68]. Holleck [69] introduced the concept of phase field in PVD deposited films of two components, i.e., a diagram depicting the phase expected to form during PVD deposition with kinetically limited growth conditions as a function of composition and substrate temperature. As an example, by calculating the free energies of formation for solution phases in the TiN-MeN systems and empirical studies the PVD phase field diagram could be constructed. In addition to stoichiometric binary and ternary nitride formation, the phase diagrams also predict the formation of sub-stoichiometetric phases, like Ti_2N and Ti_2MeN etc.
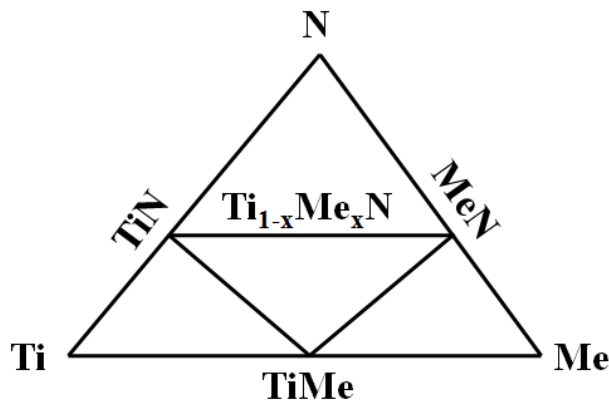
Figure 1.9 General isothermal phase field diagram of ternary Ti-Me-N system.

For example, the Ti-Al-N system exhibits the lines between the binary phases TiN, Ti_2N and AlN, TiAl, Al_2Ti, Al_3Ti and $AlTi_2$ from Ti-Al alloy and ternary compounds TiAlN, Ti_2AlN and $TiAl_2N$. For the TiN–ZrN pseudobinary system, recent *ab initio* calculations have shown that below 1000 °C the bulk phase diagram exhibits a large miscibility gap extending over the whole compositional range. However, $Ti_{1-x}Zr_xN$ arc-deposited films retained their as-grown single-phase structure up to 1200 °C [70]. The issue of phase stability in ternary TMN is more critical when Ta, Mo, or W metal is used for substitution, because the ground energy phase of TaN, MoN, or WN binary nitrides is the hexagonal structure [71, 72]. However, metastable ternary solid solutions with rocksalt structure have been produced by different PVD techniques in many systems, such as, Ti–Zr–N [70, 73-77], Ti–Ta–N [78-80], Ti-Nb-N [77, 81-83] Ti-Cr-N [84-86] Ti-V-N [87] , Ti–W–N [88] and Ti–Mo–N [89].

Most of the binary transition metal nitrides (MeN) with NaCl structure are miscible with TiN. However, the difference in the lattice parameters for binary nitrides (MeN) with respect to TiN results in the existence of a miscibility gap. The possibility of forming $Ti_{1-x}Me_xN$ solid solutions with the rock salt structure over the whole compositional range regardless of the valence electron configuration of the constituent metals was recently demonstrated from *ab initio* calculations [90]. However, different bonding types with nitrogen (metallic, ionic, and covalent) and variation of band structure were clearly evidenced depending on the valence electron configuration. The ternary compound $Ti_{1-x}Me_xN$ (Me=Zr, V, Cr, Nb) is crystallized in the rock salt structure in the whole composition range of $0 \leq x \leq 1$. The validity of Vegard's law, which relates

the composition and lattice parameter, confirms the miscibility between the binary counter parts TiN and MeN.

The main interest in the study of properties of metal-substituted TiN is centered on the improvement of their functional properties and technological applications. Several first principle calculations have shown that the metal substitution modifies the bonding nature, band structure and crystal symmetry [90, 91] which have a marked effect on the optical, electronic, vibrational and mechanical properties. For instance in Al substituted TiN, Ti atoms are replaced by Al atoms and the ternary compound $Ti_{1-x}Al_xN$ is stabilized in the rock salt cubic structure. The compound thus formed, cubic phase $Ti_{1-x}Al_xN$, was found to have superior oxidation resistance [92-94]. Similarly, addition of Si in to TiN improves the mechanical properties. Ternary $Ti_{1-x}Si_xN$ thin films have superior mechanical properties than the binary TiN and SiN [95-98].

The hardness of single layer TiN film is about 25GPa. Superhard coatings (hardness $\geq$ 40GPa) have been developed using titanium nitride nanocrystals embedded in amorphous silicon nitride matrix. TiN superlattices with NbN, CrN, TaN and VN are superhard materials. For example, the hardness of TiN/VN superlattices is 56 GPa [99] and TiN/NbN is 51 GPa [100]. On the other hand, sub-stoichiometric TiN is also very interesting since it has unusual physical properties that can be exploited. The electrical resistivity of sub-stoichiometric TiN_x increases and the material behaves like a semiconductor. The electronic structures should, however, be sensitive to the presence of vacancies and changes significantly from those for the stoichiometric phase. The vacancy concentration as well as the alloy composition is shown crucial to the electronic and mechanical properties.

It is thus possible to design multifunctional coatings, which mean one coating that fulfills several demands, but also that there can be one type of coating for each application. Simple binary TiN is not enough and recent research has therefore focused on ternary and multinary coatings. It was found that the properties of TiN thin films can be improved by the addition of the metal or semiconductor. In summary, titanium nitride is an important multifunctional material that continues and needs to be studied.

1.6 Motivation and objectives

It is evident from the literature review presented in the previous section that there are many "open" questions that remain to be addressed.

The growth of titanium nitride thin films in 100 % nitrogen atmosphere during sputtering is an aspect that has not been investigated. The implication of growth in 100% N_2 on physical behavior of TiN based is, therefore, not well understood. Conditions for the stabilization of monophase Ti_2N in thin films form has not been reported extensively. There are almost no reports on the optical constants and nanomechanical behavior of Ti_2N thin films. The conductivity of titanium nitride films is largely attributed to its unique band and electronic structure. However, the microstructural origins of the conductivity are not investigated. The optical constants and microstructural origin of electrical conductivity of metal substituted titanium nitride have also not been reported. The motivation of the current thesis is to address some of these issues.

The objective of the present work is, therefore, to deposit stoichiometric and non-stoichiometric nanostructured titanium nitride thin films on various substrates by RF reactive magnetron sputtering and investigate their physical properties.

From the Ti-N phase system, it is seen Ti_2N phase is a line compound existing for a small window of nitrogen partial pressure and substrate temperature. The first attempt is to stabilize single phase tetragonal Ti_2N thin films at low temperatures and study the structure, composition, microstructure, mechanical, optical and electrical properties.

The second objective is to study the structural, microstructural, mechanical, tribological, optical, electronic and electrical properties of Nb-substitute TiN films. Nb has a valence electron configuration of d^4s^2, its atomic radius is 146 pm (which is close to Ti 140 pm) and is easily soluble in TiN. Furthermore, it is known that the TiN-NbN system is miscible and the compound (Ti,Nb)N is a stable pseudo-binary alloy [101]. Therefore, the solid solution $Ti_{1-x}Nb_xN$ stabilizes in the rocksalt structure in the entire range of x and is expected to improve the mechanical, tribological and electrical properties compared with their binary counter parts TiN and NbN. Hence, Nb was selected as the metal for substitution in TiN to form $Ti_{1-x}Nb_xN$ films.

The electrical properties of granular TiN_x and TiN based thin films are strongly dependent on the microstructure. In this case, surface roughness and grain boundaries will contribute to the overall resistivity of the film due to electron-surface and electron-grain boundary scattering. It is important to investigate the microstructural origin of the electrical properties of TiN_x thin films. The prime objective of the last

section is; therefore, study the microstructure dependent electrical and electron transport properties of TiN_x and $Ti_{1-x}Nb_xN$ thin films using conductive-atomic force microscopy (C-AFM).

1.7 Thesis outline

In this work Ti, TiN_x and $Ti_{1-x}Nb_xN$ thin films were deposited by RF reactive magnetron sputtering on glass, quartz, silicon (311) and 316 LN nuclear grade stainless steel substrates. Including this introductory chapter, the thesis is organized into seven chapters.

Chapter 1 discusses the basic physical properties and various applications of TiN thin films.

Chapter 2 describes the experimental techniques used to deposit and characterize the films. Comprehensive description of the RF reactive sputter deposition of Ti, TiN_x and $Ti_{1-x}Nb_xN$, and optimized conditions are presented. The details of the characterization techniques used, x-ray diffraction, field emission-scanning electron microscopy, atomic force microscopy, energy dispersive x-ray spectroscopy, UV-VIS-IR spectrophotometer and nanoindentation are presented.

Chapter 3 presents the results of studies on physical properties of pure Ti and stoichiometric TiN thin films.

In chapter 4, the influence of substrate temperature T_s, on the structure, composition of TiN_x films is reported. The successful deposition of single

phase Ti_2N films and their structural, morphological, mechanical, optical, and electrical properties is the main feature of this chapter.

Chapter 5 presents the influence of Nb concentration on the physical properties of TiN thin films. It is observed that the structure, microstructure, mechanical, optical, electrical and vibrational properties of $Ti_{1-x}Nb_xN$ ($0 \leq x \leq 1$) films are strongly affected by Nb concentration. The hardness and Young's modulus increased, whereas electrical resistivity decreased with an increase in the Nb concentration in the films. The complex dielectric function of $Ti_{1-x}Nb_xN$ ($0 \leq x \leq 1$) films in the energy range 1.5 to 5.5 eV is calculated by fitting reflectance spectra based on Drude-Lorentz model.

In chapter 6, results of investigations on the microstructure dependent electrical properties of TiN_x and $Ti_{1-x}Nb_xN$ thin films by conductive-atomic force microscopy (C-AFM). Detailed study of C-AFM results *i.e.* surface conductivity map and local electron transport is presented.

Chapter 7 presents the various conclusions that can be drawn from the present investigations and discusses the scope for future work.

CHAPTER-2

THIN FILM DEPOSITION AND CHARACTERIZATION

Abstract

In this chapter, a brief description of the sputter deposition method and the importance of the process parameters in thin film deposition is first discussed. The details of the characterization techniques used such as, x-ray diffraction, field emission-scanning electron microscopy, atomic force microscopy, energy dispersive x-ray spectroscopy, UV-VIS-NIR spectrophotometer, four probe method and nanoindentation are presented in the second part.

2.1. Thin film deposition

2.1.1 Thin film deposition techniques

The processes of thin film deposition are distinguished based on the nature of source material, the technique of vaporization and the processes of condensation. Processes that involve the use of a solid source material which is vaporized either by heating or energetic particle bombardment and finally condense as a films are called physical vapor deposition technique. If the source materials are gasses and condensation of films occurs as a solid by product of the chemical reaction, the process is called chemical vapor deposition. In solution based techniques, the precursor is directly applied to the substrate and then dried to realize a film of the desired material [102, 103].

2.1.2. Sputtering

Sputtering is a PVD thin film deposition technique that is extensively used for deposition of complex materials. The ejection of atoms from the surface of a material (the target) by bombardment with energetic particles is called *sputtering*. If ejection is due to positive ion bombardment, it is referred to as *cathodic sputtering*. The ejected or sputtered atoms can be condensed on a substrate to form a thin film. Sputtering is useful for many materials; especially compounds and alloys, since the composition of the film comes out nearly the same as that of the target [104]. It is also useful for materials, which cannot be evaporated easily.

2.1.3 Physics of sputtering:

Physical sputtering is driven by momentum exchange due to collision between ions in the gas phase and atoms in the material. The incident ions set off collision cascades in the target. As a consequence, cascades recoil and atoms reach the target surface with energy above the surface binding energy leading to ejection from the surface. Physical sputtering has a well-defined minimum energy threshold which is equal to or larger than the ion energy at which the maximum energy transfer of the ion to a sample atom equals the binding energy of a surface atom. This threshold typically is somewhere in the range 10–100 eV [105].

2.1.4 Mechanism of Sputtering:

A sputtering event is initiated by the first collision between incident ions and target surface atoms followed by the second and the third collisions between the target surface atoms. The displacement of target surface atoms will be more isotropic due to successive collisions and atoms may finally escape from the surface. Figure 2.1 shows the sputtering collision on the target surface.
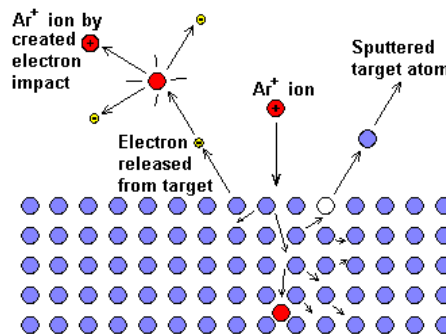
Figure 2.1 Incident ions and the sputtered particles [105]

Sputtering Yield:

The sputter yield *S* is defined as *the mean number of atoms removed from the surface of a material (target) per incident ion*. The sputtering yield is dependent on the following parameters [104]

    i)   Density of target material

    ii)   Energy of incident ion

    iii)   Incident angle of ions

    iv)   Crystal structure of target surface

Sputtering is classified into different types depending on the nature of target material (conducting, semiconducting or insulating); process used for ionization of the sputtering gas single or mixed gas sputtering atmosphere and the number of layers or elemental components in the thin films.

2.1.5 RF Magnetron Sputtering

Due to the substitution of an insulator target for the metal target in a dc diode sputtering system, the sputtering glow discharge cannot be sustained because of the immediate build-up of a surface charge of positive ions on the front of the insulator. To sustain the glow discharge with an insulator target, the dc voltage power supply is replaced by an RF power supply. This system is called an RF sputtering system. Presently the RF-sputtering system holds an important position in the field of deposition of thin films. A schematic view of an RF magnetron sputtering system is shown in figure. 2.2.
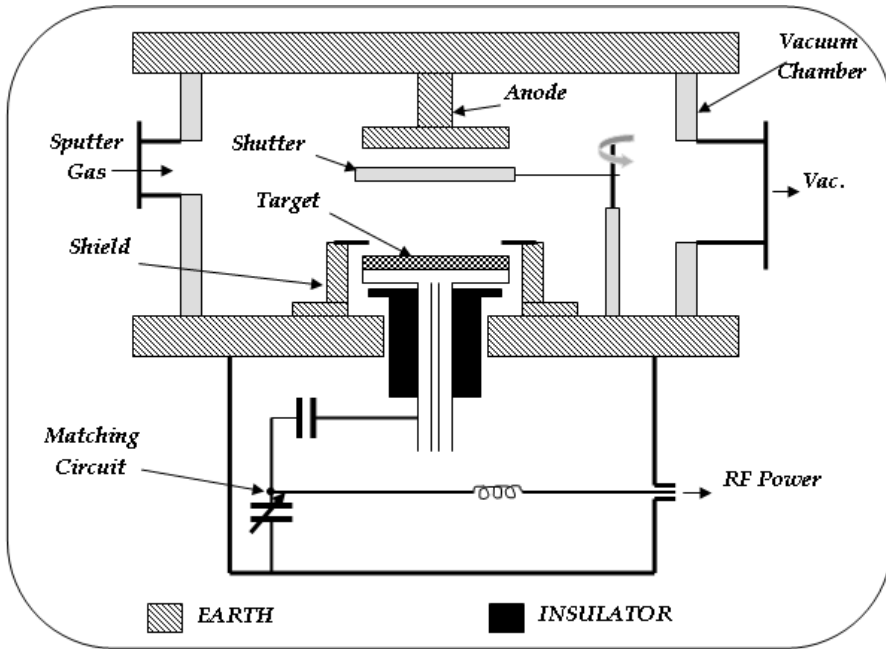
Figure 2.2 schematic view of an RF magnetron sputtering

The RF diode sputtering system requires an impedance-matching network between the power supply and discharge chamber. A typical network for impedance matching is shown in figure 2.3 [106].

The impedance of the RF-power supply is almost always 50 Ω. The impedance of the glow discharge is of the order of 1 to 10 kΩ. In RF diode sputtering, the target current density i_s is given by $i_s \cong C \dfrac{dV}{dt}$
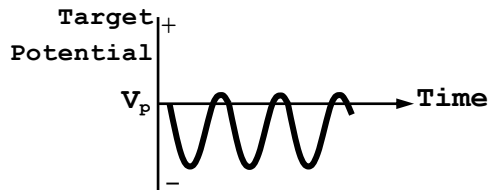
V_p: PLASMA POTENTIAL
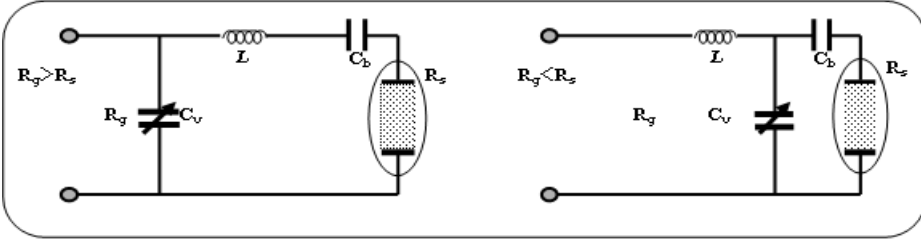
Figure 2.3 Impedance matching networks for RF-sputtering system

$$X_L = \sqrt{R_s R_g - R_s} \qquad X_c = \frac{R_s R_g}{X_L} \qquad X_c = R_s \sqrt{\frac{R_g}{(R_s - R_g)}} \qquad X_L = \frac{R_s R_g}{X_c}$$

R_g:impedance of RF-generator, C_v:variable capacitor
R_s:impedance of RF-discharge, C_v:blocking capacitor

where *C* is the capacitance between the discharge plasma and the target, $\frac{dV}{dt}$ denotes the time variations of the target surface potential. This indicates that the increase of frequency increases the target ion currents.

In the RF discharge system the operating pressure is lowered to as low as 1 mTorr, since the RF electrical field in the discharge chamber increases the collision probability between the secondary electrons and the gas molecules. In the RF sputtering system, a blocking capacitor is connected between the matching network and the target. The target area is much smaller than the grounded anode and the chamber wall. This asymmetric electrode configuration induces a negative dc bias on the target, and this causes sputtering in the RF system.

Magnetron sources are of great use to enhance ionization in the sputtering processes. In the magnetron, number of high strength magnets are placed at the rear of the target. They are fixed in a such a manner that the magnetic lines are force are perpendicular to the applied electric field.

As a result, the electron paths become helical, their mean free path increases and therefore ionization probability also increases. Figure 2.4 shows the cross-sectional view of the planar magnetron sputtering. Magnetron sputtering can be used in DC or RF modes to enhance sputtering rates. It is now a standard technique for deposition of thin films by sputtering.
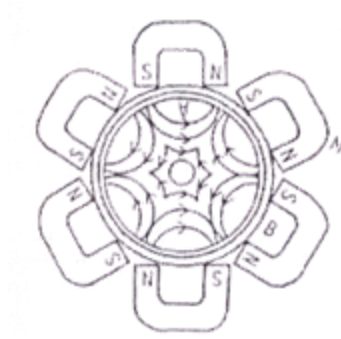
Figure 2.4 Cross-sectional view of the planar magnetron sputtering

In the magnetron sputtering system the working pressure is 10^{-5} to 10^{-3} Torr and the sputtered particles traverse the discharge space without collisions. Thus the deposition rate R is given by

$$R \cong k \frac{W_0}{t} \qquad (1)$$

where $k=1$ for the planar system, W_0 is the amount of sputtered particles given by

$$W_0 = \left(\frac{j_+}{e} \right) st \left(\frac{A}{N} \right) \qquad (2)$$

where j_+ is the ion current density at the cathode, e is the electron charge, s is sputter yield, A is atomic weight of sputtered materials, and N is Avogadro's number [104].

2.1.6 Reactive sputtering

To deposit metal thin films by sputtering, the sputtering process is carried out in an inert gas atmosphere (usually argon). However, to deposit compound thin films such as TiN, TiO_2, AlN it is required to introduce reactive gas, such as O_2, N_2 in the sputtering process. The gas will react with the growing film to form the desired compound and the process is called Reactive sputtering. A major disadvantage is that the reactions occur with the sputtering target surface as well. This 'target poisoning' complicates reactive sputtering and reduces the thin film growth rate [107-109]. A few other key points in reactive sputtering process are

1) Part of the reactive gas is exhausted through the pumps while the rest react with the growing film.

2) Compounds tend to sputter more slowly than metals.

3) Target hysteresis-as shown in figure 2.5. This is characterized by sudden jumps in the thin film deposition rate, target voltage or nitrogen pressure. To successfully make compound thin films by reactive sputtering we must stay away from these sudden jumps in the process.
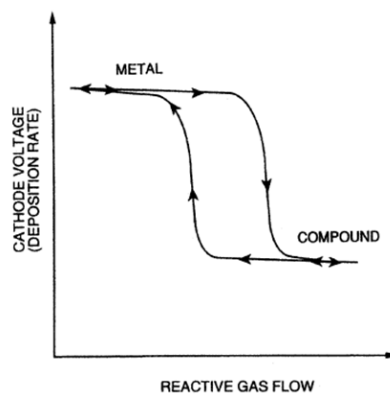
Figure 2.5 Hysteresis in reactive sputtering

2.1.7 Deposition of Ti, TiN_x and $Ti_{1-x}Nb_xN$ films using RF reactive magnetron sputtering

RF magnetron sputtering has been widely accepted as one of the versatile techniques for the deposition of high quality TiN thin films by several research groups [110-113]. Using RF magnetron sputtering any solid material (metal, insulator and semiconductor) can be sputtered. In addition, complex compounds can be sputtered stoichiometrically, use of low gas pressure for sputtering, appreciable rates of deposition and uniformity over large area is also possible. The properties of the sputter films are strongly influenced by process parameters such as RF power density, substrate temperature, working/sputtering gas pressure and substrate to target distance. In the present study, metallic Ti thin films were deposited in 100% Ar atmosphere, while TiN and $Ti_{1-x}Nb_xN$ films were deposited in 100% N_2 atmosphere.

During deposition of thin films, the vacuum chamber is continuously cooled by flow of water through the water cooling jackets fitted on the exterior to the vacuum chamber. It is evacuated through the electro-pneumatic roughing valve from atmospheric pressure to 2×10^{-2} mbar using a rotary vane mechanical pump (RP, DS-102, Varian, Italy) with an approximate pumping speed of $6.84 m^3 h^{-1}$. The vacuum chamber is isolated from the turbo molecular pump (TMP, Turbo-V 301, Varian, Italy) through a mechanical screw driven gate valve which is attached to the vacuum chamber by a 6" conflat flange. The pumping speed of the TMP is about 15 $m^3 h^{-1}$. Once the chamber pressure reaches to 2×10^{-2} mbar, the roughing valve is closed and the TMP is evacuated through electro-pneumatic backing valve. As the fore-line pressure reaches to 2×10^{-2} mbar, the TMP is switched on and the gate valve is opened. The

pressure in the vacuum chamber can now be brought into the high vacuum regime. The pressure is monitored using a cold cathode gauge. A base pressure of 3×10^{-6} mbar can be achieved in about 2 hours. The working pressure during is controlled partly by adjusting the total input gas flow and by reducing the throughput of the TMP by partially closing the gate valve. Once the pre-determined working pressure and deposition temperature is achieved, the sputter deposition process is started by initiating the plasma using the RF power generator coupled with matching network. The vacuum chamber walls and substrate holding stage was grounded during deposition. The experimental conditions used to deposit Ti, TiN_x and $Ti_{1-x}Nb_xN$ are mentioned in chapters 3, 4 and 5. Figure 2.6 shows the photograph of the RF magnetron sputtering system (Advanced Process Technology, Pune, India) used in the present study.

Figure 2.6 Photograph of the RF reactive magnetron sputtering used in the present study

2.1.8 Substrate material and preparation

In this study, the films were deposited on to different substrates depended on the nature of study. Optical (transmittance and reflectance) and photoluminescence studies TiN_x were carried out on films deposited on to well polished fused silica substrates which were 25 mm^2 in area and 0.5 mm thick. For hardness measurements, $Ti_{1-x}Nb_xN$ films were deposited on mirror polished 316 LN nuclear grade stainless steel substrates of 25 mm^2 area and 2 mm thick. Prior to deposition the substrates were cleaned with a laboratory detergent, wiped with soft dust free surgical cotton, and then washed with tap water. Traces of detergent were removed by gently rubbing under running water, then the substrates were rinsed in distilled water. These substrates were dried in an oven at 100^oC. Finally the substrate was cleaned by rinsing in an ultrasonic bath of acetone, iso-propanol and de-ionized water for about 15 minutes each. Again the cleaned substrates were finally dried in an oven at 100^oC for 30 min.

2.2. Characterization

2.2.1. Thickness measurement: Surface profilometer

The thickness of the samples was measured using stylus profiler (also known as profilometer) (Model XP-1, Ambios Technology, USA). Surface profilometry is a direct, simple and fast measurement technique for determining the physical thickness of thin films [114]. The only requirement is the existence of a step as shown in figure 2.7. Diamond stylus (tip) was used to determine the thickness of Ti, TiN_x and $Ti_{1-x}Nb_xN$ films.
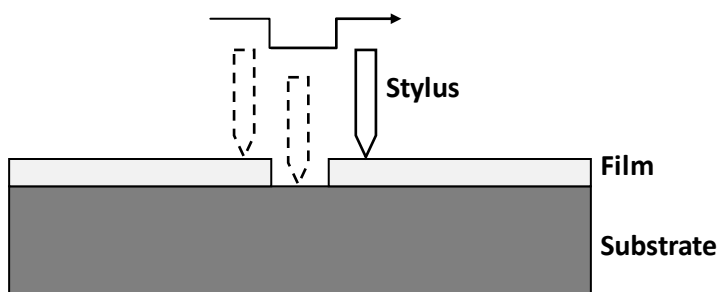
Figure 2.7 Illustration of stylus profilometer measure film thickness

2.2.2. Structural characterization

X-ray diffraction is a well-known technique for characterizing the crystal structure of materials. X-rays have a wavelength of the order of Angstroms (10^{-10} m), which is comparable to the inter-atomic spacing in crystalline solids. Therefore, a diffraction pattern can be observed when a beam of x-rays is directed on a crystalline material (where the atoms are arranged periodically). This diffraction pattern is directly related to the crystal structure of the material under observation.

The crystal structure of Ti, TiN_x and $Ti_{1-x}Nb_xN$ films was determined using x-ray diffraction and transmission electron microscopy. Two types of x-ray diffractometers with different x-ray source were used to characterize the films. One was equipped with Co K_α (λ=1.7889A^o) radiation in a wide angled x-ray diffractometer (INEL, CPS120) and a curved position sensitive detector was used to collected the data. The diffractometer is in Bragg-Brentano geometry. While, the other is grazing-incident x-ray diffrctometer (Bruker D8 Discovers) equipped with Cu K_α radiation (λ=1.5405A^o). The GI-XRD pattern was obtained

with a grazing angle of 1.5°. Calibration using a Si standard was done to account for the instrumental line broadening and the values were approximately 0.05° for INEL and 0.10° for Bruker diffractometer. The XRD and GIXRD patterns of all films were indexed using joint committee on powder diffraction standards (JCPDS) [115. 116]. These results gave important information regarding the variation in film orientation, lattice constant, crystallite size and strain as a function of process parameters.

Crystallite size and lattice parameter calculation

The crystallite sizes of the films were calculated by a line profile analysis of the peak broadening. The crystallite size D was estimated using the Scherrer equation [117].

$$D = \frac{0.94\lambda}{\beta \cos\theta_\beta} \qquad (3)$$

Here λ is the x-ray wavelength (Cu-K_α radiation, λ=0.15405 nm), β is full width at half-maximum of the XRD peak and θ is the Bragg diffraction angle.

The lattice parameter was calculated using 2θ peak position from the relation

$$d_{hkl} = \frac{a}{\sqrt{h^2 + k^2 + l^2}} \qquad (4)$$

Where
a - lattice constant
d- spacing between the planes
h,k,l- miller indices

Vegard's law

Vegard's is an approximate empirical rule which has a linear relation between the lattice parameter and the composition of the ternary system. In the case of $Ti_{1-x}Nb_xN$ thin films, the calculated lattice parameter of cubic structure was compared with the expected value from Vegards law [118]

For the ternary system, $Ti_{1-x}Nb_xN$, it is expressed as

$$a_{Ti_{1-x}Nb_xN} = (1-x)a_{TiN} + xa_{NbN} \qquad (5)$$

Here a_{NbN} and a_{TiN} are the bulk values of the lattice parameters of NbN (0.439 nm) and TiN (0.424 nm) respectively.

2.2.2.2. Transmission Electron Microscopy (TEM)

The crystal structure of TiN_x and $Ti_{1-x}Nb_xN$ thin films were also determined using transmission electron microscope operated in the selected area electron diffraction (SAED) mode (model: FEI Tecnai G^2 S-Twin, FEI electron microscope operated at 200 kV using Gatan CCD camera).

Figure 2.8**.** Photograph of the Transmission electron microscope

2.2.3. Chemical composition

Chemical composition of TiN_x and $Ti_{1-x}Nb_xN$ thin films was determined using x-ray photoelectron spectroscopy and energy-dispersive x-ray spectroscopy respectively.

2.2.3.1 X-ray photoelectron spectroscopy

X-ray photoelectron spectroscopy (XPS) is a quantitative spectroscopic technique that measures the elemental composition, chemical state and electronic state of the elements that exist within a material. The phenomenon is based on the photoelectric effect, where the concept of the photon was used to describe the ejection of electrons from a surface when photons impinge upon it. XPS

simultaneously measure the kinetic energy and number of electrons that escape from the top 1 to 10 nm of the material being analyzed. Each atom in the surface has core electrons with a characteristic binding energy that is conceptually, not strictly, equal to ionization energy of the electron. The energy of an X-ray with particular wavelength is known, the electron binding energy of each of the emitted electrons can be determined by using an equation

$$E_{binding} = E_{photon} - (E_{kinetic} + \phi)$$ (6)

where $E_{binding}$ is the binding energy (BE) of the electron, E_{photon} is the energy of the X-ray photons being used, $E_{kinetic}$ is the kinetic energy of the electron as measured by the instrument and ϕ is the work function of the spectrometer [119]. The binding energy of the peaks is characteristic of each element. The peak areas can be used (with appropriate sensitivity factors) to determine the composition of the materials surface. The shape of each peak and the binding energy can be slightly altered by the chemical state of the emitting atom.

In the present case, the composition of TiN_x films, *i.e.,* the N/Ti ratio in the films was determined using X-ray photoelectron spectrometer (XPS-model PHI 5700). The excitation X-ray source for the XPS used was Mg K_α at an energy level of 1253.6 eV. The spectra of the Ti-2p, N-1s, and O-1s peaks were calibrated with respect to the C-1s peak, which resulted from the adventitious hydrocarbon at an energy level of 284.8 eV. The base pressure in the analysis chamber was about 7 x 10^{-8} Pa. The XPS spectra were fitted using a non-linear least squares fit assuming a Gaussian/Lorentzian peak shape (G/L mixing ratio = 0.3).

2.2.3.2 Energy dispersive x-ray spectroscopy

Energy Dispersive X-Ray Spectroscopy (EDS or EDX) is a chemical microanalysis technique used in conjunction with scanning electron microscopy (SEM). The EDS technique detects x-rays emitted from the sample during bombardment by an electron beam to characterize the elemental composition of the analyzed volume. Features or phases as small as 1 µm or less can be analyzed. When the sample is bombarded by the SEM's electron beam, electrons are ejected from the atoms comprising the sample's surface. The resulting electron vacancies are filled by electrons from a higher state, and an x-ray is emitted to balance the energy difference between the two electrons' states. The x-ray energy is characteristic of the element from which it was emitted [120].

Figure 2.9 Photograph of field-emission scanning electron microscopy attached with INCA EDX detector. The present system used to determine microstructure and composition of the films.

In the present study, chemical composition of $Ti_{1-x}Nb_xN$ films was determined using energy-dispersive x-ray spectroscopy (EDX) analysis. EDX spectrum is obtained from FE-SEM using an INCA EDX system, which is equipped with an Oxford Instruments. The operating voltage and working distance for EDX measurement is 20 kV and 8.5 mm respectively.

2.2.4. Optical characterization

Optical properties of Ti, TiN_x and $Ti_{1-x}Nb_xN$ thin films were studied using a JASCO (V-570 UV-VIS-NIR) double beam spectrophotometer. The optical properties of these films are studied with respect to their transmittance and reflectance spectra by considering the interaction of photon with matter and consequent changes in electronic states The spectral transmission and reflectance (near normal) in the wavelength region from 190 to 1500 nm. The optical constants, refractive index and extinction coefficient of TiN_x thin films was calculated by fitting the measured reflectance/transmittance spectra using PUMA (Pointwise Unconstrained Minimization Approach) software [121, 122]. While refractive index and extinction coefficient and dielectric function of $Ti_{1-x}Nb_xN$ thin films was calculated by fitting the measured reflectance spectra based on Drude-Loerntz model [123].

If light is incident on a film of refractive index, n, coated onto a substrate of refractive index s, then at the air-film, the film-substrate and substrate-air interfaces, part of the incident intensity is reflected and part is it is transmitted. From fundamental considerations of optics it follows that since the reflected and transmitted beams originates from a single coherent source, the beams will exhibits interference

effects. The schematic diagram of the optics is shown in figure 2.10. The reflectance and transmittance spectra collected from the spectrophotometer were analyzed and studied the optical properties.
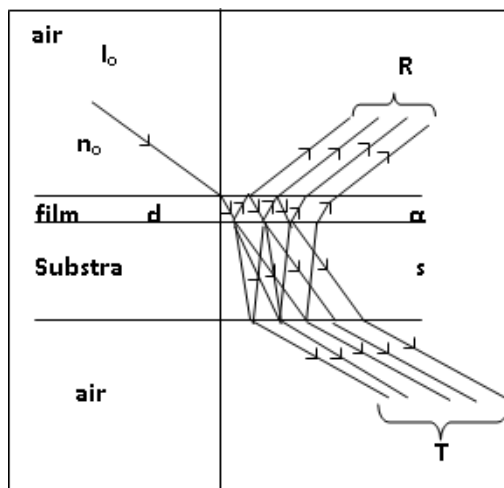
Figure.2.10 Interference from a thin film on a thick substrate, s>>d

If I_0 is the incident light and I the intensity of light after passing through the sample then, from *Beer's law* [124]

$$I = I_0 e^{-\alpha t} \tag{7}$$

Where, α is the absorption coefficient of the sample and t is the thickness of the sample.

The spectra transmittance and reflectance (at 6^0 angle of incidence) of the films were measured using a UV-VIS-NIR double beam spectrophotometer with an accuracy of $\pm 0.2\%$. Before recording the spectra, a 100% base line was established by performing the back correction. The wavelength range of the instrument was 190 to 2500 nm.

The spectra reflectance curves were taken using a Aluminum mirror (provided by the supplier) as the reference.

The transmittance of the samples is given by

$$T = \frac{I}{I_0} \qquad (8)$$

Reflectance is given by

$$R = (n-1)^2 + \frac{k^2}{(n+1)^2} + k^2 \qquad (9)$$

and the absorption coefficient α is defined by

$$\alpha = \frac{4\pi k}{\lambda} \qquad (10)$$

So, equation 9 becomes, with the substitution of k from equation (4),

$$n = \frac{(1+R)}{(1-R)} \pm \left\{ \left(\frac{R+1}{R-1} \right)^2 - (1+k)^2 \right\}^{\frac{1}{2}} \qquad (11)$$

Furthermore, optical constants n and k of thin films are highly influenced by various factors like deposition rate, substrate temperature, film thickness, microstructure, crystallinity and chemical composition

2.2.5 Microstructural characterization

The microstructure of Ti, TiN_x and $Ti_{1-x}Nb_xN$ thin films were determined using field emission-scanning electron microscopy (Carl ZEISS, FEG, Ultra 55) and atomic force microscopy (Seiko Instruments, SPA-400 of 3800 probe station, Japan) respectively. The FE-SEM images were obtained at an operating voltage of 20 kV and the working distance is 8.5 mm. The AFM images were registered in a contact mode with Si

cantilevers of length 100 µm. The resonant frequency and spring constants of the cantilever is 13 kHz and 0.18 N/m respectively.

2.2.5.1 Field Emission-Scanning Electron Microscopy (FE-SEM)

The scanning electron microscopy is a versatile technique that reveals detailed information about the morphology and the composition of natural and manufactured materials. SEM rasters a focused electron beam across a sample surface, providing high-resolution and long-depth-of-field images of the sample surface. A field-emission SEM provides narrower probing beams at low as well as high electron energy, resulting in both improved spatial resolution and minimized sample charging and damage [125]. The emission is reached by placing the filament in a huge electrical potential gradient. The FEG is usually a wire of Tungsten (W) fashioned into a sharp point. The significance of the small tip radius (~ 100 nm) is that an electric field can be concentrated to an extreme level, becoming so big that the work function of the material is lowered and electrons can leave the cathode. FESEM uses Field Emission Gun producing a cleaner image, less electrostatic distortions and spatial resolution < 2nm (that means 3 or 6 times better than SEM). The images formed by the field emission scanning electron microscope are from secondary electrons, backscattered electrons, characteristic X-rays, Auger electrons and others that are emitted by the sample.

2.2.5.2 Atomic force microscopy

Atomic force microscopy (AFM) is a very high-resolution type of scanning probe microscopy. SPM images are obtained by scanning a sharp probe across a surface while monitoring and compiling the tip-sample interactions to provide an image. The measurement of local physical properties of the material is extremely important for semiconductor fabrication. Using the SPM technique one can study the local physical properties materials down the atomic scale. The resolution obtained by this technique can resolve the single atom and the map the real 3-D images of the surface [126, 127].

2.2.5.3 Conductive-Atomic force microscopy

Conductive-Atomic Force Microscopy (C-AFM) is a mode of atomic force microscopy in which a conductive tip is scanned in contact with the conductive sample surface, while a voltage is applied between the tip and the sample, generating a current image. Using (C-AFM) one can probe the local variations in the conductivity of a material (crystal or thin film) with microstructure and thus examine the local variation of current at grain and grain boundaries [128-131].

The C-AFM measurements were made on the surface of TiN and $Ti_{1-x}Nb_xN$ thin films in order to study the local electron transport and microstructure origin of the conductivity. The C-AFM measurements were standardized first using a platinum thin film deposited on a silicon substrate. The C-AFM was operated in the constant force contact mode with Si cantilevers. The tip and one side of the cantilever were coated with 25 nm Au layer. The length of the cantilever is 10 μm, with a spring

constant of 2.2 N/m and resonant frequency of 29 kHz. The radius of curvature of the tip is less than 35 nm. The sample stage and the cantilever are carefully insulated from the apparatus frame. Conductive silver paint pasted on the top surface of the films formed the other electrode, to which a bias voltage was applied. The conductive tip was the counter microelectrode, connected to the ground potential. The feedback signal is used to generate a normal contact AFM topography image, while the current passing between the sample and the tip generates the conductive AFM (current) image. When surface morphology and local current are registered simultaneously, a dc voltage of 1V is applied to the bottom electrode prior to scanning. The range of current, which the current preamplifier could measure, was 100 pA to 100 nA. For each film a new tip was used to avoid artifacts due to tip erosion. A schematic view of the C-AFM measuring set-up is shown in figure 2.11.
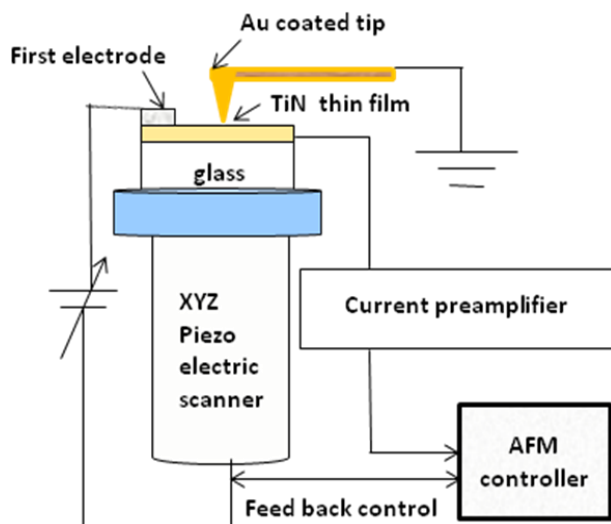
Figure 2.11 Schematic diagram of the conductive atomic force microscopy measuring set-up

In the present case, we have used SPA 400 of SPI 3800 probe station of Seiko Instruments, Japan for both contact mode and current mode.

Figure 2.12 Photograph of the SPA-400 atomic force microscopy used in the present study

2.2.6 Four probe method: measurement of electrical resistivity

Surface resistivity could be defined as the material inherent surface resistance to current flow multiplied by the ratio of specimen surface dimensions (width of electrodes divided by the distance between electrodes) which transforms the measured resistance to that obtained if the electrodes had formed the opposite sides of a square. In other words, it is a measure of the material surface inherent resistance to current flow.

Surface resistance does not depend on the physical dimensions of the material [132]. Four probe technique is very useful to measure the electrical resistivity of thin metallic and semiconductors films. The schematic diagram of four probe method used to measure the resistivity of Ti, TiN_x and $Ti_{1-x}Nb_xN$ films is shown in figure 2.13. The four probe measurement were carried out in a Agilent Technology B1500A, semiconductor analyzer,

According to Ohm's law, the resistance (R) of a material is the applied voltage (V) divided by the current (I) drawn across the material across two electrodes.
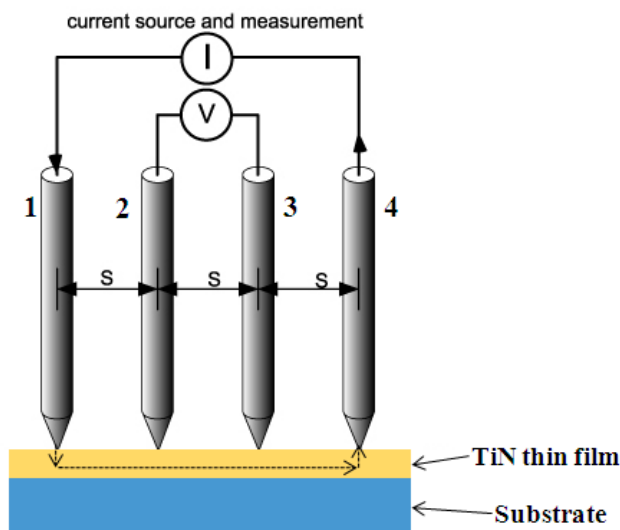
R=V/I

Figure 2.13 The schematic diagram of four probes set up. Probes 1 and 4 carry current (I), probes 2 and 3 measure voltage (V).

In the four-point probe set up, the voltage potential V adjacent to a probe carrying current can be given by

$V = \rho I / 2\pi r$

Where ρ is the surface resistivity of a material of semi-infinite size, I is the current in the probe and r is the distance between the voltage and the current probes.

Using dimensions in Figure 2.13 the voltage at probe 2 is,

$V_2 = \rho I / 2\pi \{(1/S_1) - (1/(S_2 + S_3))\}$

The voltage at probe 3 is

$V_3 = \rho I / 2\pi \{(1/(S_1 + S_2)) - (1/S_3)\}$

To get total voltage, substrate the voltage $V_2 - V_3$

$V = = \rho I / 2\pi \{(1/S_1) + (1/S_3) - (1/(S_2 + S_3)) - (1/(S_1 + S_2))\}$

Rearranging to get the resistivity

$\rho = 2\pi V / I / \{(1/S_1) + (1/S_3) - (1/(S_2 + S_3)) - (1/(S_1 + S_2))\}$

However, if all probe spaces are an equal size s, then the equation become

$\rho = 2\pi s (V/I)$

Considerations that need to be account for accurate four-point probe measurements are the spacing of the probes, temperature effects, thickness and surface roughness of the film. Therefore, the resistivity of metallic and semiconductor thin films measured using four probe method is

$\rho = 2\pi s (V/I) \times C.F$

In the above equation the correction factor (C.F) arises due to film thickness and surface roughness.

2.2.7. Mechanical characterization

Mechanical properties of film such as hardness (H), Young's modulus (Y), yield stress (σ) and ultimate tensile stress (σ_{UTS}) are derived from the response to applied force. In the present study, nanomechanical properties such as hardness and Young's modulus and nanotribological properties such as friction coefficient and wear volume were determined using nanoindentation, nanoscratch and wear test respectively. All above tests were performed in a Hysitron nanomechanical system (TriboIndentor, 900 series, USA).

2.2.7.1 Nanoindentation

Nanoindentation is a simple method that consists of hard indenter, indenting a specimen by a very small load using a high precision instrument, which records the load and displacement continuously [133]. The mechanical properties of thin films up on nanoindentation can be derived from the measured load-displacement (or loading /unloading) curve through appropriate analysis.

Hardness H of a material is usually defined as its resistance to local plastic deformation when a force is applied. As load is applied to the indenter, the depth of penetration in to the sample is measured. An indentation test instrument provides experimental results in the form of a load-displacement curve for the loading and unloading part of the indentation process as shown in figure 2.14
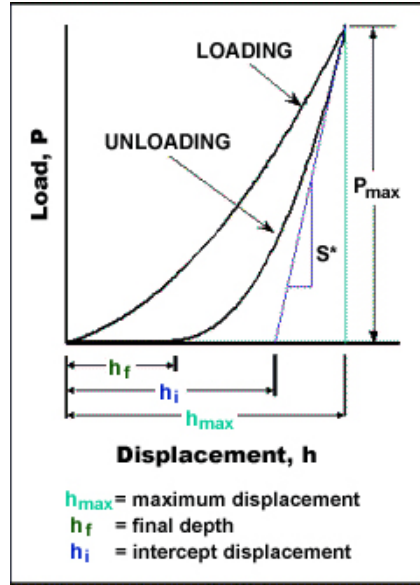
igure 2.14 Example of nanoindentation load-displacement curve obtained from Berkovich indenter during loading and unloading (32).

An analysis of the unloading data provides a value for the depth of the area of contact at full load. The area of contact at full load is determined from the known angle or radius of the indenter. For Berkvoch tip the total included angle on this tip is 142.3°, with a half angle of 65.35°. The hardness is derived by dividing the maximum load (P_{max}) by area of contact (A), thus [133]

$$H = \frac{P_{max}}{A(h_c)} \tag{12}$$

The slope of the linear variation of the unloading curve measures the elastic stiffness (S).

$$S = \frac{dp}{dh} = \frac{2}{\sqrt{\pi}} E_r \sqrt{A(h_c)} \tag{13}$$

Here E_r is the reduced modulus of the material. The Youngs modulus (Es) can be calculated using the equation

$$\frac{1}{E_r} = \frac{(1-v_i^2)}{E_i} + \frac{(1-v_s^2)}{E_s} \qquad (14)$$

In the above equation v and E stands for poisson's ration and Young modulus of indenter and sample. The subscript i and s represents the *indenter* and *sample* respectively.

In the present case, Ti, TiN$_x$ and Ti$_{1-x}$Nb$_x$N films were indented by Berkovich-type pyramidal diamond tip with a maximum load of 2000 µN. The trapezoid load function (which includes the loading, holding and unloading segments) was used to measure the hardness of the films with a loading rate of 200 µNs^{-1} and segment time of 10 see for each segment.

2.2.7.2 Scratch test

Scratch test method is intended to measure the resistance of solid surfaces to permanent deformation due to friction from a sharp stylus tip. In thin film-substrate system, using scratch test one can quantify parameters such as friction coefficient and adhesive strength [134, 135]. This technique involves that generate a controlled scratch by dragging a tip across the film surface under a constant or incremental normal load. In a scratch test, both lateral and normal loads applied simultaneously to the indenter in order to get scratch length of few micrometers. The basic principle involved in scratch is represented in figure 2.15. At a certain critical load the film surface will start to deform. The critical loads are very precisely detected by means of an acoustic sensor. The critical load data is used to quantify the adhesive properties of different film - substrate combinations.
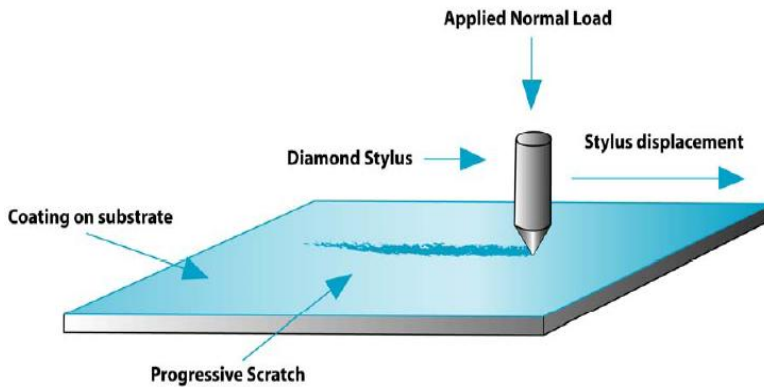
Figure 2.15 Principle of scratch test

The coefficient of friction is defined as the ratio of lateral force to normal force applied to the indenter (F= μL). In a scratch test, the coefficient of friction can simply determined by dividing the lateral force to that of normal force.

2.2.7.3 Wear test

The definition of wear may include loss of dimension from plastic deformation if it's originated at the interface between two sliding surfaces. The material intrinsic surface properties such as hardness, strength, ductility, work hardening etc. are very important factors for wear resistance [134-136]. To do wear test a specific area should be defined on the surface of the sample and the data was analyzed in terms of wear depth and wear volume. Wear volume can be calculated from the relation.

$$\text{Wear volume} = (\text{wear area})^2 \times (\text{wear depth}).$$

The variation in wear volume could be used to define the wear behavior of the material.

In the present case, a conical tip was used for both scratch and wear test of $Ti_{1-x}Nb_xN$ thin films. In the scratch test 5 segments were used in the load function to apply both lateral and normal loads with a scratch ramp force from 0 to 5000µN. Normal force and lateral displacements are controlled, while lateral force and normal displacement are simultaneously recorded as a function of time. During wear test, tip is repeatedly scanning over $2\,\mu m \times 2\,\mu m$ area with a contact force of 80 µN). In addition to mechanical and tribological tests, Hysitron nanomechanical system also has the imaging capability using *in-situ* atomic force microscopy. *In-situ* atomic force microscopy is employed to visualize the scratch and wear behavior

Figure 2.16 photograph of the Hysitron (Triboindentor-900) nanomechanical test system

CHAPTER-3

Ti AND TiN THIN FILMS

Abstract

In this chapter, structure, microstructure, mechanical optical and electrical properties of 150 and 220 nm metallic Ti and stoichiometric TiN thin films are studied. Thin films are deposited at room temperature on single crystalline Si (311) and polycrystalline 316 LN nuclear grade stainless steel (SS) substrates using RF reactive magnetron sputtering in 100% Ar atmosphere for Ti films and 100% N_2 for TiN films. Ti films are crystallized into hexagonal structure with (100) orientation and exhibits complex microstructure, which consists of obelisk-like, lenticular-like and flower-like structures. On the other hand TiN thin films are crystallized in to cubic structure with (111), (200) and (220) orientations and display good microstructure, which consists of spherical grains and pyramid-like structures. TiN films have higher hardness and Young's modulus than that of Ti films. The maximum values of hardness and Young's modulus for Ti thin films were obtained on SS substrate for 220nm film and the values are 12 and 132 GPa respectively. Similarly, the values for TiN thin films on SS substrate are 27 and 250 GPa respectively. The reflectance percentage was increase in the visible region for Ti films and it exhibits a reflectance minimum for TiN films. Polycrystalline TiN films have higher electrical resistivity than that of single crystalline Ti films. TiN films on Si substrate of thickness 220 nm has maximum resistivity and the values is 210 $\mu\Omega$-cm and similarly, Ti films on Si substrate of thickness 220 nm has minimum resistivity i.e., 54 $\mu\Omega$-cm.

3.1 Introduction

Transition metals in groups IVb and Vb and the first row elements, carbon and nitrogen, together make strong solids in the rocksalt structure. Titanium nitride is the one among them which exhibits interesting physical and chemical properties. The close packed structure, an fcc Ti sub-lattice with N filling all octahedral sites, is due to the relatively small size of the N atoms compared to Ti (0.74 A^0 vs. 1.47 A^0). In order to accommodate the interstitial nitrogen, Ti must transform from a bcc or hcp structure to fcc, and N_2 must decompose to atomic nitrogen. The sublimation energy for nitrogen molecule to nitrogen atom is 4.897 eV [137]. In this chapter, we present the results of studies on physical properties of pure Ti and stoichiometric TiN thin films. The significant variations in structure, microstructure, mechanical, optical and electrical properties of Ti and TiN thin films were observed. Some of the physical properties of metallic Ti and TiN compound are presented in the table 3.1

Table 3.1 some important physical properties of metallic Ti and TiN compound

Properties	TiN	Ti
Structure	Fcc (NaCl)	hcp
Space group	Fm3m	$P6_3$/mmc
Range of composition	$TiN_{0.6-1.1}$	N/A
Color	Golden	Grey
Density	5.40 g/cm^3	4.54g/cm^3
Melting point	2950 ^{o}C	1940 ^{o}C
Thermal conductivity	30 Watt/m.K	13 Watt/m.K
Thermal expansion	9.36×10^{-6}/K	11×10^{-6}/K
Electrical resistivity	20 ± 10 $\mu\Omega$-cm	39 $\mu\Omega$-cm
Hall constant	-6.7×10^{11}m^3/C	-7.7×10^{11}m^3/C
Vickers Hardness	21-24 GPa	0.55-2.5GPa
Young's modulus	590GPa	120GPa

3.2 Experimental conditions

Table 3.2 Experimental conditions being used to deposit Ti and TiN thin films

Experimental parameter	Ti	TiN
Deposition method	RF magnetron sputtering	RF magnetron sputtering
Target material	2 inch diameter Ti	2 inch diameter Ti
Substrates	Single crystal Si (311) and 316 LN stainless steel	Single crystal Si (311) and 316 LN stainless steel
Ultimate pressure	3×10^{-6} mbar	3×10^{-6} mbar
Working pressure	5×10^{-2} mbar	5×10^{-2} mbar
Sputtering gas	100 % Argon	100 % nitrogen
RF power	100 Watt	100 Watt
Distance between target and substrate	60 mm	60 mm
Substrate temperature	Room temperature	Room temperature
Deposition time	120 and 180 min	120 and 180 min

For the120 and 180 min deposition time, thickness of the films was 150 and 220 nm determined using surface profilemeter. The error in the thickness calculation was about ±10 nm for 150 nm films and is about ±16 nm for 220nm films.

3.3 Crystal structure of Ti and TiN thin films

XRD patterns of metallic Ti thin films on SS and Si substrates are shown in figure 3.1 (a). Films on both substrates crystallized into the hexagonal closed pack structure with preferred orientation only (100) plane. The intensity of the reflection from (100) decreased with increase

in thickness and it was also accompanied by a shift in the peak position to lower diffraction angle. Compared to the film on Si substrate the FWHM increased and the shift is more significant for the films on SS substrate. XRD patterns of Ti films, in the present case, are different from the other reported studies [138-140] with respect to preferred orientation. Titanium films deposited by physical vapor deposition technique at low substrate temperature found to have highly (200) orientated h.c.p structure. Films deposited at high substrate temperature of the order of 800°C on the contrary have been found randomly orientated structure [141]. Ti films deposited using RF bias sputtering by Sundgren *et al.* [142] also had random crystalline orientations with relative intensities of reflections being different from that of the bulk material. This has been attributed to an effect of preferential growth during deposition. Films prepared by arc deposition have been reported to have a prepared (110) orientation under conditions of high negative bias [143]. The crystalline orientation of the films is a process dependent and a generalization of the behavior cannot be made very easily. Beside this, Y. H. Song *at al.* [144] demonstrated that the crystal orientation is also dependent on the surface free energy and the crystal structure of substrates.

A first-order estimation of the stresses in the films was made from the shifts in the propositions of the reflections from their standard values. The standard value of 2θ position of (100) reflection of the stress free h.c.p Ti is appears at 35.170° (JCPDS file No: 89-5009). In the present case, films with lower thickness, the diffraction angle of (100) plane is appeared at the same position as the standard value. However, in films with higher thickness the diffraction angles appeared at 34.96° and 34.67° for the films on Si and SS substrate respectively. The shift in the

peak position is attributed to the presence of compressive stress in the films for higher thickness. The difference in lattice parameter between the deposited Ti films and substrate results the presence of stress.
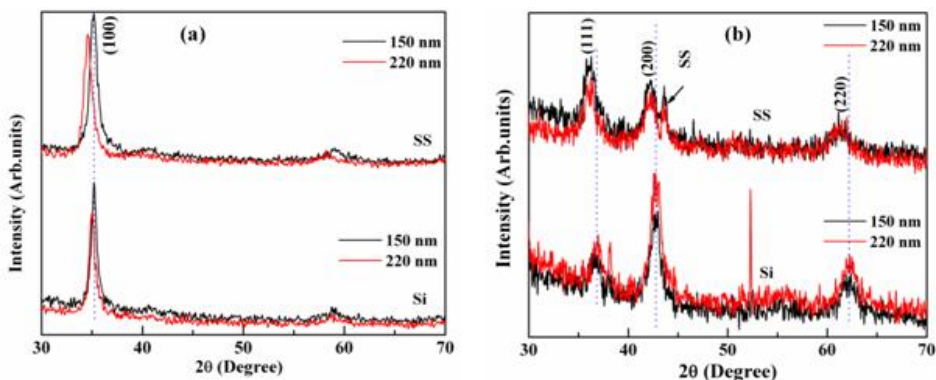

Figure 3.1 X-ray diffraction patterns of 150 and 220 nm thin (a) Ti films (b) TiN films on Si and SS substrates.

XRD patterns of TiN thin films on Si and SS substrates are shown in figure 3.1 (b). From the figure, it is evident that the films are crystallized into cubic structure with (111), (200) and (220) orientation. Films on Si substrate exhibits a (200) preferred orientation, whereas, films on SS substrate did not show any preferred orientation. Comparing the XRD patterns on Si and SS substrates, it is observed that all diffraction planes are shifted to lower diffraction angles for the film on SS substrate independent of the film thickness. The shift is attributed to the presence of residual stress in the films. The calculated lattice parameter of the films on Si substrate is 4.24A°, which is equal to the bulk stress free lattice parameter. On the other hand, the lattice parameter of the films on SS is 4.28A° which is greater than the standard value.

Volvada [145] had observed that the lattice parameter of TiN decreases with increasing film thickness. Kiran *et al.* [146] reported that the structural properties such as crystallographic orientations, lattice parameter variation and the level of stress states of TiN thin films are dependent on the structure and properties of substrates. Variations in stresses in TiN were studied by Machunze *et al.* [147] using x-ray diffraction technique and they reported that the average film stress is highly compressive in thin films and less compressive in thicker films. Mismatch of the lattice parameter and the thermal expansion coefficient between the film and substrate result in residual stress in the films. The intrinsic component of the total residual stress is due to contributions from the process parameters, whereas the extrinsic contributions are due to lattice constant or thermal expansion coefficient mismatches [148, 149]. If the extrinsic contributions had dominated, then the direction and magnitude of stress would have been completely predictable from an examination of the differences between the lattice constants and thermal expansion coefficients of the film and the substrate. The lattice mismatches between the film-substrate combinations that TiN-SS and TiN-Si are -21 % and 20.5 % respectively. The thermal expansion coefficient of TiN is 9.4×10^{-6}/°C and this value for Si and SS is 4.68×10^{-6}/°C and 17.3×10^{-6}/°C respectively [145]. The thermal expansion coefficient mismatch between TiN-SS is higher than that of TiN-Si. Therefore, the thermal expansion mismatch and the lattice mismatch between TiN-SS should lead to a compressive stress, which results in the shift of lattice planes to lower diffraction angles.

3.4 Microstructure of Ti and TiN thin films

The microstructure of the films was determined using field emission-scanning electron microscopy. The microstructure evolution of Ti films on Si and SS substrates are shown in figure 3.2. From the figure, it is evident that the surface of the films consists of complex microstructure. Films on Si substrates possess obelisk-like nanostructure and this feature is transformed into flower-like structure with increase in film thickness. On the other hand, films on SS substrates possess lenticular-like structures and the shape is turned to flower-like structure for 220 nm film. On both Si and SS substrates the flower-like structure with relatively little variation could observed for 220 nm film.
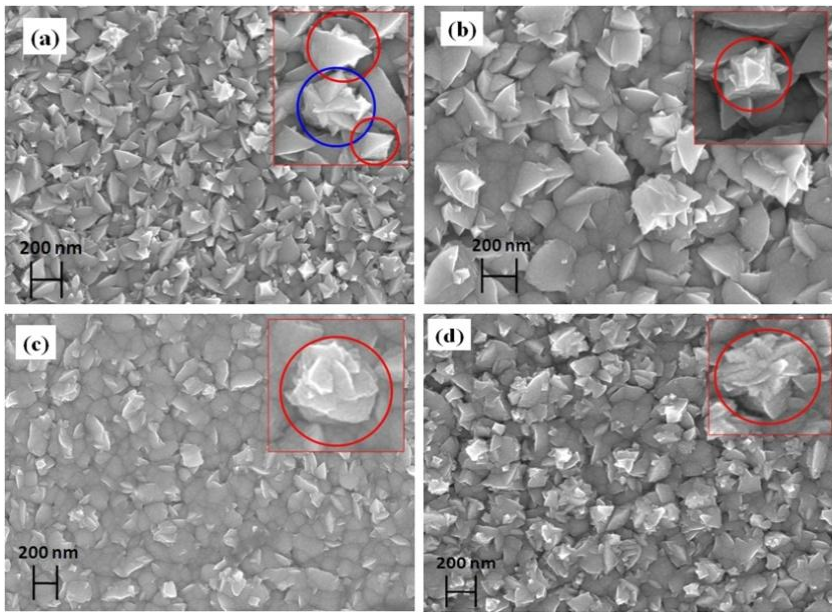

Figure 3.2 Field-emission scanning electron microscopy images of Ti thin films on Si and SS substrates. (a) 150 nm on Si (b) 220 nm on Si and (c) 150 nm on SS (d) 220nm on SS. The magnified features are shown as insert.
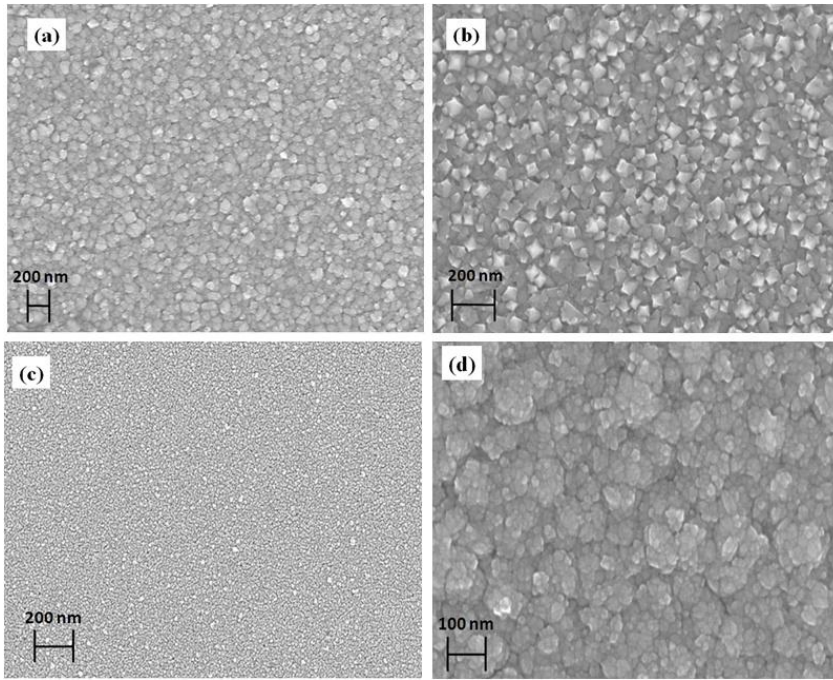
Figure 3.3 Field-emission scanning electron microscopy images of TiN thin films on Si and SS substrates. (a) 150 nm on Si (b) 220 nm on Si and (c) 150 nm on SS (d) 220nm on SS.

The microstructure of TiN thin films on Si and SS substrate is shown in figure 3.3. The morphology of the films on Si substrate changes from circularly shaped fine grains to a pyramid-like structure with increase the film thickness. The mean grain size in the 150 nm films is 80 nm and the diagonal distance of the pyramids in the 220 nm film is about 54 nm. In contract, the microstructure of TiN films on SS substrate consists of fine grains of spherical shape. The grain size in 150 nm film is 35 nm and the size increased to 50 nm for the film with thickness of 220

nm. It is evident that the microstructure evolution of Ti and TiN thin films are dependent on the substrate and the thickness of the films. The microstructure corresponds to zone-I type of the structure zone model, where the films growth temperature is much less than that of melting temperature of Ti and TiN thin films.

3.5 Mechanical properties

The hardness (H) and Young's modulus (Y) of Ti and TiN films were determined using nanoindentatio technique. Figures 3.4 (a) and (b) shows the load-displacement curves of Ti and TiN thin films of two different thicknesses (150 and 220nm) on Si and SS substrates respectively. The hardness and Young's modulus of the films were calculated from load-displacement curves using Oliver-Pharr method [150]. The detailed analysis of hardness and Young's modulus of the films was presented in table 3.3.
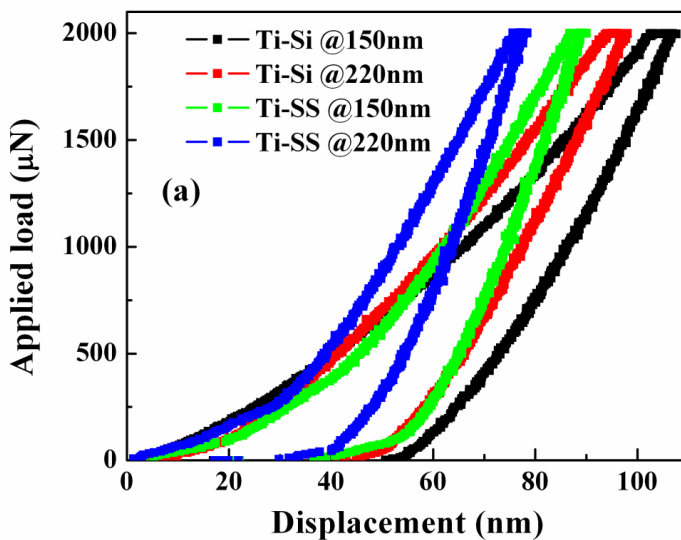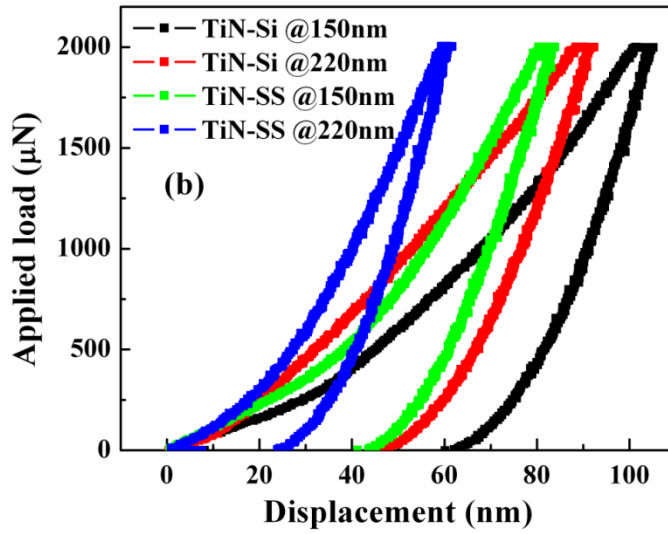
Figure 3. 4 load-displacement curves of 150 and 220nm (a) Ti and (b) TiN thin films on Si and SS substrates.

Table 3.3 Nanoindentation analysis of Ti and TiN thin films on Si and SS substrates

Film	Ti				TiN			
Substrate	Si		SS		Si		SS	
Thickness (nm)	150	220	150	220	150	220	150	220
Hardness (GPa)	8	10	10	12	16	21	20	27
Young's modulus (GPa)	82	105	100	132	200	230	220	250

The data revealed that the hardness of 150 and 220 nm thin Ti films on Si substrate is in the range of 8-10GPa and the value on SS substrate is in the range of 10-12GPa. Similarly, the Young's modulus on Si substrate is in the range 82-105GPa and on SS substrate is in the range 100-132GPa. There is a consistency in the data on both substrates in that the films with high thickness (220nm) have higher values of hardness and Young's modulus. Heterogeneous character of coating microstructure, elastic anisotropy, growth texture, and the underlying substrate including the interface have to be accounted for in the interpretation of nanoindentation measurement results. Previously Chang *et al.* [138] studied the structural and mechanical properties of RF sputtered Ti thin films. They reported that with variations in substrate temperature during film growth, the hardness values are spanning in the range 2-6 GPa and similarly the elastic modulus in the range 100-130 GPa for (002) textured films with residual stresses are presented. In the present case films with (100) orientation have higher hardness and Young's modulus that that of previously reported values. In addition, films on polycrystalline SS substrate with high compressive stress have higher values of hardness and Young's modulus. Stresses in a films promotes the texture evolution during film growth and hence the plastic yielding in anisotropic materials [151]. Therefore, films on SS substrate have high stress and exhibits enhance mechanical properties as the films on Si substrates.

Nanoindentation data of TiN thin films revealed that the hardness on Si substrate is in the range 16-21GPa and the value is on SS substrate is in the range 20-27GPa for 150 and 220nm films respectively. Similarly, Young's modulus on Si substrate is in the range 200-230GPa and on SS substrate is in the range 220-250GPa. Levy *at al.* [152]

reported that the mechanical properties of transition metal nitride are depends on the electronic structure, in addition to structure, microstructure and composition. In transition metal compounds, the chemical bond and cohesion energy relate to the mechanical properties, like Young's modulus and hardness [153]. High cohesion energy and high hardness values normally correlate with a covalent character of the bonding. Previously, it is reported that TiN films become harder with increasing N content because the covalent bonding between Ti and N atoms [154]. However, TiN films on SS substrate have higher hardness and Young's modulus than the films on Si substrates. This could be due to improved microstructure of the films on SS substrate.

3.6 Optical properties

The reflectance spectra of Ti and TiN thin films in the wavelength range 200-1500nm are shown in figures 3.5 (a) and (b). The reflectance spectra of Ti films on both Si and SS substrates show similar features. On both substrates with different thicknesses, the percentage of reflectance increased in visible region and saturated at about 35-45% in the near infrared region. In ultraviolet region (200-350 nm), the reflectance is less than 10% for all films. The reflectance spectra of TiN films exhibit a minimum in the visible region, beyond which the reflectance increases in the infrared region. In TiN thin films the reflectance minimum is strongly depended on the nitrogen composition. For stoichiometric TiN experimentally it is observed centered around 2.33 eV, which corresponding to charge transfer between the Ti3p and N2s states [155]. The reflectance minima of all films are centered on 2.30eV. However, in

the entire wavelength region the reflectance is higher for the 150nm thickness than for the 220nm thickness films on both substrates.
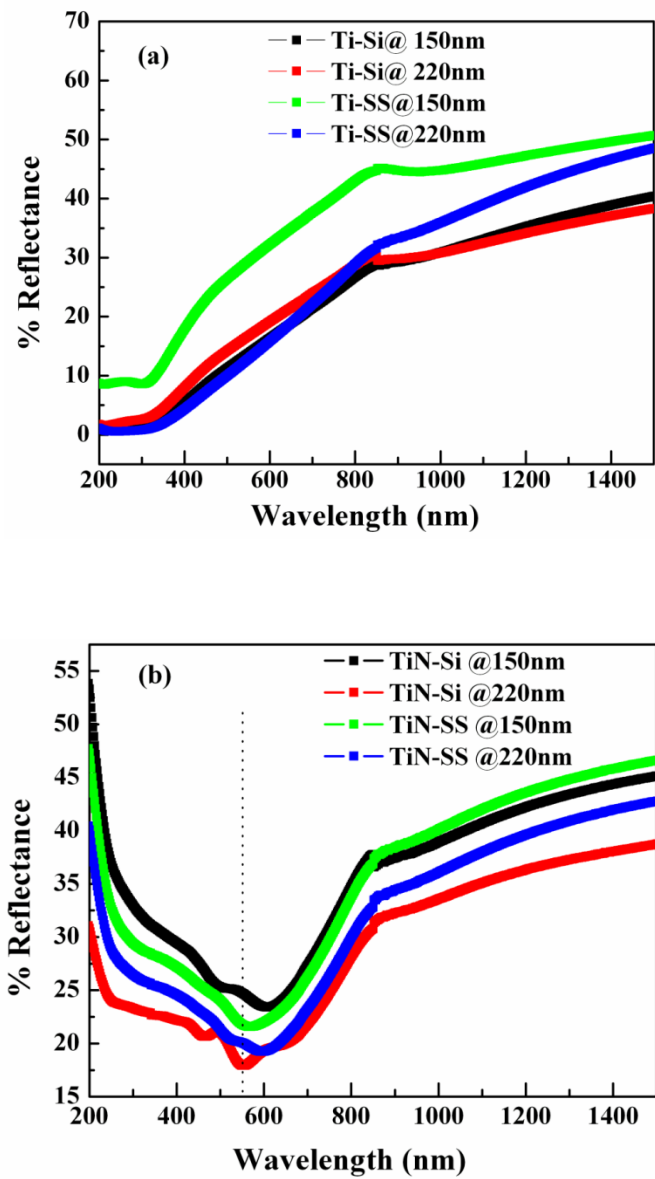

Figure 3.5 Reflectance spectrums of 150 and 220nm thin (a) Ti (b) TiN films on Si and SS substrates.

3.7 Electrical properties

The electrical resistivity of Ti and Ti N thin films are determined using four probe method and the data revealed that the films are highly conducting. The calculated values of electrical resistivity of Ti and TiN thin films are presented in table 3.4

Table 3.4 Analysis of electrical resistivity of 150 and 220nm thin Ti and TiN films on Si and SS substrates.

Film	Ti				TiN			
Substrate	Si		SS		Si		SS	
Thickness (nm)	150	220	150	220	150	220	150	220
Resistivity ($\mu\Omega$-cm)	64	54	80	72	160	210	120	180

On both substrates Ti films exhibits low resistivity in the range 54-80 $\mu\Omega$-cm and there is a marginal variation in the resistivity with film thickness. On the other hand, TiN films exhibits higher resistivity in the range 120-210 $\mu\Omega$-cm. It is observed that Ti films on both substrates of 150 nm thickness exhibit higher resistivity than the 220nm film. In contract, TiN films of thickness 150 nm exhibit lower resistivity than the 220 nm films. It has been reported that the electrical resistivity of TiN thin film is less than that of pure Ti and that is because of the intersection of the valence band of the Ti 3d electrons' with the Fermi level [5, 154]. But in the present case, the resistivity of TiN films is higher than that of Ti films; this could be polycrystalline nature of TiN thin films. It is known that the electrical resistivity of TiN_x thin films depends on defects, microstructure, composition and structure [156]. In polycrystalline TiN

films the resistivity arises due to grain boundary scattering [67]. From XRD studies it is observed that TiN films on Si and SS substrates are polycrystalline and Ti films is single crystalline. Therefore, grain boundary scattering could be the reason for higher resistivity of TiN films than for Ti films.

3.8 Summary

Pure metallic and stoichiometric TiN thin films of thicknesses 150 and 220 nm were deposited on single crystalline Si (311) and polycrystalline 316 LN nuclear grade stainless steel substrate by RF reactive magnetron sputtering. From the results presented above, it is observed that the addition of nitrogen to titanium makes new compound, which shows different structure, microstructure, mechanical, optical and electrical properties than that of pure titanium. For example, crystal structure of h.c.p Ti transform into cubic TiN. Cubic TiN shows polycrystalline nature and exhibits (111), (200) and (220) plane orientations, where as h.c.p Ti is a single crystalline and exhibit (100) orientation. Covalent bond between Ti and N make the compound stronger, as a result TiN film displays higher hardness and Young' modulus than that of Ti films. The charge transfer from Ti3p to N2s during compound formation is responsible for exhibit reflectance minimum in the reflectance spectrum and it occurred around 2.35eV for TiN films on Si and SS substrates. Grain boundary scattering is major reason for increase in resistivity of polycrystalline TiN films than that of single crystalline Ti films.

CHAPTER- 4

SUB-STOICHIOMETRIC TITANIUM NITRIDE THIN FILMS

Abstract

In this chapter, the chemical composition, crystal structure, morphology, mechanical, optical, electrical and optoelectronic properties of TiN_x thin films are reported as a function of substrate temperature. Thin films are deposited on a quartz substrate by RF magnetron sputtering in 100% nitrogen atmosphere and the substrate temperature was varied from room temperature to 600^oC. Thicknesses of the films were in the order of $150\pm10nm$. For XPS characterization TiN_x films were deposited on Si substrate and it was found that the composition of the films is substrate temperature dependent. The crystal structure of the films changed from tetragonal Ti_2N phase to cubic TiN as substrate temperature is increased. Average grain size, rms surface roughness, hardness and Young's modulus were increased with increasing substrate temperature. The measured highest values of hardness and Young's modulus were 17.5 ± 1 GPa and 120 ± 6 GPa for the film deposited at 600^oC. Electrical resistivity was higher for the amorphous film than for the crystalline films. Optical reflectance minima of the films shifted from the ultra-violet region having energy of 4.83 eV to the visible region corresponding to energy of 2.47 eV. The width of the transmittance band in the visible range varied with temperature between 460nm and 620 nm. All the films exhibited a PL (photoluminescent) single band in the middle of the visible region.

4.1 Introduction

Owing to its hardness and high temperature stability, titanium nitride has found many applications in industry. It is used, for example as a surface coating on cutting tools and decorative coating on ornaments because of its attractive gold color [157, 158]. The physical and chemical properties of TiN_x thin films are strongly dependent on composition, crystal structure, microstructure and experimental conditions being used. High quality and improved properties of films can obtain by careful control of the experimental conditions. In general, the composition of TiN_x thin films is governed by varying nitrogen partial pressure. According to Holmberg [42], when x in TiN_x is less than or equal to 0.2, the distorted α-TiN_x (tetragonal) phase is formed. When $0.2 < x < 0.49$, a mixture of FCC α-Ti (N) and tetragonal Ti_2N is formed. In the narrow range $0.49 \leq x < 0.52$, ε-Ti_2N alone is formed. In the range $0.52 \leq x < 0.60$, both ε-Ti_2N and FCC δ-TiN_x are formed. When $x>0.6$, only δ-TiN_x phase is present. The phase diagram of Ti-N compound [159] reveals that the stoichiometry of TiN_x is also governed by temperature at a well defined nitrogen partial pressure.

In this chapter, the influence of substrate temperature on structure, composition, microstructure, mechanical, optical, electrical and photoluminescence properties of anion (nitrogen)-deficient titanium nitride thin films, is reported.

4.2 Experimental conditions

Experimental parameter	TiN
Target material	2 inch diameter Ti
Substrates	quartz
Working pressure	5×10^{-2} mbar
Sputtering (reactive) gas	100 % nitrogen
RF power	100 Watt
Distance between target and substrate	60 mm
Substrate temperature	RT, 200, 400, 600°C
Deposition time	120 min

Thickness of the films is 150±10 nm

4.3. Influence of substrate temperature on crystal structure

XRD patterns of 150nm thin TiN_x films deposited at different substrate temperatures are as shown in figure 4.1. The low intensity of the x-ray diffraction peaks as well as their large widths clearly indicates that films are not fully crystalline and that a large fraction of the films is still amorphous. Film deposited at room temperature shows a single crystalline peak corresponding to tetragonal δ'-Ti_2N (200) (see for comparison JCPDS file number 77-1893). However, the Bragg angle of the plane (200) had shifted to a lower value. This is traceable to the distortion in the metastable phase due to the fact that sputtering is a non-equilibrium process, and the interstitial sites in hcp α-Ti are smaller than the size of the nitrogen atoms (1.19 A^o and 1.35A^o respectively) [3,160]. Close examination of the XRD pattern of the film deposited at 200°C revealed that the tetragonal Ti_2N phase had completely disappeared, but instead crystallization of cubic TiN_x of (111) orientation had started. In

the film deposited at 400°C, cubic TiN_x of (111), (200) and (220) orientations were observed. At 600°C, the intensity of the Bragg reflections had increased in comparison with the film deposited at 400°C, which is evidence for improved crystallinity. The stoichiometry continued to remain TiN_x (x<1.0), but only crystallites of (220) orientation could be observed. It is reported [161] that the surface energy, S, along different planes in TiN have the following order $S_{100} < S_{110} < S_{111}$ whereas the strain energy follows the order $U_{111} < U_{220} < U_{200}$ [162]. The change in preferred orientation of the films can be attributed to the competition between surface and strain energies at different temperatures. The free energy minimization process results in the films exhibiting orientation along the plane that has the lowest total free energy, which clearly seems to be substrate-temperature dependent.

These results clearly reveal that at 200°C, the tetragonal Ti_2N phase starts transforming to the cubic TiN_x phase, which continued to remain cubic TiN_x till 600°C. More significantly, 'x' was a function of substrate temperature and its value increased towards unity, as the substrate temperature was raised. Figure 4.2 (a) is a bright field transmission electron microscopy (TEM) image and figure 4.2 (b) is a selected area electron diffraction (SAED) pattern, both from a Ti_2N thin film deposited at room temperature. Microstructure analysis revealed that the grain size was ~14 nm and the lattice planes belonged to ε-Ti_2N. The lattice parameter was 4.22 A^o and 4.23 A^o for the films deposited at 400°C and 600°C respectively. In contrast, stress-free stoichiometric TiN (N/Ti=1) has a lattice parameter of 4.24 A^o [163-165]. The smaller value of the lattice parameter indicates that the film composition was sub-

stoichiometric ($x<1$) and nitrogen-deficient. It is also known that the lattice parameter increases with increasing (N/Ti) ratio [56, 62].
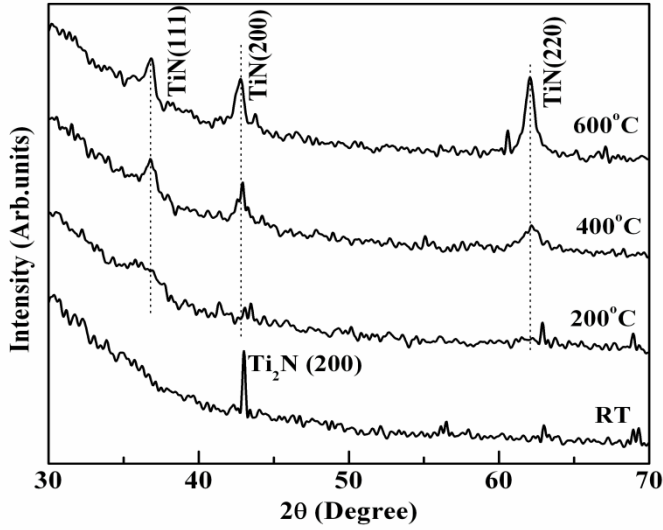

Figure 4.1 X-ray diffraction pattern of TiN_x thin films deposited at different substrate temperatures.
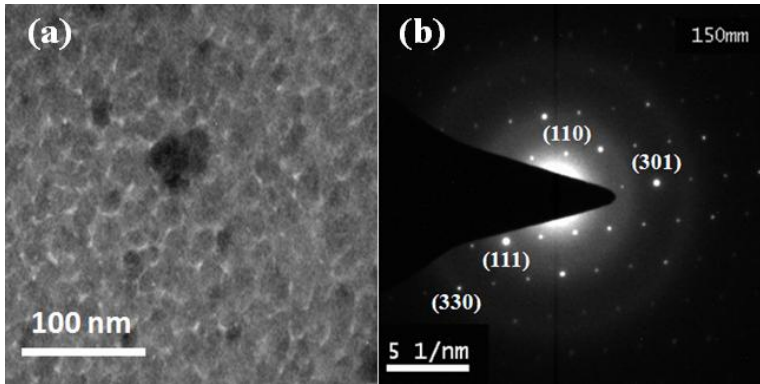

Figure 4.2 (a) Transmission electron microscopy bright field image (b) selected area electron diffraction image of Ti_2N thin film deposited at room temperature.

4.4. Influence of substrate temperature on composition: TiN$_x$ films on Si substrate

The stoichiometry of TiN$_x$ thin films is determined using x-ray photoelectron spectroscopy (XPS). XPS spectra of the films exhibited the characteristic Ti-2p and N-1s peaks at binding energies of 458.5 eV and 397.8 eV respectively. High-resolution XPS spectra of Ti-2p and N-1s peaks are as shown in figures 4.3 (a) and (b). For the film deposited at room temperature, Ti-2p$_{3/2}$ and Ti-2p$_{1/2}$ lines appeared at 459.0 eV and 464.8 eV. It is clear that Ti-2p$_{3/2}$ and Ti-2p$_{1/2}$ core levels obtained from the TiN$_x$ compound are shifted to higher binding energy values with respect to the Ti-2p$_{3/2}$ line (453.6 eV) and Ti-2p$_{1/2}$ line (459.7 eV) compared with those for pure titanium [166]. From figure 4.3 (b), it is evident that the N-1s peak, which appears at 400.1 eV, is shifted to a higher binding energy region from the free nitrogen core level position of 399.0 eV. These shifts could be attributed to the formation of titanium oxide on the surface of the film at high temperatures. It is clear from the XPS data that oxidation is present only in the films deposited at room temperature and 500°C and that oxidation is restricted to the film surface. For the film deposited at 300°C, no change was observed in Ti 2p$_{3/2}$ and Ti 2p$_{1/2}$ core levels, but the N1s core level shifted to a lower binding energy (397.2 eV), confirming the formation of titanium nitride with an N/Ti ratio of 0.52. For the film deposited at 500°C, both the Ti 2p$_{3/2}$ as well as the Ti 2p$_{1/2}$ levels shifted to higher binding energy. The N1s core level appeared at 399 eV which reveals the formation of near-stoichiometric TiN with an N/Ti ratio of 1.1. As described by Galvanetto et al [167], the nitrogen content was measured as the area ratio between the N 1s and the whole region of the Ti 2p signal. Figure 4.3 (c) shows

the increase in N/Ti ratio with substrate temperature, this is evident that the variation in composition of TiN_x thin films is substrate temperature dependent. Thus, x-ray diffraction and x-ray photoelectron spectroscopy studies confirm clearly that x in TiN_x films is varying in the following manner $x_{600°C} > x_{400°C} > x_{200°C}$.
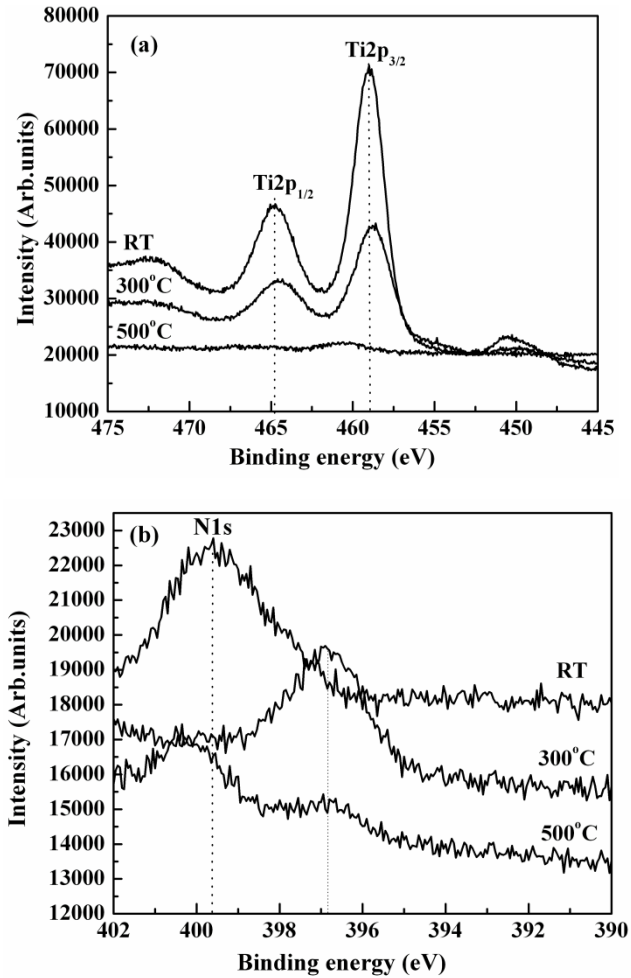

Figure 4.3 X-ray photoelectron spectra of (a) Ti2p and (b) N1s states of TiN_x thin films deposited at different substrate temperature on Si(311) substrate.
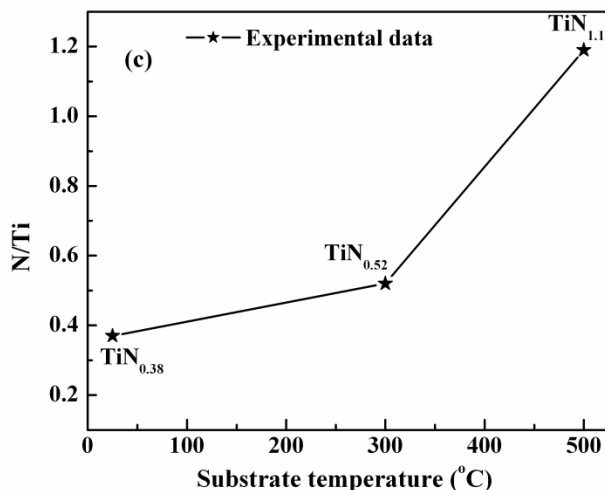
Figure 4.3 (c) Variation of N/Ti ration as a function of substrate temperature calculated from the XPS spectra.

4.5. Microstructure

Contact mode atomic force microscopy (AFM) images of TiN_x thin films deposited at different substrate temperature are shown in figure 4.4. Surface morphology of all films consists of spherical shaped grains with different sizes over a $1\mu m \times 1\mu m$ scan area. The average grain size of Ti_2N film, deposited at room temperature is 21 ± 8 nm and it increased to 52 ± 13 nm as the substrate temperature increased to $600^{o}C$. The rms surface roughness also follows the same trend, increasing from 0.86 ± 0.4 to 4.20 ± 1.2 nm as the substrate temperature increased from room temperature to $600^{o}C$. The complete microstructural analysis of TiN_x thin films are reported in table 4. 1. The increase in grain size with substrate temperature of TiN_x thin films is attributed to the enhancement of adatom surface mobility and atomic diffusion at high substrate temperature,

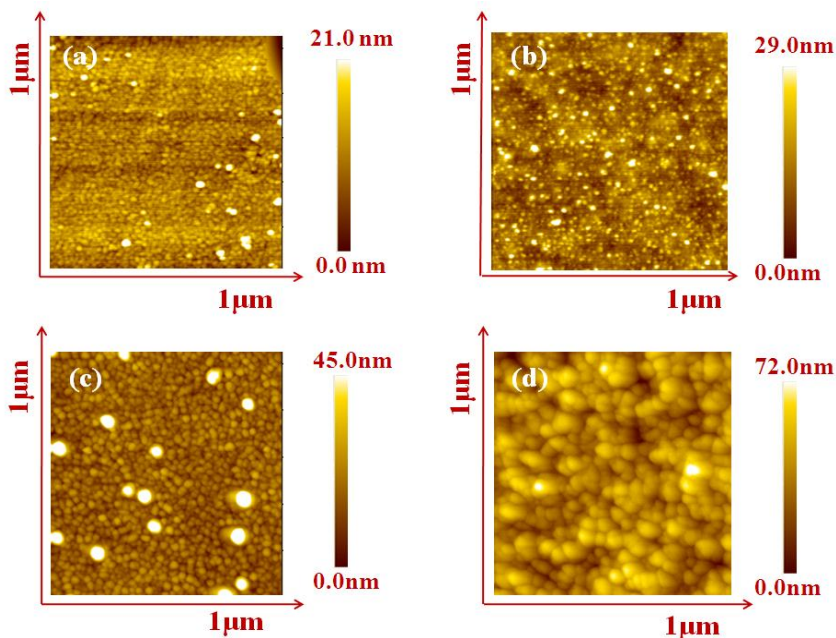thereby enhancing the grain growth which leads to increase the grain size [168].

Figure 4.4 Contact mode atomic force microscopy images of TiN$_x$ thin films deposited at (a) room temperature (b) 200°C (c) 400°C and (d) 600°C.

Table 4. 1 Microstructural details of the TiN$_x$ thin films at different substrate temperature

Substrate temperature (^{o}C)	Grain size (nm)	RMS surface roughness (nm)
RT	21±8	0.86±0.4
200	23±9	1.00±0.5
400	28±11	3.30±1
600	52±13	4.20±1.2

The grain size distributions of TiN_x thin films are shown in figure 4.5, from which it is observed that the FWHM of the distribution increased with increase in substrate temperature. The increase in the FWHM of the size distribution is a consequence of Ostwald-ripening process with increase in temperature [169].
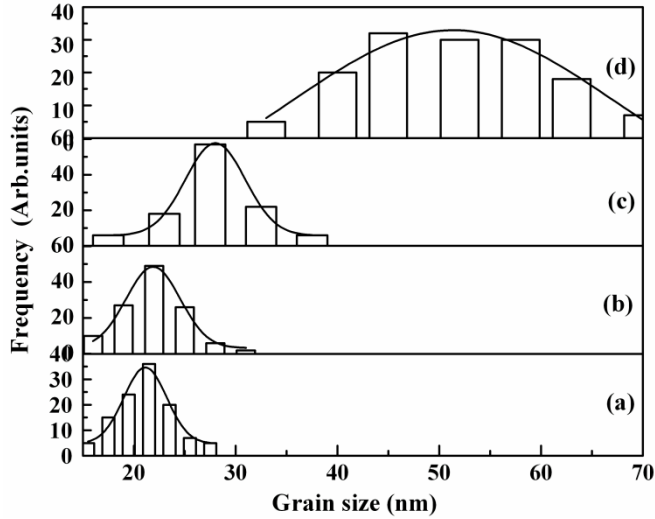
Figure 4.5 Distribution of grain sizes of TiN_x thin films deposited at (a) room temperature (b) 200°C (c) 400°C and (d) 600°C.

4.6 Nanomechanical properties

Nanomechanical properties, i.e., hardness and Young's modulus of TiN_x thin films were determined using nanoindentation technique. The load-displacement curves as a result of the indentation of the films are depicted in figure 4.6. The hardness and Young's modulus are derived from figure 4.6 using Oliver-Pharr method [150].
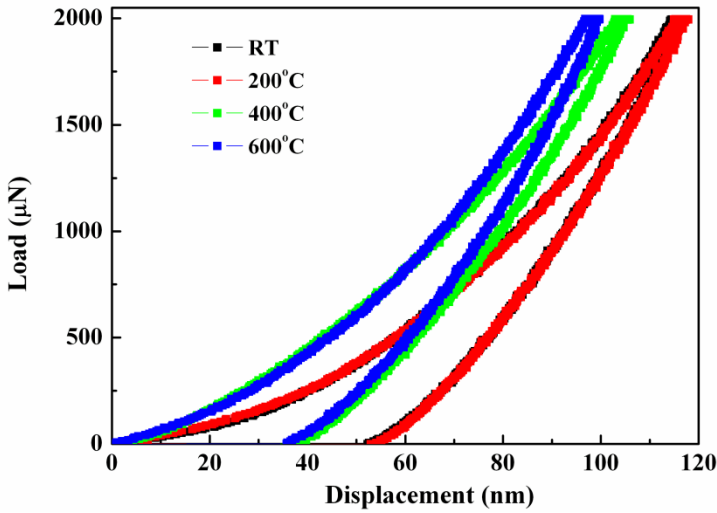
Figure 4.6 Load-displacement curves of TiN$_x$ thin films deposited at different substrate temperatures.

The values of hardness and Young's modulus of the TiN$_x$ thin films with increasing substrate temperature are displayed in figure 4.7. The data reveal that the hardness of the Ti$_2$N film, deposited at room temperature is 6.8±0.5 GPa. The hardness increases with increasing substrate temperature and attains a maximum value of 17.5±1.3 GPa for film deposited at 600°C. Similar behavior is observed in the variation of Young's modulus with substrate temperature. It increased from 91±2 to 120±6 GPa as the substrate temperature increased from room temperature to 600°C. This finding is in line with the well-known relation that hardness scales as Young's modulus.
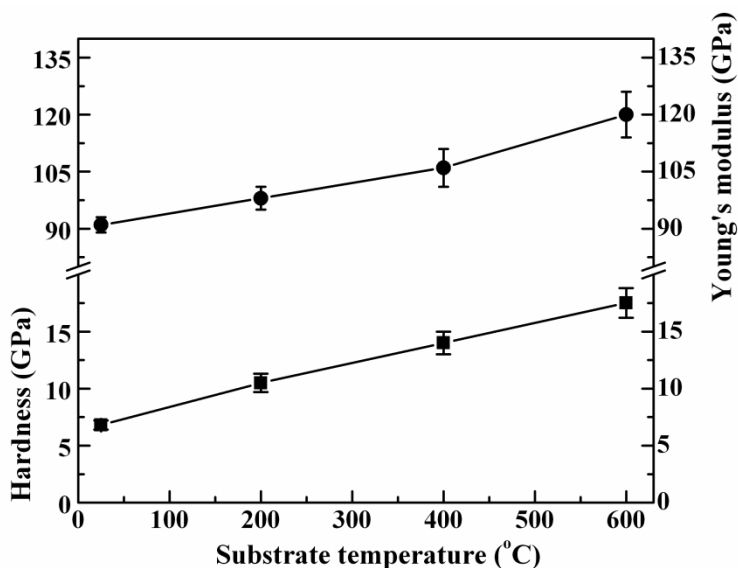
Figure 4.7 Variation of hardness and Young's modulus of TiN_x as a function of substrate temperatures.

Several first principle calculations and experimental results have showed that the high hardness in the stoichiometric TiN is due to a favourable occupancy of the hybridized Ti 3d (e_g) and N2p states leading to the covalent character [152]. XRD and XPS results in the current study showed that the deposited films are sub-stoichiometric. A high density of nitrogen vacancy is the most significant defect in the sub-stoichiometric TiN. Therefore, the mechanical properties of TiN_x are expected to change appreciably in the composition range investigated here, because of the change in electronic binding mechanism due to the existence of nitrogen vacancies [137, 170]. As the nitride composition

increases, the lattice constant of TiN_x increases and the covalent character in the Ti-N bonding become stronger [62].

The nitrogen composition in the films is increased with increase in substrate temperature, which leads to strong covalent bond between Ti-N atoms. As a result the hardness and Young's modulus of TiN_x films are increased with increase substrate temperature.

4.7 Electrical properties

Figure 4.8 shows the variation of electrical resistivity of TiN_x thin film as a function of substrate temperature. From the figure, it is revealed that the electrical resistivity is strongly dependent on substrate temperature. The resistivity of Ti_2N thin film, deposited at room temperature is 302±15 mΩ-cm. Interestingly, it increased to 485±24 mΩ-cm for the amorphous film deposited at 200°C. The resistivity decreased to 102±5 mΩ-cm for the film deposited at 400°C and it is further decreased to 720±0.036 μΩ-cm at 600°C. It is known that the electrical resistivity of TiN_x thin films depends on defects, microstructure and composition. The defects in sub-stoichiometric TiN_x are nitrogen vacancies. Therefore, the resistivity of sub-stoichiometric TiN_x is mainly due to two kinds of carrier scattering, one due to nitrogen atoms randomly distributed at vacant interstitials, another attributable to grain boundary scattering [67]. The increase in resistivity of amorphous film deposited at 200°C is attributed to the lack of long range order. Electron scattering from grain boundaries of randomly oriented crystals in the film leads to increase in resistivity. The films deposited at 400 ^{o}C undergo a transformation in to the cubic structure. The density of defects in the

cubic TiN_x is low due to the improved crystallinity of the film. As a result the electron scattering rate is lower in crystalline film compared to films that lack long range order. The improvement of crystallinity in tetragonal and cubic TiN_x films leads to decrease in resistivity.
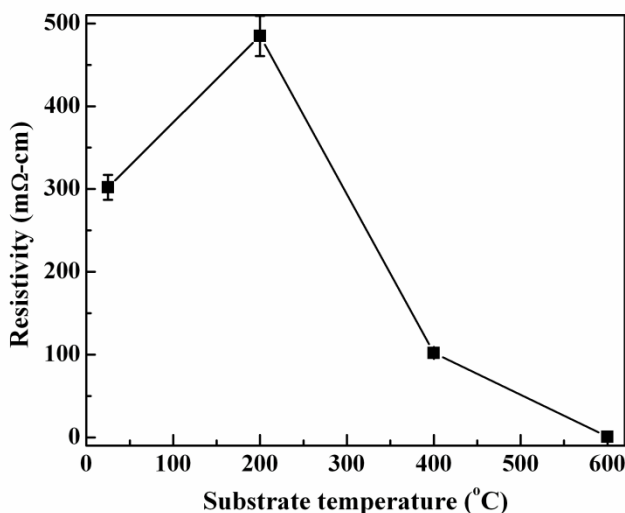

Figure 4.8 Variation of electrical resistivity of TiN_x thin films as a function of substrate temperature.

4.8 Optical properties

The measured specular reflectance spectra of TiN_x films in the wavelength range 190-1500 nm as shown in figure 4.9. Films deposited at room temperature and 200^oC exhibit a dip in the reflectance around 4.83 eV. There is a red-shift in the position of this feature to 3.98 eV at 400^oC. At 600^oC, there is a transformation in the specular reflectance behavior. The reflectance dip disappears completely and is replaced by a short wavelength edge at 4.12 eV, a long wavelength edge at 2.47 eV and an almost constant reflectance over this wavelength range. The

appearance of the absorption peak at 4.83 eV indicates non-stoichiometry in the films up to a temperature of $400^{o}C$. This is inferred from the fact that the absorption peak for stoichiometric TiN occurs at 2.33 eV and deviations from this value are due to nitrogen non-stoichiometry [64, 155]. The edge at higher energy in the films deposited at $600^{o}C$ corresponds to an inter-band transition, while the lower energy band represents a charge transfer excitation [155].

Thus the shift in the reflectance minima of the deposited TiN_x from 4.83 to 2.47 eV, signifies that the composition changed from x~0.5 to x→1, as the substrate temperature increased from room temperature to $600^{o}C$.
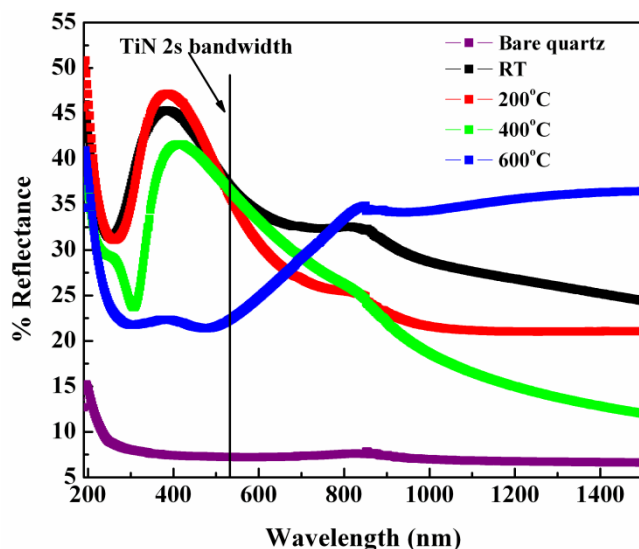
Figure 4.9 Specular reflectance spectra TiN_x thin films with uncoated bare quartz substrate deposited at different substrate temperature.
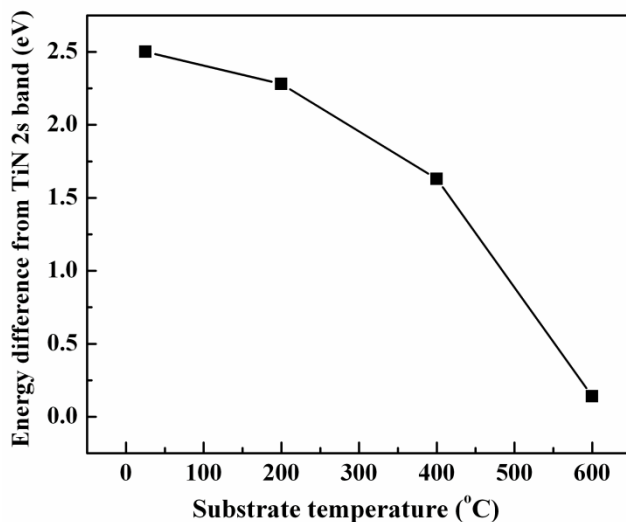
Figure 4.10 Variation of absorption band edge energy difference of TiN$_x$ thin films from absorption edge of stoichiometric TiN (2.33 eV).

Figure 4.10 shows the energy difference of the absorption edge of the TiN$_x$ thin films compared with the band width of a fully crystalline, stoichiometric TiN film. With increasing substrate temperature, the energy difference became increasingly less decreasing from 2.5 eV to 0.14 eV. As in all cases, the energy difference is positive, i.e., the energy minimum of the presently formed films were greater than that of stoichiometric TiN, it is evident that all the films deposited were nitrogen deficient (It is known that Ti$_2$N/TiN$_x$ has higher plasma edge energy than TiN [155]).

Spectral transmittance of TiN$_x$ thin films in UV, visible and IR wavelengths depends on the N/Ti ratio [171]. The transmittance spectra for films deposited at different substrate temperatures in the wavelength range of 190-1500 nm is shown in figure 4.11. Room temperature

deposited Ti_2N film was transparent, did not show any interference fringes and recorded a high transmittance of ~ 90% in the near infra-red region. It has been reported that there is a marked increase in the infra-red transparency with increasing non-stoichiometry in the TiN_x thin films [172]. TiN_x thin films deposited at 200^oC recorded a high percentage of transmittance only in the visible region (470-640 nm). The transmittance percentage in the UV and IR regions was clearly low. In contrast, in stoichiometric TiN the UV and IR regions are completely blocked [172]. With increasing substrate temperature, the transmittance percentage decreased and the onset of the region of transmittance above the band gap was shifted towards the longer wavelengths (lower energy). There is a suggestion that an increase in the number of free electrons with increasing substrate temperature is responsible for the decrease in the peak transmittance (due to an increase in the reflectivity of the films) [44]
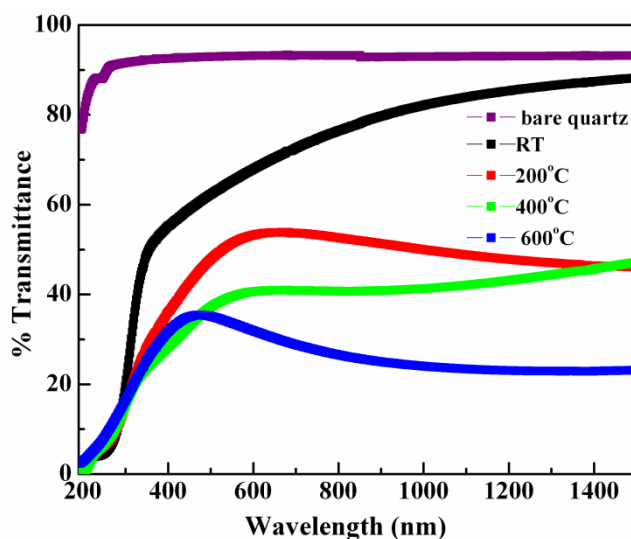

Figure 4.11 Spectral transmittance spectra TiN_x thin films with uncoated bare quartz substrate deposited at different substrate temperature.

Optical constants

The optical constants, the refractive index (n) and the extinction coefficient (k) were calculated using the Point-wise Unconstrained Minimization Approach (PUMA) software [173, 174]. Prior knowledge of n and k values was used to fit the measured specular reflectance curves. A typical fit of TiN_x films reflectance spectra is shown in figure 4.12. Clearly the procedure yields an extremely good fit between the calculated and the measured spectra.
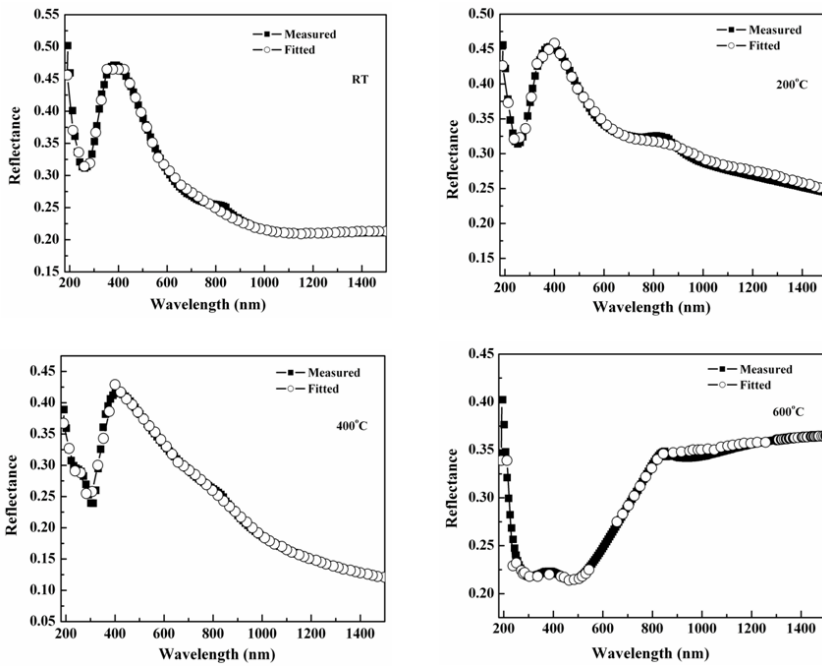

Figure 4.12 Measured reflected spectra of TiN_x thin films at different substrate temperature were fitted using PUMA software.

After successfully fitting the measured reflectance spectra the software provides the data of optical constants $n(\lambda)$ and $k(\lambda)$ in the entire wavelength range. Figure 4.13 (a) and (b) shows the variation of refractive index and extinction coefficient in the wavelength range 200-

1500 nm of TiN_x thin films for different substrate temperature. From the figure, it is observed that there is an increase in the values of n and k with an increase in the substrate temperature. The n value at a wavelength of 600 nm is 1.98 for the film deposited at ambient temperature and 2.11, 2.24 and 2.47 at 200, 400 and 600 $^\circ$C respectively. The corresponding k values were 0.2, 0.56, 1.48 and 1.8 for the films deposited at room temperature, 200, 400 and 600 $^\circ$C respectively. The extinction coefficient is directly related to the conductivity of the material through an absorption coefficient $\alpha=4\pi k/\lambda$. Therefore, increase in extinction coefficient implies that increase in conductivity of TiN_x thin films with in substrate temperature. This also have good agreement with dc four probe measurement, where the electrical resistivity of TiN_x thin films was decreased with increase in substrate temperature. The peak in the extinction coefficient could indicate the presence of Plasmon resonance at the wavelength, ~ 500nm, reported by earlier workers [175].
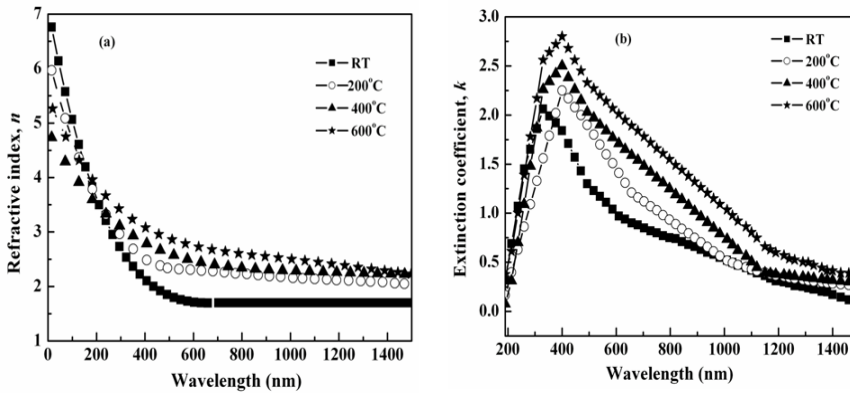

Figure 4.13 Variation of (a) refractive index (b) extinction coefficient of TiN_x thin films deposited at different substrate temperature.

4.9. Photoluminescence

The Photoluminescence spectrum of the deposited TiN_x thin films is shown in figure 4.14. All the films exhibited a PL single band in the middle of the visible region. The intensity decreased with increasing substrate temperature. As seen earlier, all the films were nitrogen-deficient. It was also pointed out that the higher energy absorption edge of the films involves inter-band transitions and the low energy absorption edge is due to charge transfer excitation [155, 176]. The band gaps suggest that the films deposited at room temperature and $200^{o}C$ are semi-conducting, while the film deposited at $400^{o}C$ and $600^{o}C$, although nitrogen deficient, are conducting. It has been suggested that the nitrogen deficiency in the films coupled with the magnitude of the optical band gap energy, is indicative of the recombination between the electrons bound to the N vacancies and the holes in the valance band-the so called donor-bound excitons [177]. With increasing substrate temperature, the FWHM of the peaks increased and the peak shifted towards the higher wavelengths.
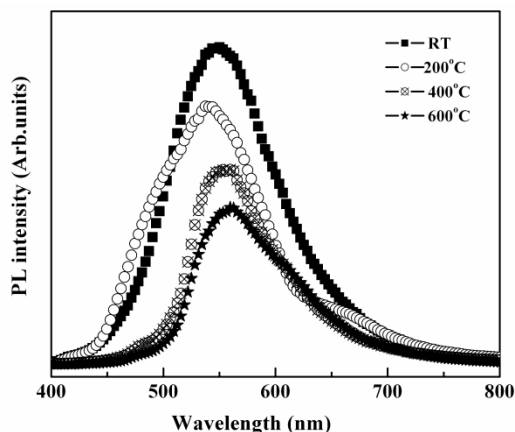

Figure 4.14 Photoluminescence spectra of TiN_x thin films deposited at different substrate temperature.

In addition to quartz substrate, TiN_x thin films are also deposited on borosilicate glass and sapphire substrate for reproducibility of PL spectra. PL results on these substrates also shown good luminescence properties. Figure 4.15 (a) and (b) shows the photoluminescence spectra of TiN_x thin films on glass and sapphire substrates deposited at room temperature and 200^oC. Comparison with the PL spectra on quartz substrates, it is seen that there is a slight blue shift in the peak position. This shift can be attributed to the changes in stoichiometry on different substrates.
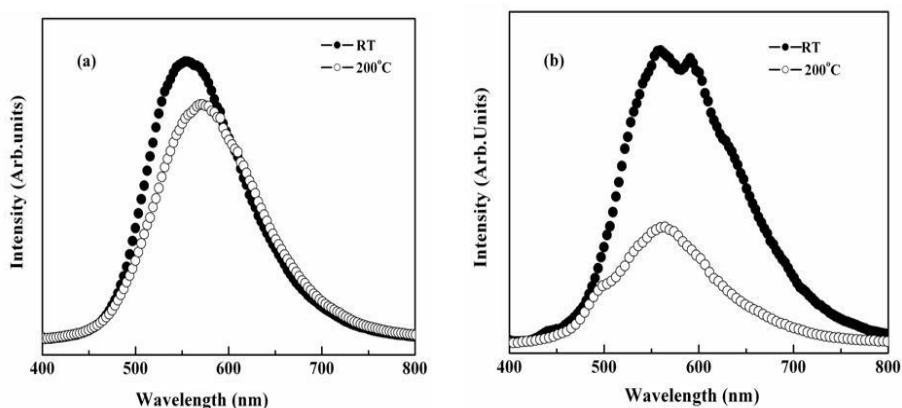

Figure 4.15 Photoluminescence spectra of TiN_x thin films on (a) glass and (b) sapphire substrates

4.10 Summary

In summary, the growth of single phase sub-stoichiometric TiN_x thin films at fixed nitrogen partial pressure and varying substrate temperature by RF reactive magnetron sputtering in 100% N plasma is reported. It was shown that the composition, structural, microstructure, mechanical and optical properties like spectral transmittance and reflectance of TiN_x thin films depend on the substrate temperature. The

correlations between the structural and optical properties of deposited films established in a mutually consistent manner using TEM, spectral transmittance, reflection plasma band and photoluminescent band indicate that the composition of TiN_x thin films had changed from non-stoichiometric, tetragonal Ti_2N phase to nitrogen deficient, cubic stoichiometric TiN phase with an increase in the substrate temperature. TiN_x films displayed good mechanical properties and also exhibits luminescence behavior. Therefore, in addition to mechanical applications, TiN_x thin films can also be used for optoelectronic applications.

CHAPTER-5

Nb-SUBSTITUTED TITANIUM NITRIDE THIN FILMS

In this chapter, the composition, structure, nanomechanical and nanotriboloical, optical, electronic, electrical and vibrational properties of TiN thin films are studied as function of Nb concentration. $Ti_{1-x}Nb_xN$ thin films in the whole composition range ($0 \le x \le 1$) were deposited onto polycrystalline nuclear grade 316LN nuclear grade stainless steel substrates by RF magnetron sputtering in 100% N_2 plasma. It is demonstrated that all the properties studied are dependent on the Nb concentration, x, and exhibit a threshold at x=0.5 in the case of mechanical and optical properties. Grazing incident x-ray diffraction results revealed that Nb is soluble in TiN up to x=0.77. From x=0.26 to x=0.77, these films stabilized in rock salt structure with (111) orientation. The hardness and Young's modulus increased while the friction coefficient and wear volume decreased with increasing Nb concentration. The highest hardness achieved was 31GPa for x=0.77. The films showed a broad reflectance band, with a minimum in reflectance that shifted to shorter wavelengths as a function of increasing x. The position of the reflectance minima shifted from 2.33 to 3.0 eV with an increase in x from 0 to 0.77 and the shift is negligible for Ti-rich films, i.e. for $x < 0.5$, while for Nb-rich films, $x > 0.5$, the shift is more significant. Reflectance spectra of the films in the energy range 1.5 to 5.5 eV are fitted by a model dielectric function based on Drude-Lorentz oscillators. The real part of the dielectric function is characterized by screened plasma energy of 2.25 eV for values of $x < 0.5$ (~TiN) and 3.25 ± 0.2 eV for $x > 0.5$ (~NbN). The electrical resistivity was decreased from 206 to 56 $\mu\Omega$-cm as increase x from 0 to 0.77. Nb substitution in TiN results in first-order Raman scattering.

5.1 Introduction

The properties of metal substituted titanium nitride films are dependent strongly on the nature of the substituting metal. Several reports are available on Zr and Ta substituted TiN [70, 73, 74, 78, 80, 178]. However, Zr shares similar valence electron (d^2s^2) configuration as Ti, whereas Ta has the valence electron configuration (d^3s^2). In both the compounds, $Ti_{1-x}Zr_xN$ and $Ti_{1-x}Ta_xN$, improvements in mechanical, electrical and optical properties were observed. This is due to the fact that the substituent metal (Me) is completely soluble in TiN. Furthermore, the pseudo-binary compounds $Ti_{1-x}Zr_xN$ and $Ti_{1-x}Ta_xN$ crystallize in the rock salt structure and are stable over the whole composition range of $0 \leq x \leq 1$. The change in electronic structure and bonding mechanism in these compounds could result in the variations in physical and chemical properties [90, 91].

In this chapter, the effect of Nb (valence electron configuration is d^4s^2) concentration on the composition, microstructure, and structure, mechanical, tribological, optical, electrical, electronic and vibrational properties of titanium nitride thin films is studied. $Ti_{1-x}Nb_xN$ thin films, over the entire range of x from 0 to 1, were deposited on polycrystalline 316LN nuclear grade stainless steel substrates. Significantly, these properties show two distinct regions of behaviour, one of which corresponds to the Ti rich compositions and the other to the Nb rich compositions with the threshold value for transition in mechanical and optical behavior being centered around $x=0.5$. The results are used to draw important conclusions regarding the crystal structure, electronic structure, mechanical and optical properties of $Ti_{1-x}Nb_xN$ thin films.

5.2 Experimental conditions

Experimental parameter	TiN
Target material	Ti & Nb (99.99 % purity)
Substrate	316 LN nuclear grade stainless steel
Working pressure	5×10^{-2} mbar
Sputtering (reactive) gas	100 % nitrogen
RF power	100 Watt
Distance between target and substrate	50 mm
Substrate temperature	$250^{o}C$
Deposition time	180 min

In the case of Ti-rich films Nb fractions was varied on Ti target surface. On the other way Nb-rich films Ti fractions was varied on Nb target surface. Thickness of the films is 500 ± 20nm.

5.3 Composition and microstructure

Chemical composition of $Ti_{1-x}Nb_xN$ thin films was determined using energy dispersive x-ray (EDX) spectroscopy. The composition (x) in the films was controlled by varying the Nb fractions on Ti target. Figure 5.1 shows the EDX spectra of the films in the entire composition range ($0 \leq x \leq 1$). From the EDX spectra it was inferred that all films have a nitrogen percentage in the range of 48 to 52 at. %. The unidentified peaks in the EDX spectra correspond to the 316 LN SS substrate. No O or C contamination was detected in the bulk of the films. From the EDX analysis, the values of x in the films were calculated as 0, 0.26, 0.41, 0.58, 0.77 and 1.
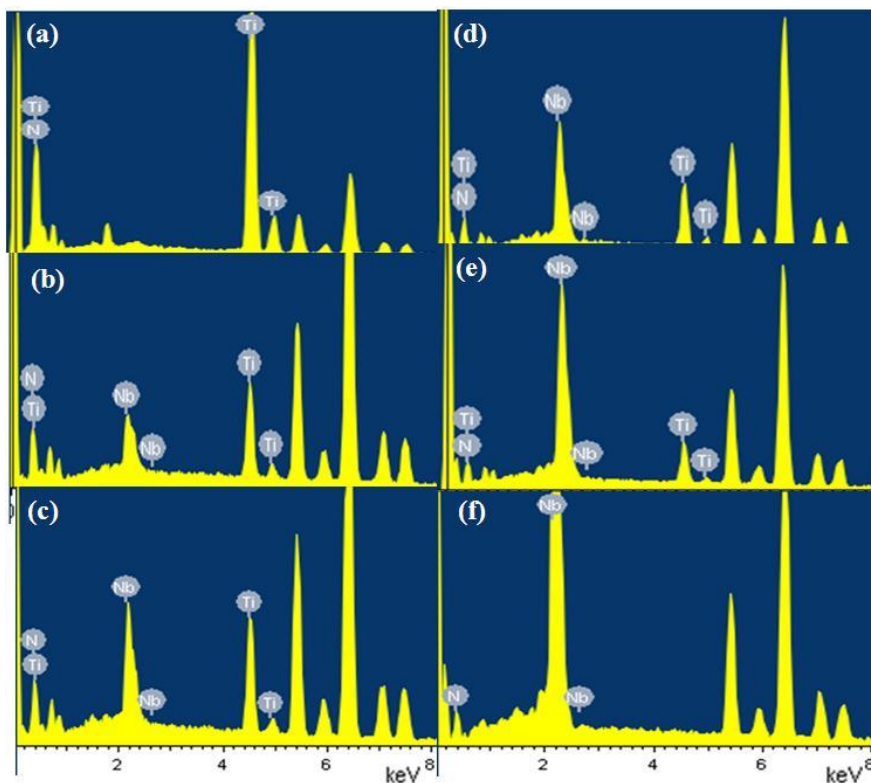
Figure 5.1 Energy dispersive x-ray spectroscopy spectrum of $Ti_{1-x}Nb_xN$ thin films (a) $x = 0$, (b) $x = 0.26$ (c) $x = 0.41$ (d) $x = 0.58$, (e) $x = 0.77$ and (f) $x = 1$

Microstructure of the films was determined using field emission scanning electron microscopy (FE-SEM). The FE-SEM images of $Ti_{1-x}Nb_xN$ thin films are shown in figure 5.2. The FE-SEM images reveal that the films are very smooth and the grain very small. The average grain size increased from 25 ± 4 to 35 ± 5 nm for $x=0$ to $x=0.77$ respectively and then decreased to 30 ± 3 nm for $x=1$. There were not much noticeable difference in the grain size distribution as a function of x.
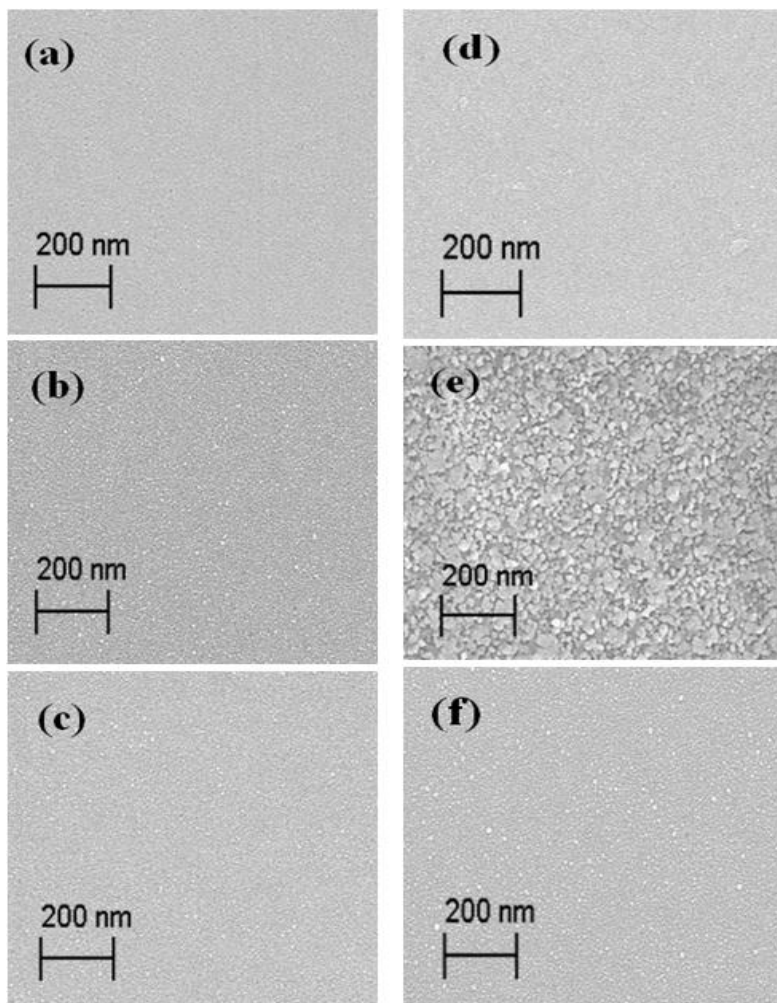
Figure 5.2 Field emission-scanning electron microscopy images of $Ti_{1-x}Nb_xN$ thin films (a) x = 0, (b) x = 0.26 (c) x = 0.41 (d) x = 0.58, (e) x = 0.77 and (f) x = 1

5.4 Structure

Crystal structure of $Ti_{1-x}Nb_xN$ thin films was determined using grazing-incidence x-ray diffraction (GI-XRD). The GI-XRD patterns of the films for different values of x are shown in figure 5.3. It is evident that the TiN film (x=0) crystallizes in the rock salt structure, with (111) orientation. For x=0.26, intensity of the reflection from the (111) plane had increased, but it was also accompanied by a shift in the peak position to a lower diffraction angle. At a higher Nb substitution in the films, *i.e.* for x=0.41, 0.58 and 0.77 [figures 5.3 (c), (d) and (e)], the intensity of the reflection from the (111) plane continued to increase, with the 2θ position progressively shifting to lower diffraction angles. The shift in position of the (111) reflection is attributed to an increase in the substitution of Nb into the Ti lattice sites of the structure. When Ti atoms are replaced by Nb atoms, the crystal lattice undergoes a distortion, since the radius of the Ti atom is smaller than that of the Nb atom [101]. Moreover, the difference in the atomic sizes of Ti and Nb atoms gives rise to an internal stress/strain in the film. At x=0.77 (Figure 5.3 (e)), in addition to the reflection from the (111) plane, a reflection from the (220) plane also appeared. It is known that the TiN-NbN system is miscible and the compound (Ti, Nb)N is a stable pseudo-binary alloy [101]. The NbN film, formed at x=1, did not crystallize, as can be observed from the GI-XRD pattern shown as f igure 5.3 (f). The reasons for the non-crystallization of NbN are not clear. It may be speculated that the experimental conditions did not favour crystallization in the NbN films.
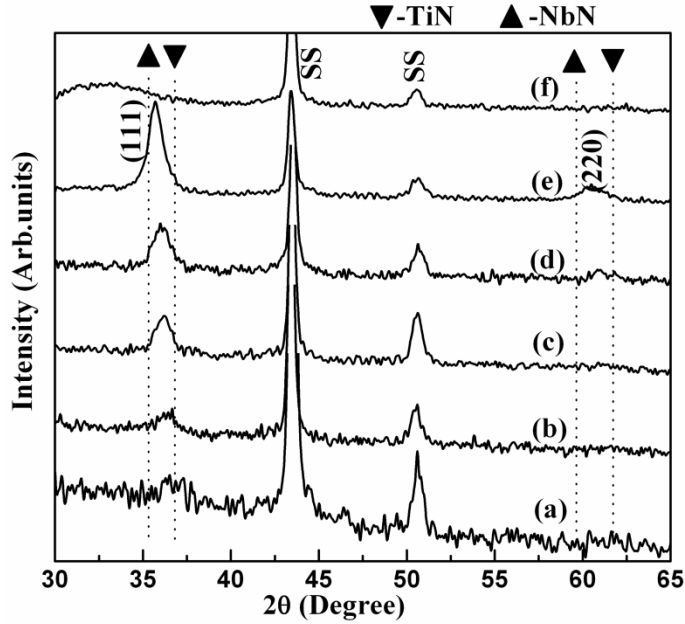
Figure 5.3 Grazing incident-x ray diffraction pattern of $Ti_{1-x}Nb_xN$ films with various Nb substitution (a) x = 0, (b) x = 0.26 (c) x = 0.41 (d) x = 0.58, (e) x = 0.77 and (f) x = 1

Crystal structure of the films also determined using transmission electron microscopy of selected area electron diffraction (SAED) technique. Figure 5.4 shows the TEM-SAED pattern of $Ti_{1-x}Nb_xN$ films for different level of Nb concentration. Structural analysis using TEM-SAED is in good agreement with the GI-XRD analysis, that the $Ti_{1-x}Nb_xN$ films crystallized in to cubic structure up to x=0.77 and NbN film for x=1 is amorphous. In addition to (111) plane, the reflections from (200) and (220) plane also appeared in TEM-SAED pattern. The absence of (200) and (220) planes in the GI-XRD pattern is due to the (111) plane overlap of the position of the SS substrate with the (200) plane position of $Ti_{1-x}Nb_xN$ films and the lower intensity of (220) plane.

Therefore, the intensity of (111) plane of SS dominates over the intensity of (200) plane of $Ti_{1-x}Nb_xN$ films. However, from the structural analysis of $Ti_{1-x}Nb_xN$ films, it is evident that the solid solution was stabilized in the rock salt structure up to $x=0.77$.
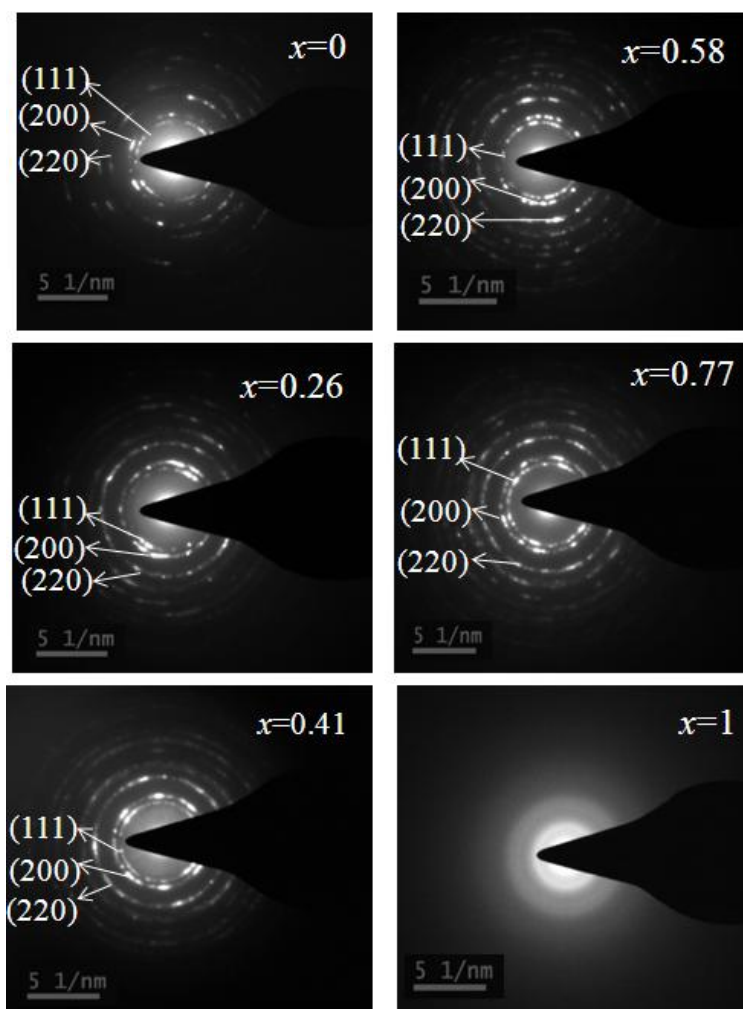

Figure 5.4 Transmission electron microscopy of selected area electron diffraction patterns of $Ti_{1-x}Nb_xN$ thin films for different values of Nb concentration.

The lattice parameter of the films was calculated from GI-XRD and SAED analysis and the value increased from 0.425 to 0.436 nm as the x value increased from 0 to 0.77. The calculated lattice parameter of the films in the cubic structure up to $x=0.77$ was compared with the expected value from Vegard's rule, which relates the lattice parameter to the composition of the ternary system.

For the ternary system, $Ti_{1-x}Nb_xN$, it is expressed as

$$a_{Ti_{1-x}Nb_xN} = (1-x)a_{TiN} + xa_{NbN} \qquad (1)$$

Here a_{NbN} and a_{TiN} are the bulk values of the lattice parameters of NbN (0.4393 nm) [179] and TiN (0.4240 nm) [163] respectively. Figure 5.5 shows the experimental variation of lattice parameter with the composition. This variation is linear, as predicted by Vegard's rule. However, in all the cases the calculated lattice parameter is larger than that predicted by Vegard's rule. This variation may be attributed to the presence of in-plane compressive stress [79].
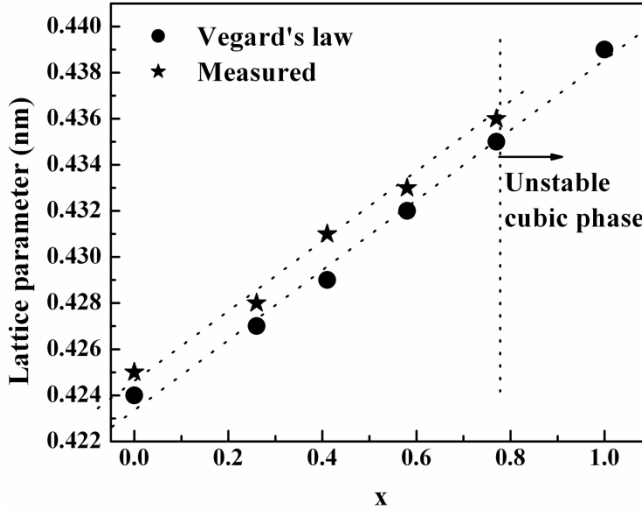

Figure 5.5. Evolution of lattice parameter, along with the prediction based on Vegard's rule.

The crystallite size in the films was calculated by a line profile analysis of the peak broadening. The crystallite size D was estimated using the Scherrer equation

$$D = \frac{0.9\lambda}{\beta \cos\theta} \qquad (2)$$

Here λ is the x-ray wavelength (Cu-K$_\alpha$ radiation, λ=0.15405 nm), β is full width at half-maximum of the XRD peak and θ is the Bragg diffraction angle. Analyses of lattice parameter and crystallite size along with composition analysis are summarized in Table 5.1. The crystallite size varied marginally with composition from 15±2 to 18±2 nm, as x increased from 0 to 0.77. This indicates that Nb substitution does not affect the crystallite size in the films significantly.

Table 5.1 Summary of structural analysis of Ti$_{1-x}$Nb$_x$N thin films

Composition (x)	Metal ratio (Nb/Nb+Ti)	Cubic Ti$_{1-x}$Nb$_x$N thin films	
		Lattice parameter (nm)	Crystallite size (nm)
0.00	0.00	0.425	15.00
0.26	0.29	0.428	16.00
0.41	0.43	0.431	17.00
0.58	0.60	0.433	17.00
0.77	0.77	0.436	18.00
1.00	1.00	-	-

5.5 Nanomechanical and nanotribological properties

Nanomechanical properties such as hardness and Young's modulus of $Ti_{1-x}Nb_xN$ films were determined using load-displacement curve obtained from nanoindentation technique and nanotribological properties such as friction coefficient and wear volume were determined using scratch and wear test respectively.
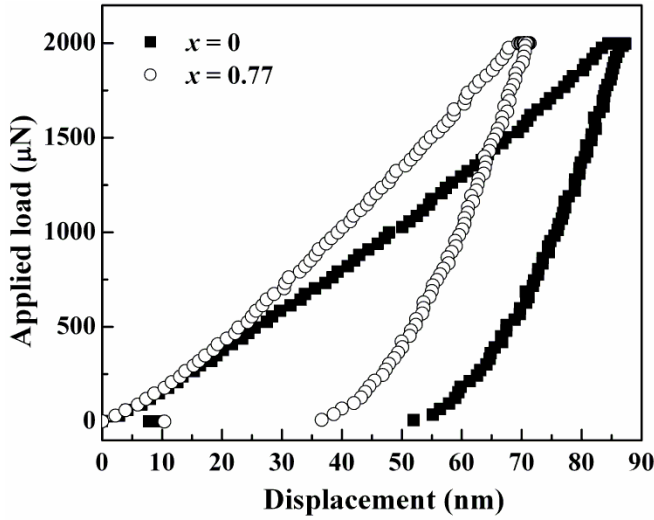

Figure 5.6 Load-displacement curves of $Ti_{1-x}Nb_xN$ thin films for $x=0$ and $x=0.77$.

Hardness and Young's modulus are calculated from load-displacement curves using the Oliver and Pharr method [150] as described in chapter 4. Figure 5.6 shows the typical load-displacement curves obtained from nanoindentation test for x=1 and 0.77 respectively. Clearly the pure TiN film is not as hard as the $Ti_{1-x}Nb_xN$ film with $x=0.77$.

The values of hardness and Young's modulus of the $Ti_{1-x}Nb_xN$ thin films with increasing concentrations of Nb in TiN are displayed in

figure 5.7. The data reveals that the hardness and Young's modulus increase with increasing Nb concentration. Hardness of the TiN film, for x=0, is 17±1.5 GPa which increased to 21±1.8 GPa for x=0.41, 25±2.4 GPa for x=0.58 and then to 31±2.8 GPa for x=0.77. For x=1, the hardness decreases to 20±1.9 GPa for the amorphous NbN film. Similar behavior is observed in the variation of Young's modulus with the Nb content. It increased from 275±8 to 320±13 GPa as x increased from 0 to 0.77 (with rapid increment after x=0.5) and then reduced to 290±11 GPa for x=1 corresponding to the amorphous NbN film. This finding is in line with the well-known relation that hardness scales as Young's modulus. From the figure, it is revealed that x = 0.5 is a threshold value, below which $i.e.$ x < 0.5, both hardness and Young's modulus makes less contribution to the increment and above which $i.e.$ x > 0.5 those are increased rapidly.
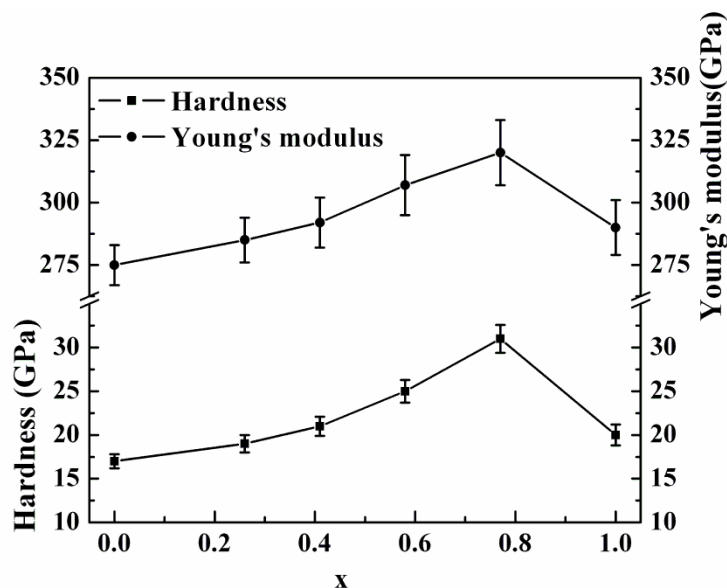

Figure 5.7 Variation of hardness and Young's modulus of $Ti_{1-x}Nb_xN$ thin films as a function x

A review of literature shows that there is a large scatter in the hardness data reported by other workers. Boelens *et al.* [180] deposited Ti-rich (Ti,Nb)N by arc deposition and reported a Vickers hardness value of ~2900 HVN for the $Ti_{0.92}Nb_{0.08}N$ composition. Similarly, Vancoille *et al.*[181] have reported that steered arc ion plated films of composition $Ti_{0.85}Nb_{0.15}N$ exhibit Young's modulus of 375 GPa and Vickers hardness of 2818 HVN units. Grimberg *et al.* reported variation in hardness from 47.7 to 31.5 GPa with a decrease in the nitrogen pressure in TiNbN films deposited by vacuum arc deposition. The composition of the films over this range of pressure changed from 30 at% Ti and 19 at% to 24 at% each of Ti and Nb, i.e from Ti-rich to equal concentrations of Ti and Nb [82]. Ljungcrantz *et al.* [83] reported a study on TiN/NbN multilayers in which a Nb-rich composition of (Ti,Nb)N with 40 at% of Nb was also studied. The films were deposited by reactive magnetron sputtering and displayed a hardness value of 24.7 GPa. The pure TiN film showed a slightly higher hardness value of 26 GPa. Clearly there is large scatter in the hardness data reported in the literature for (Ti,Nb)N films.

Levy and co-workers have studied extensively the electronic and band structures of ternary chromium nitride ($Cr_{1-x}Me_xN$, Me is being substituted metal) and titanium nitrides ($Ti_{1-x}V_xN$ films) [84, 87]. These authors state that the main effect of replacing Ti by V in the metallic sublattice is to raise the intensity of the energy distribution curve at the Fermi level. Based on XPS data they observe that there is negligible shift in the V $2p$ and Ti $2p$ nor the N $1s$ core levels with increase in V concentration for $0.15 < x < 0.5$. It is concluded that changes of the hybridized N $2p$–Me $3d$ and N $2s$ levels observed on the XPS valence-band spectra, as well as the relatively high BE values of N $1s$ core level,

indicate that there are significant changes in the chemical bonding and in charge transfer. In this study although there is no correlation made by the authors with any physical behavior, it is clear that the nature of bonding and charge transfer are strongly dependent on the substituting metal concentration, *i.e.* V. However in the case of ternary chromium nitrides (CrTiN and CrMoN) these authors have found a direct correlation between the change in the nature of bonding and the hardness. The XPS data presented by these authors showed that the peak separations (DBE) between the N2s and the metallic Cr3d/Ti3d states in the valence band and between the N1s and the Cr2p3/2 core levels and the hardness curves show similar minima for x ~0.4-0.5. It is inferred that the decrease of the hardness values for the CrTiN compound at about x=0.4 is caused by the less covalent character of the average bonding. Similar behavior has been reported in TiCrN films by Vishyanakov *et al.* [86].

Several detailed first-principles calculations of the electronic and band structure of transition metal nitrides revealed that the high hardness in the TMN is due to a favourable occupancy of the hybridized Ti 3d (e_g) and N2p states leading to the covalent character. The bonding–antibonding valence band distribution of the N2p–Md (where M is the transition metal) develops symmetrically below and above the hybridization gap. The trigonal prismatic coordination is emphasized through the strong p-d orbital mixing. In TiN, the additional valence electrons contributed by nitrogen fill the antibonding Ti 3d(e_g) and 2p hybridized states at the zone center. Interestingly, the extra nitrogen electrons also populate some of the Ti 3d (t_{2g}) states that build bonds between the Ti atoms. The binding energy of the nitrogen valence and core states decreases, whereas the binding energy of the cation states

increases. The difference in the binding energies between corresponding anion-and cation like states can be considered as a measure of the charge transfer and of the ionic/covalent character of the compound. Jhi *et al.* [45] suggested that the high hardness of this system is due to the fact that the bonding states between the nonmetal p and the metal d orbitals strongly resist shearing strain.

The elastic recovery, R, defined as the period of slight rebound in a material after a load is removed, is estimated from the load-displacement curve. If h_f is the plastic component of displacement and h_{max} is its maximum value, then (h_{max}-h_f) is displacement due to the elastic deformation. The elastic recovery R, is calculated from the relation [182].

$$R(\%) = 100 \times (h_{max} - h_f) / h_{max} \qquad (3)$$

The elastic recovery of $Ti_{1-x}Nb_xN$ films as a function x is depicted in figure 5.8. From the figure it is observed that the film with the highest hardness ($x=0.77$) 31GPa exhibits improved elastic recovery of about 60%.
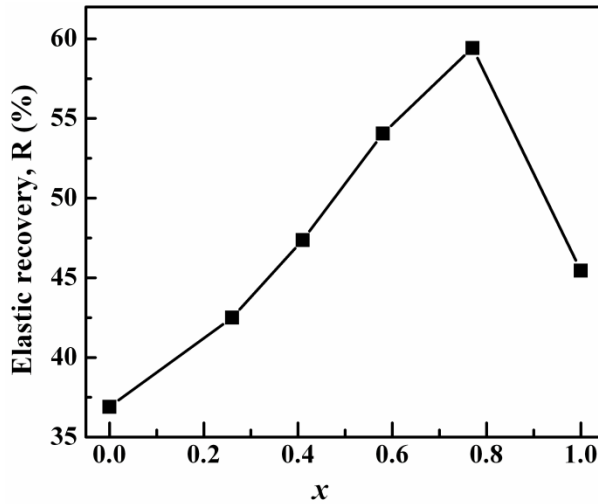

Figure 5.8 Elastic recovery of $Ti_{1-x}Nb_xN$ thin films as a function x.

The coefficient of friction (μ) is defined as the ratio of lateral force to normal force applied to the indenter and the value is measured from scratch test. In the scratch test different segments (5) were used to apply both lateral and normal loads. Ramping force is increased from 0 to 5000 μN to get 10 μm scratch length. Using *in-situ* atomic force microscopy, the scratch length was imaged over a 10 μm×10 μm area. Figure 5.9 shows the AFM image of scratch of $Ti_{1-x}Nb_xN$ thin films for x = 0 and x=0.77 respectively.
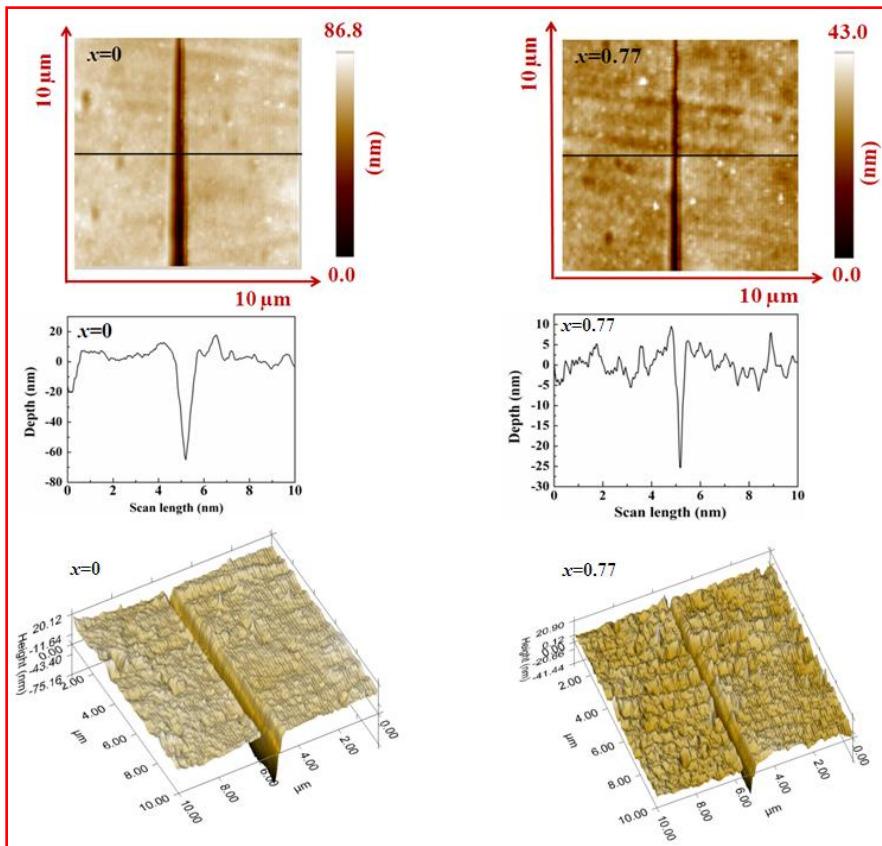
Figure 5.9 2D (top) and 3D (down) AFM images of scratch length of $Ti_{1-x}Nb_xN$ thin films for x=0 (left panel) and x=0.77 (right panel). Line profile of scratch is shown in middle.

Figure 5.10 shows the variation of coefficient friction of $Ti_{1-x}Nb_xN$ films, $0 \leq x \leq 1$, as a function of normal load applied to the tip. From the figure, it is observed that for all films in the entire x range, the friction coefficient slightly increased with increasing normal load. This could be attributed to plastic deformation (more intimate contact) at higher normal loads [183]. The friction coefficient of TiN film for $x=0$ is 0.35 and the value decreases to 0.15 for $x=0.77$ of $Ti_{1-x}Nb_xN$ film. The corresponding value was 0.22 for the NbN film. Low coefficient of friction, in the absence of extra lubrication, indicates that the film has improved scratch resistance. From the scratch test analysis for $Ti_{1-x}Nb_xN$ thin films, it is observed that the scratch resistance increased with an increase in Nb substitution up to $x=0.77$.

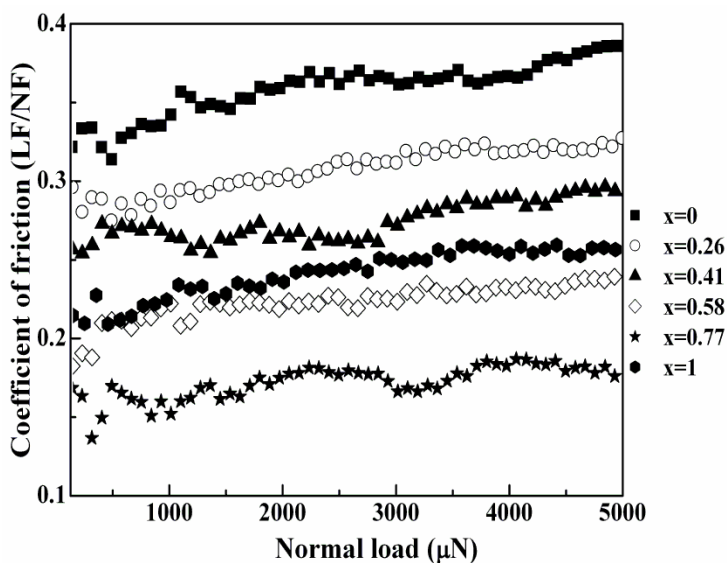Figure 5.10 Variation of coefficient of friction in thin $Ti_{1-x}Nb_xN$ films as a function of normal load

Wear test was performed on deposited films at a contact force of 80 μN over 2 μm × 2 μm area. This area was repeatedly scanned for 20 passes (times). *In-situ* atomic force microscopy was employed to visualize the wear behavior. Figure 5.11 shows the atomic force microscopic images of wear area of $Ti_{1-x}Nb_xN$ thin films. A horizontal line was drawn across the images to measure the depth of wear. The line profiles of the corresponding AFM images are also shown in figure 5.11. From the figure, the depth of wear is seen to be higher for $x=0$ than for $x=0.77$.
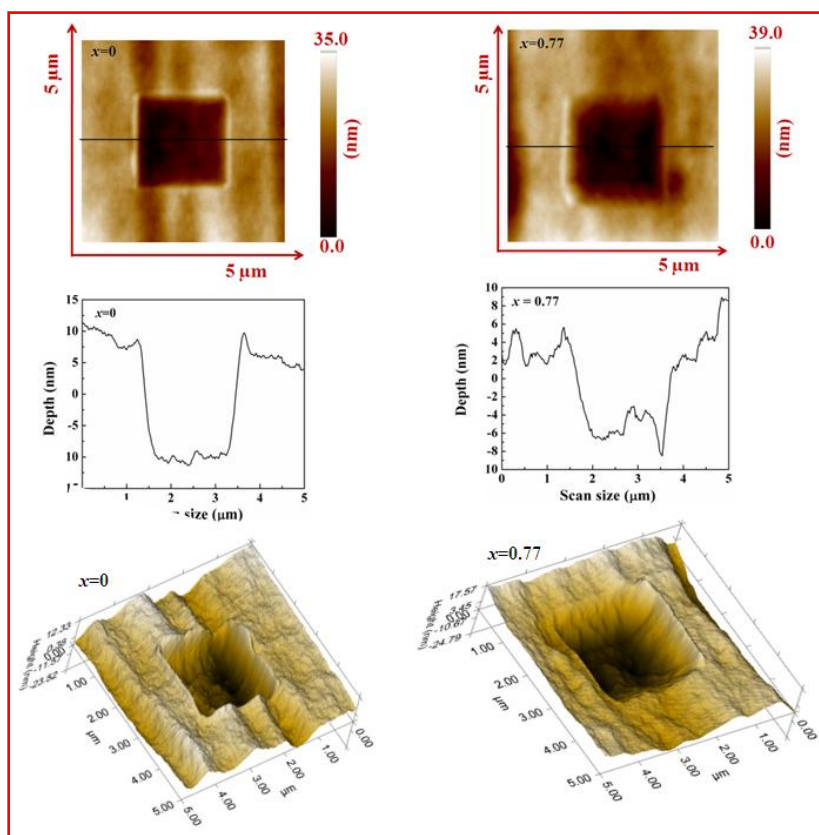

Figure 5.11 2D (top) and 3D (down) AFM images of wear area of $Ti_{1-x}Nb_xN$ thin films for x=0 (left panel) and x=0.77 (right panel). Line profile of wear depth is shown in middle.

The wear test was analyzed in terms of the depth of wear and wear volume. Once the depth of wear is found from the AFM images, the wear volume can be calculated from the relation

$$\text{Wear volume} = (\text{scan size})^2 \times (\text{wear depth})$$

The variation of wear volume with Nb concentration is plotted in figure 5.12. From the figure, it is clear that the wear volume decreased with an increase in Nb concentration. Wear volume of TiN film for x=0 is 0.08 μm^3 which decreased to 0.04 μm^3 for $Ti_{1-x}Nb_xN$ for x=0.77. This value then increased to 0.054 μm^3 for $x=1$ corresponding to the amorphous NbN film. The decrease in wear volume indicates improvement in wear resistance [184]. As the crystal structure of $Ti_{1-x}Nb_xN$ films remains unaltered, it is concluded based on the wear tests that the wear resistance is improved due to increase in Nb concentration
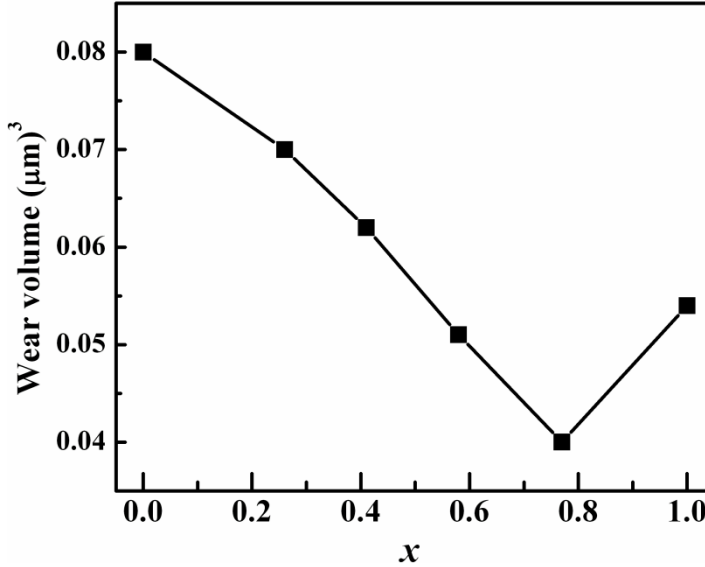

Figure 5.12 Evolution of wear volume of $Ti_{1-x}Nb_xN$ thin films as a function x

5.6 Optical and electronic properties

Optical and electronic properties of $Ti_{1-x}Nb_xN$ film were analyzed by means of their specular reflectance spectra and complex dielectric function calculated based on Drude-Lorentz model. It is demonstrated that the optical and electronic properties studied are dependent on the Nb concentration x and exhibit a threshold at $x=0.5$ similar to mechanical properties.
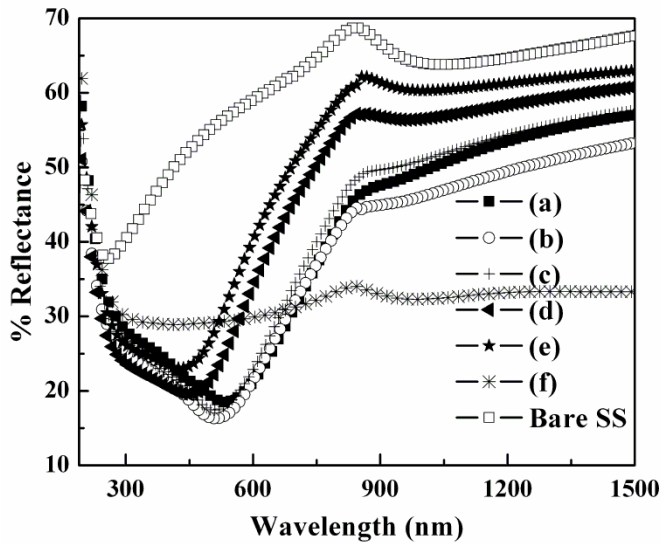

Figure 5.13 Measured specular reflectance spectra of $Ti_{1-x}Nb_xN$ thin films with various Nb concentration, (a): $x=0$, (b): $x=0.26$, (c): $x=0.41$, (d): $x=0.58$, (e): $x=0.77$ and (f): $x=1$.

The measured specular reflectance spectra of deposited films with different levels Nb concentration in the wavelength range 190-1500 nm are shown in figure 5.13. The measured specular reflectance spectra show that the films exhibit a broad reflectance band starting from ultraviolet to the middle of the visible region in all cases (figure 5.13 (a) to (e)) except

for $x=1$ (figure. 5.13 (f)), which corresponds to amorphous NbN film. It is observed that the width of the reflectance band decreases with increasing x. This is accompanied by a shift in position of the reflectance minimum to the shorter wavelength region with an increase in the Nb concentration. The main feature of stoichiometric TiN observed experimentally is centered around 2.33 eV corresponding to charge transfer between the Ti 3p and N 2s states [155]. A similar feature has been observed between the Nb3p and N2s states at ~3.8 eV by various workers [185, 186]. Closer examination of the reflectance spectra revealed that the shift in reflectance minima is negligible for Ti-rich films, *i.e.* for $x < 0.5$, while for Nb-rich films, $x > 0.5$, the shift is more significant. Evidently, as the Nb concentration increases beyond 0.5, the Nb-N charge transfer excitation dominates over the Ti-N charge transfer. The pure NbN film (Figure. 5.13 (f)) displays a slightly different behavior with a very weak reflectance minimum and large reflectance band width. These effects, i.e., width of the reflectance band and shift in position of the reflectance minimum are plotted in figure 5.14 (a) as a function of x. It is evident that the position of the reflectance minimum shifts to shorter wavelengths with increasing Nb concentration and the FWHM of the transition which is a measure of the strength of the charge transfer between the metal p and nitrogen s levels decreases with an increase in Nb concentration. The occurrence of absorption band at different energies with an increase in Nb concentration is due to the variations in valence electron concentration as a result of stoichiometry/compositional variation in the film, which significantly affects the charge transfer mechanism from metal (Ti+Nb) 3p state to N 2s state.
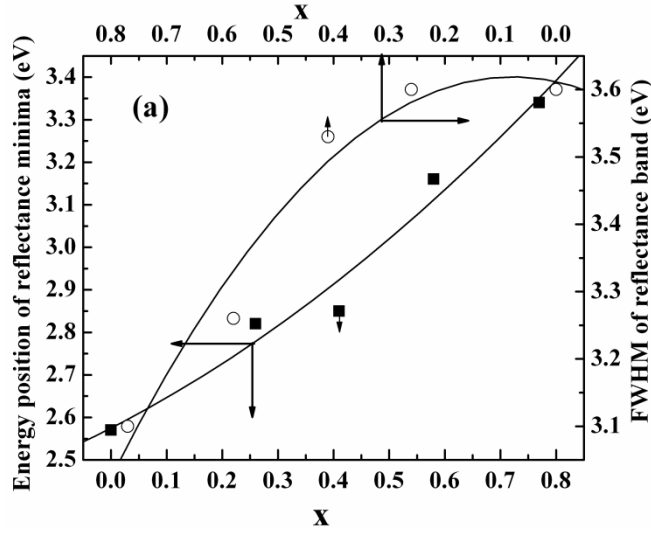
Figure 5.14 (a) Variation in FWHM of the reflectance band and energy position of reflectance minima as a function of x.
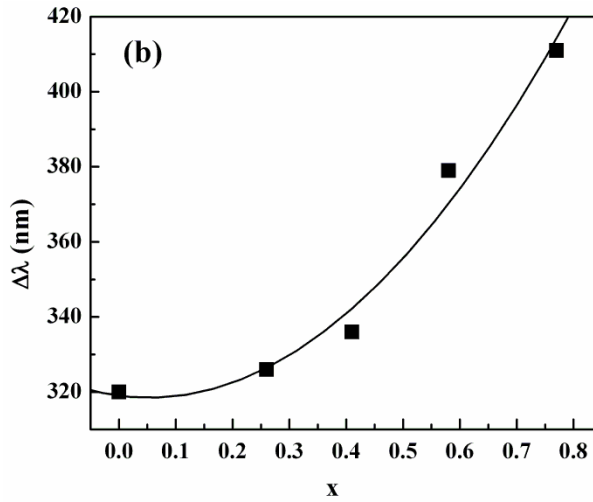

Figure 5.14 (b) The width ($\Delta\lambda$) of the transition from wavelength (λ_{Rmax}) at which highest reflectance occurs to the wavelength (λ_{Rmin}) at which a reflectance minimum occurs, as a function of x

Moreover, Figure 5.13 (a) to 5.13 (e) reveal that the specular reflectance of the films exhibits a sharp increase in reflectance beyond the position of the reflection minimum in the long wavelength region (>750 nm). The sharpness of this transition to high reflectance is characterized by a transition width, $\Delta\lambda$, defined as the difference between the wavelengths beyond which the variation in reflectance is negligible (as indicated in the figure) and the reflectance minimum occurs.

$$\Delta\lambda = \lambda_{R_{max}} - \lambda_{R_{min}} \qquad (4)$$

This is plotted as a function of x in figure 5.14 (b). From the optical reflectance study it is demonstrated that Nb-N charge transfer excitation dominates over the Ti-N charge transfer after a threshold at $x=0.5$. From the figure 5.13, it is observed that in the long wavelength region the percentage of reflectance is increased with increasing Nb concentration. The increase in reflectance is characteristic of Drude-like behavior of these films since they are metallic in nature.

Dielectric function Calculations using the Drude-Lorenz model

In order to calculate the complex dielectric function and optical constants $n(\omega)$ and $k(\omega)$ of $Ti_{1-x}Nb_xN$ films, the interaction of radiation with deposited films was modeled taking into account photon-free electron and photon-bound electron interactions. The model presented here is based on the combined Drude-Lorentz model, in which the Drude term describes the intraband transitions and Lorentz term consists of several oscillators that describe the radiation absorption due to the interband transitions. In this way the contributions to the dielectric

functions due to free electron intraband absorption and those due to bound electron interband transitions could be unambiguously distinguished. The dielectric function based on Drude-Lorentz model can be described using the following equation [5].

$$\varepsilon(\omega) = \varepsilon_\infty - \frac{\omega_{pu}^2}{\omega^2 - i\Gamma_D\omega} + \sum_{j=1}^{4} \frac{f_j.\omega_{0j}^2}{\omega_{0j}^2 - \omega^2 + i\gamma_j\omega} \qquad (5)$$

In the above equation, the contribution of high energy interband transitions is taken into account by introducing the background constant ε_∞, which is real and greater than unity. The Drude term is characterized by a damping factor Γ_D and unscreened plasma energy ω_{pu}. According to free electron theory, the parameter Γ_D is equal to the inverse of relaxation time (τ_D) and is due to electron scattering. Further the parameter ω_{pu} depends on the concentration of conduction electrons in the film and is defined by the relation

$$\omega_{pu} = \sqrt{\frac{Ne^2}{\varepsilon_0 m^*}} \qquad (6)$$

Where N is conduction electron density, e charge of conduction electrons, ε_0 dielectric constant in vacuum and m^* is electron effective mass, in SI units. Since ω_{pu} is directly correlated with the conduction electron density, it can be used to determine the metallic character of $Ti_{1-x}Nb_xN$ films. Each of the Lorentz oscillators is located at an energy position ωo_j, with strength f_j and damping (broadening) factor γ_j.

Normal-incident reflectivity $R(\omega)$ is expressed via the dielectric function $\varepsilon(\omega)$ according to Fresnel formula [187].

$$R(\omega) = \left| \frac{1 - \sqrt{\varepsilon(\omega)}}{1 + \sqrt{\varepsilon(\omega)}} \right|^2 \qquad (7)$$

Based on these equations a complete quantification of dielectric functions of the $Ti_{1-x}Nb_xN$ films was achieved. The initial 'guess' values of the fitted constants (ε_∞, Γ_D, ω_{pu}, ωo_j, f_j and γ_j) were taken from literature for TiN system [28, 29]. They were then refined to fit the spectra of $Ti_{1-x}Nb_xN$ films. Based on (5) and (7) a complete quantification of dielectric functions of the $Ti_{1-x}Nb_xN$ films was achieved.
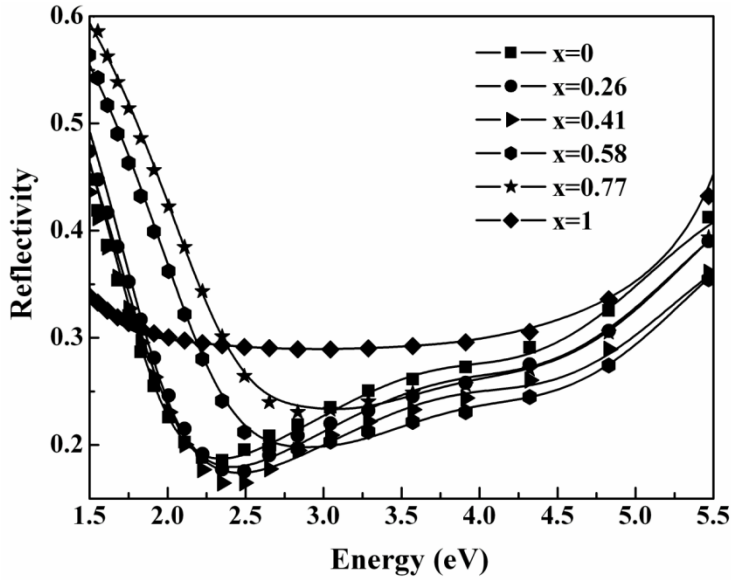

Figure 5.15 Measure reflectance spectra (solid lines) of $Ti_{1-x}Nb_xN$ thin films are fitted with Drude-Lorentz model (symbols).

The measured reflectance spectra of $Ti_{1-x}Nb_xN$ thin films in the spectral range 1.5-5.5 eV are shown in figure 5.15 along with the data fitted using one Drude parameter and four Lorentz oscillators from equations 5 and 7. In the figure, symbols correspond to fitted data using the model and solid lines correspond to experimental data. The Drude parameters ω_{ps}, Γ_D and ε_∞ obtained from the fit are summarized in table 5.2.
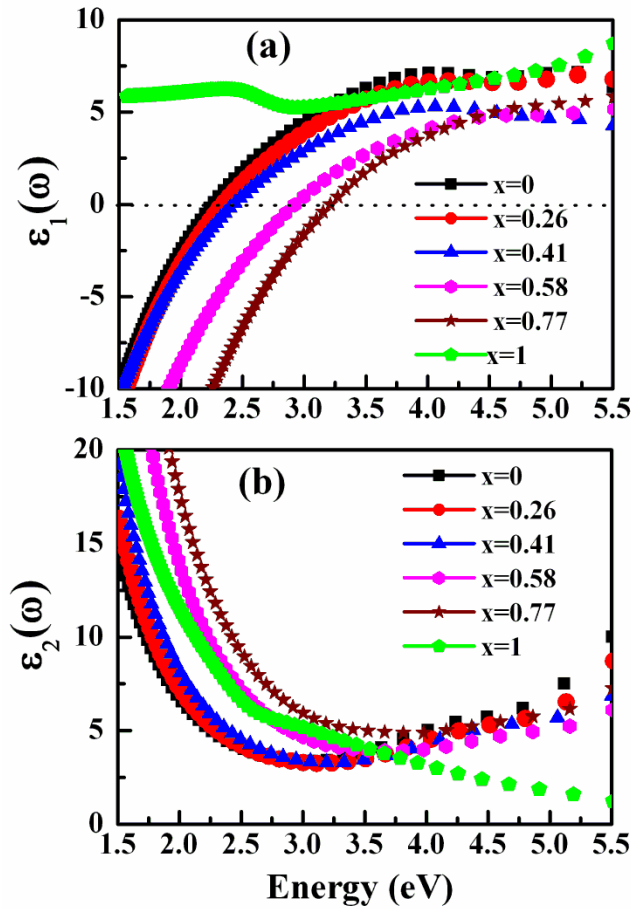

Figure 5.16 (a) Real and (b) imaginary parts of the dielectric function of $Ti_{1-x}Nb_xN$ thin films.

The electronic structure, described based on Drude-Lorentz model via a dielectric function, takes into account both the free and bound electron contributions. The Drude terms describe the optical properties due to free carrier (intraband absorption) response while the Lorentz term is due to the bound electron response. Figure 5.16 shows the real, $\varepsilon_1(\omega)$, and imaginary, $\varepsilon_2(\omega)$, parts of the dielectric function of $Ti_{1-x}Nb_xN$ thin films in the energy range 1.5-5.5 eV. Apart from amorphous NbN, data of all the films showed Drude-like behavior in the IR and visible regions due to the (free-carrier) intraband absorption. The real part of dielectric function of the films passes through zero ($\varepsilon_1(\omega)=0$) in the visible region due to strong interband transitions at the higher energies that indicate the existence of the screened plasma energy, $\omega = \omega_{ps}$ (defined as the energy position at which $\varepsilon_1(\omega)=0$). This energy position has contributions from both free and bound electrons and signals the onset of interband transition in the electronic structure. It can therefore be inferred that strong interband transitions dominate at higher energy. The screened plasma energy of $Ti_{1-x}Nb_xN$ films shifted to higher energies as x is increased. The variation of screened plasma energy with x is depicted in figure 5.17 (a). The value of screened plasma energy of TiN for $x=0$ is 2.25 eV, which is close to the reported value of 2.45 eV [5, 52]. This value increased to 3.22 eV for $x=0.77$, *i.e.* the Nb-rich composition of $Ti_{1-x}Nb_xN$. This value is very close to the reported value of 3.20 eV of NbN film [188]. The dielectric function does not pass through zero for x=1, which indicates that in amorphous NbN the screened plasma energy does not exist. Dielectric function of NbN film exhibits a dielectric behavior rather than metallic in the entire spectral region. There is a consistency in the dielectric function and optical reflectivity study of the films, that the film

with plasma energy exhibits reflectance minima in the reflectance spectra, whereas the dielectric NbN film did not exhibit reflectance minima.
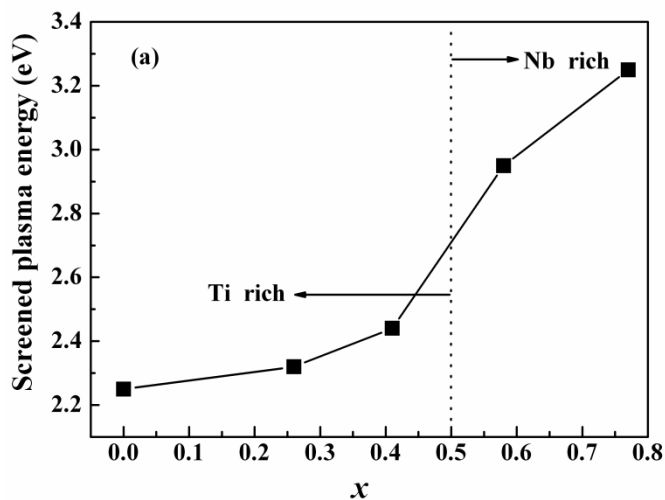

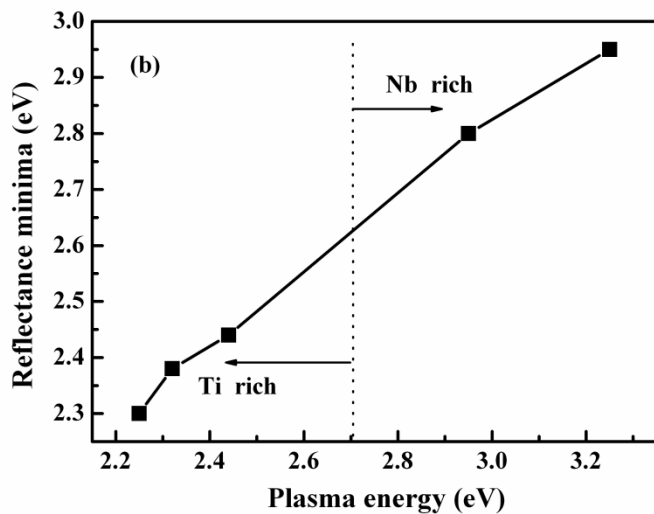Figure 5.17 (a) Variation of screened plasma energy as a function of x

Figure 5.17 (b) Dependence of the reflectance minima on screened plasma energy.

Delin *et al.* [189] reported that the reflectance minimum of transition metal nitrides, like TiN, ZrN, is strongly dependent on the Drude parameter, i.e., screened plasma energy. In the present study also it was observed that the reflectance minimum of the $Ti_{1-x}Nb_xN$ films is strongly dependent on plasma energy, as shown in figure 5.17(b). However, there are two distinct regions of variation depending on Nb concentration. For the Nb deficient films (up to $x = 0.41$), the screened plasma energy values are similar to that of stoichiometric TiN with relatively small variation. Beyond this value of x, there is a large increase in the screened plasma energy signifying a transition to a state characterizing the Nb rich phase.

The dielectric loss-function-spectra ($-im(1/\varepsilon)$) for $Ti_{1-x}Nb_xN$ thin films were calculated using the real and imaginary parts of dielectric function. The dielectric loss-function can be expressed in terms of ε_1 and ε_2 as [187]

$$-im(1/\varepsilon(\omega)) = \varepsilon_2(\omega)/(\varepsilon_1^2(\omega) + \varepsilon_2^2(\omega)) \qquad (8)$$

Figure 5.18 (a) show the dielectric loss-function spectra of $Ti_{1-x}Nb_xN$ thin films in the spectral range 1.5-5.5 eV. All spectra (except NbN film for x=1) show a strong plasmon resonance peak at an energy around $\varepsilon_1(\omega) = 0$. The resonance peak shifts towards higher energy with an increase in x. Figure 5.18 (b) shows the variation of resonance peak position and loss value of $Ti_{1-x}Nb_xN$ films as a function of x. The resonance peak for TiN film appeared at 2.40 eV which blue-shifted to 3.40 eV for $x=0.77$. It is evident that the peak value of the loss function increases initially, as Nb concentration increases from $x=0$ to $x=0.41$, and decreases sharply thereafter, for values of $x>0.41$. In other words, Nb-rich films have a

lower peak dielectric loss than the Ti-rich films with the threshold concentration being approximately $x=0.5$. The resonance energy obtained from the maximum of loss-function-spectra is compared with the plasma energy, $\varepsilon_1(\omega) = 0$, of the dielectric function and reported in table 5.2. From equation 6, it is seen that plasma energy is directly related to the conduction electron density (N). Therefore, the increase of screened plasma energy is interpreted as primarily due to the increase in the conduction electron density with increasing Nb substitution.
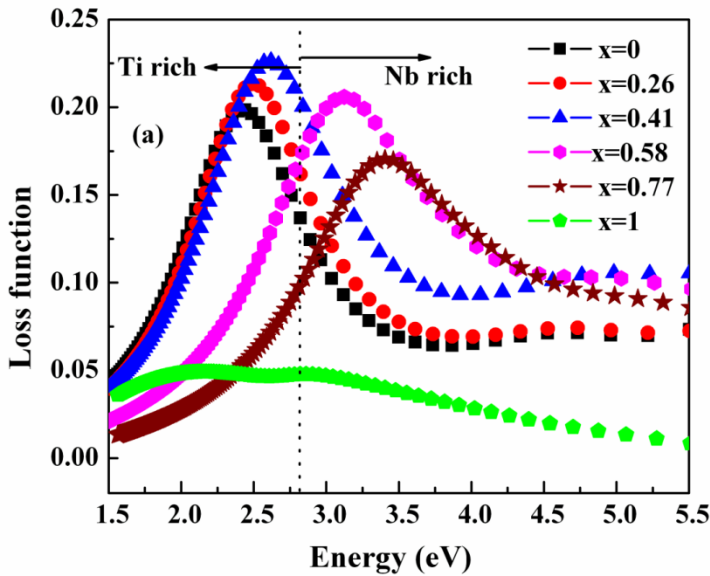

Figure 5.18 (a) Energy-loss-function spectra of $Ti_{1-x}Nb_xN$ thin films.

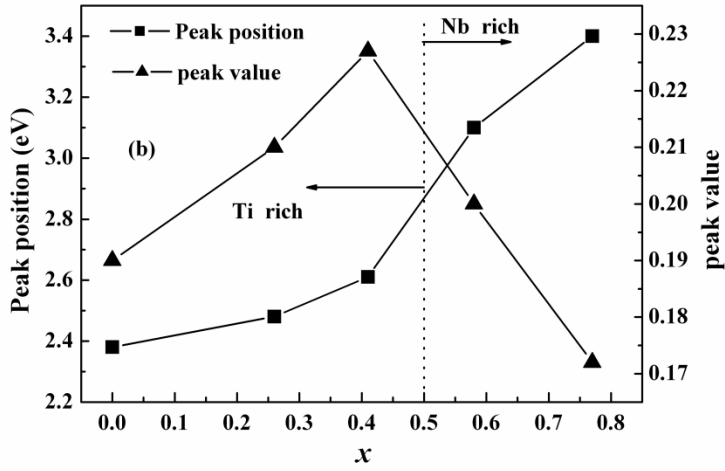Figure 5.18 (b) Variation of plasmon resonance peak position and loss value of $Ti_{1-x}Nb_xN$ films as a function of x.

Table 5.2 Summary of Drude parameters of $Ti_{1-x}Nb_xN$ thin films obtained from the fit of the specular reflectance spectra.

x	ε_∞	Drude parameters		$-im$ (1/ε) (eV)
		Γ_d (eV)	ω_{ps} (eV)	
0.0	4.1	0.95	2.25	2.38
0.26	3.8	0.93	2.34	2.48
0.41	3.0	1.00	2.42	2.61
0.58	3.5	1.20	2.92	3.10
0.77	4.0	1.25	3.22	3.40
1.0	9.5	6.00	-	-

The Lorentz oscillators are included in the fitting procedure to model the onset of the interband transitions. In the present case four Lorentz oscillators have been used to describe the electronic structure of $Ti_{1-x}Nb_xN$ thin films based on the measured reflectance spectra. The

139

Lorentz parameters obtained from the fit are summarized in table 5.3. The oscillators located at ω_{01}, ω_{02}, ω_{03} and ω_{04} correspond to the interband transition between the critical points $\Gamma'_{25} \rightarrow \Gamma_{12}$, $\Gamma_{15} \rightarrow \Gamma_{12}$, $X_5 \rightarrow X_2$ and $L_3 \rightarrow L'_3$ in the Brillouin zone. In the case of TiN film, for $x=0$, four oscillators located at energy positions of 1.0, 2.2, 3.9, 5.45 eV respectively were fitted. These energy positions are in good agreement with the energy positions reported by other authors [5, 52]. Note that the oscillator with a resonant frequency of 1.0 eV had to be introduced to provide for the observed dispersion of the dielectric function. This oscillator is outside the measurement range, but it corresponds, in fact, to the absorption peak (interband transition), predicted in the band structure calculations [5]. Lorentz oscillators of $Ti_{1-x}Nb_xN$ film for $x=0.77$ are located at 1.1, 2.95, 4.1, 5.6 eV respectively; which are slightly increased compared with pure TiN. From table 5.3, it is seen that for all the films the oscillators ω_{01} and ω_{02} are located below the plasma energy in the range of 1.0-1.7 eV and 2.2-2.95 eV respectively. The strength of these oscillators is significantly lower compared with the strength of oscillators at ω_{03} and ω_{04}. High density of conduction electrons below the screened plasma energy blocks the interband transitions so that the strength of the oscillators located below the plasma energy is reduced [62]. In the case of NbN film for x=1, the optical response is modeled using only three Lorentz oscillators and the oscillators are located at 1.7, 3.8, 5.78 eV respectively.

Table 5.3 Summary of Lorentz parameters of $Ti_{1-x}Nb_xN$ thin films obtained from the fit of the specular reflectance spectra.

x	ω_{01} (eV)	ω_{02} (eV)	ω_{03} (eV)	ω_{04} (eV)	f_1	f_2	f_3	f_4	γ_1 (eV)	γ_2 (eV)	γ_3 (eV)	γ_4 (eV)
0.00	1.0	2.20	3.9	5.45	0.1	0.01	1.30	2.92	1.2	1.0	1.8	1.6
0.26	1.0	2.40	4.0	5.60	0.2	0.01	1.30	2.85	1.3	1.0	1.95	1.6
0.41	1.0	2.40	4.0	5.50	0.2	0.01	1.55	2.20	1.3	1.0	2.0	1.75
0.58	1.0	2.90	4.1	5.60	0.1	0.10	1.20	2.20	0.9	1.0	2.1	1.6
0.77	1.1	2.95	4.1	5.60	0.1	0.15	1.35	2.65	0.9	1.0	2.2	1.6
1.00	1.7	-	3.8	5.78	0.6	-	0.10	1.90	0.7	-	1.5	0.25

Since there are no other reports on the values of dielectric functions of $Ti_{1-x}Nb_xN$ films, a comparison with other ternary nitrides has been made. To the first approximation, the values obtained in the present study compare well with those reported for other ternary metal nitrides. The more significant observation is that the optical reflectance and dielectric function can be divided into two distinct regions; Ti rich and Nb rich with a threshold Nb concentration, $x=0.5$. The existence of a threshold concentration has observed in the case of mechanical properties of ternary metal nitrides. To the best of the current authors knowledge, such a threshold for dielectric behavior has not been reported for $Ti_{1-x}Nb_xN$ films.

Dielectric function ($\varepsilon(\omega)=\varepsilon_1(\omega)+i\varepsilon_2(\omega)$) related optical constants, refractive index ($n(\omega)$) and extinction coefficient ($k(\omega)$) can be written in terms of $\varepsilon_1(\omega)$ and $\varepsilon_2(\omega)$ as

$$n(\omega) = \left(\frac{[\varepsilon_1(\omega)^2 + \varepsilon_2(\omega)^2]^{1/2} + \varepsilon_1(\omega)}{2} \right)^{1/2} \qquad (9a)$$

$$k(\omega) = \left(\frac{[\varepsilon_1(\omega)^2 + \varepsilon_2(\omega)^2]^{1/2} - \varepsilon_1(\omega)}{2} \right)^{1/2} \qquad (9b)$$

The refractive index decreases at lower energy and reaches a minimum at about the screened plasma energy (ω_{ps}) and then increases at higher energies. The extinction coefficient, in contrast, decreases at low energy and becomes constant at higher energies. As is known, the extinction coefficient depends mainly on the conductivity of the material through an absorption coefficient $\alpha = 4\pi k/\lambda$. A higher value of k indicates high absorption at lower energy due to free electron density. Figure 5.19 shows the calculated dependence of (a) refractive index, and (b) extinction coefficient of $Ti_{1-x}Nb_xN$ films on photon energy.
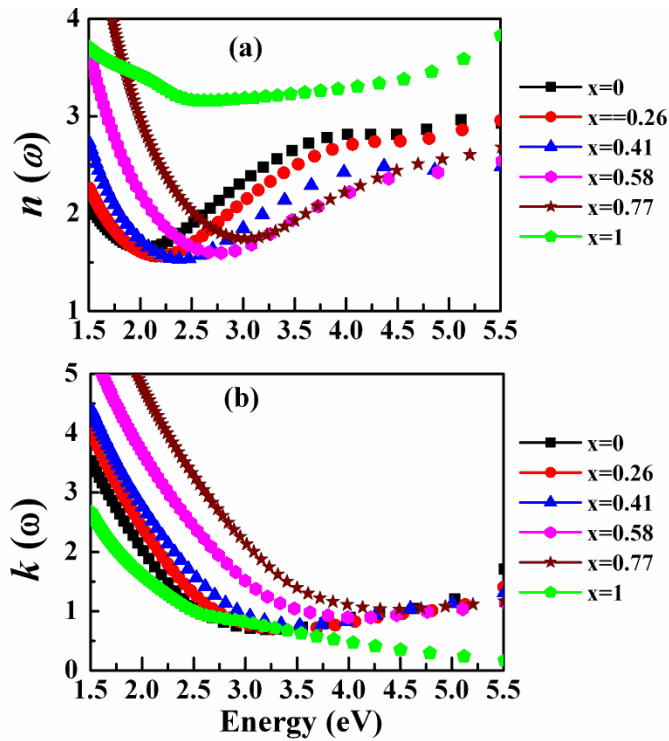
Figure 5.19 Variation of (a) refractive index (b) extinction coefficient of $Ti_{1-x}Nb_xN$ thin films.

5.7. Electrical resistivity

The variation in the metallic nature of the films as a function of x is demonstrated in figure 5.20 by plotting the room temperature resistivity as a function of increasing Nb concentration. The electrical resistivity of TiN film for $x=0$ is 206 ± 10 μΩ-cm which decreases to 56 ± 4 μΩ-cm for $x=0.77$ in $Ti_{1-x}Nb_xN$ film and then increases to 105 ± 6 μΩ-cm for amorphous NbN film at $x=1$. Several studies have established that the electrical conductivity of TiN arises from the intersection of the Ti 3d electrons valence band by the Fermi level and it is strongly dependent on stoichiometric variations [5, 190]. The increase in resistivity in NbN film at $x=1$ is attributed to the lack of long range order.

The bonding of these materials has a covalent character due to the strong hybridization between the N and the metal states and the ionic component is also significant as a consequence of the charge transfer from the metal to the more electronegative nitrogen atom, leading to the metallic nature. In ternary compounds such as (Ti, Nb)N, the increase of the charge transfer from cation states to nitrogen increases the ionic character of the bonding. This is manifested as a decrease in the resistivity of the ternary compound with an increase in x, as seen in the present case.
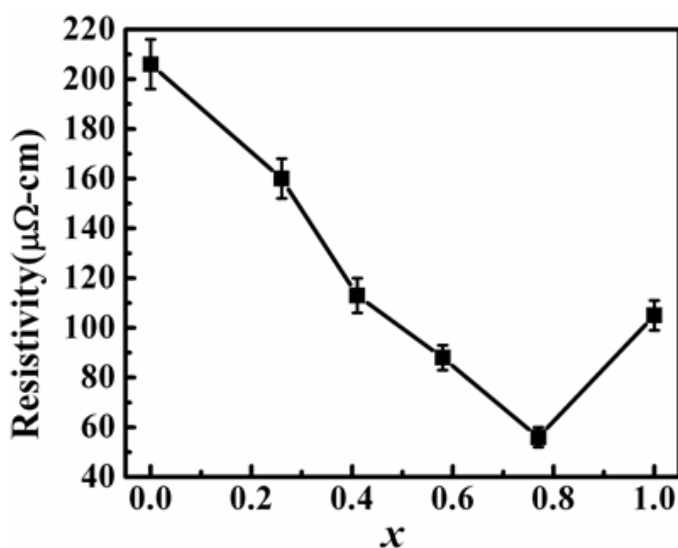
Figure 5.20 Evolution of room temperature electrical resistivity of $Ti_{1-x}Nb_xN$ thin films as a function of x.

5.8 Vibrational properties

Previous studies of Raman scattering of TiN thin films have reported that low frequency scattering below 370 cm^{-1} is caused by acoustical phonons and the high frequency scattering above 500 cm^{-1} is due to optical phonons [32]. The scattering intensities in the acoustical branch are largely determined by the vibrations of the heavy Ti ions, while the scattering in the optical branch is mainly due to the lighter N ions [55]. The first-order Raman scattering of a perfect TiN with a NaCl crystal structure is forbidden, because every ion is at a site of inversion symmetry. However, TiN with defects or substitutional impurities, breaks the crystal symmetry and defect (impurity)-induced first-order Raman

scattering can be observed. Raman spectra of $Ti_{1-x}Nb_xN$ thin films with various levels of Nb substitution over a frequency range of 100-1200 cm^{-1} are presented in figure 5.21. Interestingly, it is observed that the pure TiN film ($x=0$) indeed exhibits Raman scattering with a two-phonon acoustic peak at 620 cm^{-1}, a single-phonon acoustical peak at 270cm^{-1} and an optical phonon peak at 540 cm^{-1}. In addition, there is a low intensity at the lower edge of acoustical phonon peak at 270 cm^{-1}. The intensities of single-phonon acoustic (270 cm^{-1}) and optical (530 cm^{-1}) peaks are relatively low compared with that of two-phonon acoustical peak at 620 cm^{-1}. The one-phonon first-order Raman scattering is forbidden in a perfect NaCl structured TiN. The low intensity and the large width of this peak indicate the good crystalline quality and low cation or anion vacancy density. In our case, TiN peak positions are different from previously reported works [32, 191, 192]. In contrast to the data reported earlier [32, 193] the second-order Raman scattering peak in the frequency range 850-1150 cm^{-1} could not be observed. Those authors reported the occurrence of a peak at 850 cm^{-1} due to an acoustical plus an optical phonon (A+O) and at 1110 cm^{-1} due to two optical phonons (2AO) respectively. The differences between the current and previous reports may be attributed to the differences in the sample preparation conditions and quality.

The Raman spectrum of $Ti_{1-x}Nb_xN$ film for $x=0.26$ exhibits a broad single-phonon acoustical peak at 280 cm^{-1} corresponding to first-order Raman scattering and a two-phonon acoustical peak at 620 cm^{-1}. In comparison with TiN, the peak width for $x=0.26$ was larger although the peak position was the same. The intensity of the single-phonon acoustical peak at 280 cm^{-1} had increased sharply, which

indicates the presence of first-order Raman scattering as Nb is substituted in TiN. The scattering from optical phonon at 540 cm^{-1} is missing probably because of low density of defects. When Nb is added to TiN, the crystal undergoes lattice distortion leading to stress in the film due to the difference in atomic sizes of Nb and Ti which are 146 pm and 140 pm respectively. As a result, Nb substitution breaks the crystal symmetry by lattice distortion leading to the observation of first-order Raman scattering. The observation of acoustical phonon scattering indicates that the vibration of Ti and Nb ions are more pronounced than the N ions. Raman spectra of higher level of Nb substitution of $Ti_{1-x}Nb_xN$ films for x=0.41, 0.58 and 0.77 show that the first-order one-phonon scattering is more pronounced. Raman spectra NbN film for x=1, exhibits first-order Raman scattering because of amorphous nature. But the one-phonon acoustical peak position is shifted to higher frequency side and two-phonon acoustical peak disappeared. This is probably became vibrations of heavy Nb atoms are dominated by lighter N atoms in the randomly arranged crystal structure. The intensity of the one-phonon acoustical peak increase is accompanied by a shift to lower frequency. In contrast, intensity of the two-phonon acoustical peak is constant with a shift to slightly higher frequency. The one-phonon acoustical peak shifts to lower frequency because of variation in lattice parameter of $Ti_{1-x}Nb_xN$ films for various levels of Nb substations.
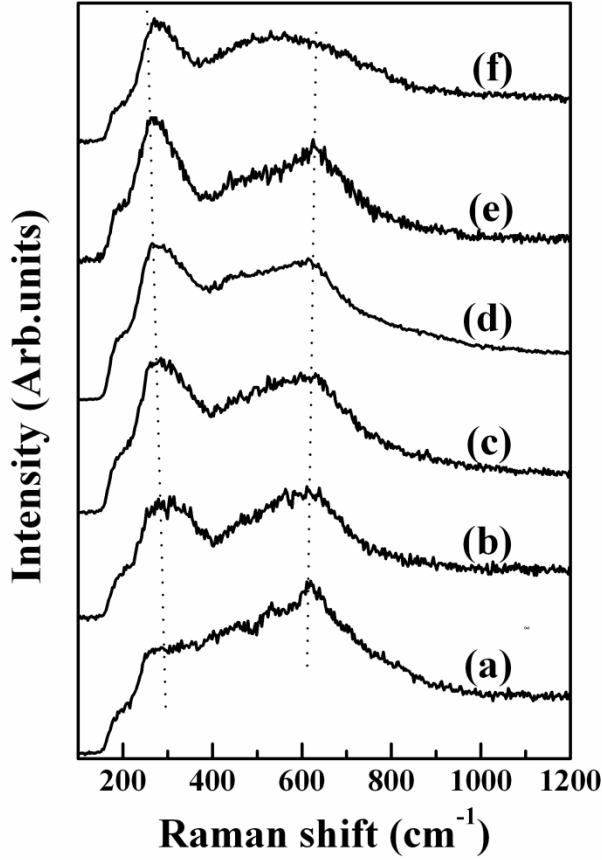
Figure 5.21 Raman spectra of $Ti_{1-x}Nb_xN$ thin films, for (a) $x=0$, (b) x=0.26, (c) x= 0.41, (d) x= 0.58, (e) x=0.77 and (f) x=1.

5.9 Summary

In summary, $Ti_{1-x}Nb_x$ N thin films were coated on 316LN stainless steel by RF reactive magnetron sputtering in 100% N_2 atmosphere at a substrate temperature of 250°C. It is clear from the results presented above that Nb substitution has pronounced influence on the structure,

microstructure, mechanical optical response and dielectric functions of $Ti_{1-x}Nb_xN$ films. The more significant observation is that the mechanical, optical and electronic properties can be divided into two distinct regions ; Ti rich and Nb rich with a threshold Nb concentration, $x=0.5$. From the structural analysis of the films, it is seen that the ternary $Ti_{1-x}Nb_xN$ solid solution was stabilized in the rock salt structure up to $x=0.77$. The ternary nitrides exhibit improved mechanical, tribological, electrical and optical properties in comparison with those of the binaries, TiN and NbN, so long as the structure remained crystalline. The optical reflectance and dielectric functions, in the energy range 1.5-5.5 eV, of $Ti_{1-x}Nb_xN$ thin films were investigated. It is shown that these properties depend critically on the Nb concentration in the films. The screened plasma is close to 2.33 eV for the Ti rich concentrations which increases to 3.2 eV for the Nb rich concentrations. All the films showed evidence for Raman scattering with Nb concentration dependent peak intensities, positions and widths.

It is evident from the above that the observed variation in all the physical properties of $Ti_{1-x}Nb_xN$ films investigated in the present study can be traced to the variations in the electronic/band structure, as a consequence of Nb substitution in TiN. From a practical view, the results demonstrate that $Ti_{1-x}Nb_xN$ coatings enhance the mechanical, optical and electrical properties of the 316LN substrate surface over the entire solid solubility region of x from 0 to 0.77. As previously pointed out, when x = 1, the structure is amorphous and the hardness and electrical conductivity decrease compared to the values found for x= 0.77.

CHAPTER-6

CONDUCTIVE-ATOMIC FORCE MICROSCOPY STUDY ON TiN$_x$ AND Ti$_{1-x}$Nb$_x$N THIN FILMS

Abstract

Simultaneous local current and topography measurements were made on the surface of TiN_x and $Ti_{1-x}Nb_xN$ thin films by conductive-atomic force microscopy (C-AFM). TiN_x (x=0.76, 1) and $Ti_{1-x}Nb_xN$ (0≤x≤0.77) thin films were deposited on borosilicate glass substrate using RF magnetron sputtering. Local variation of current at grain and grain boundaries was examined. Topography images reveal that the films consist of nano grains, for TiN_x films, the grain size is increased from 50 to 73nm as x increased from 0.76 to 1. Similarly, for $Ti_{1-x}Nb_xN$ films the value is increased from 30 to 90 nm as x increased from 0 to 0.77. In both type of films the current distribution on the surface also increased with increase in x for a constant applied voltage of 1V. The measured current is in the order of nA and its flow is filamentary in nature. Current-voltage characteristics of stoichiometric TiN reveal that the grain interiors are electrically conductive, while in sub-stoichiometric $TiN_{0.76}$ thin film, grains are electrically resistive, i.e., a potential barrier to electron transport exists at the junction between the grain and the grain boundary in sub-stoichiometric $TiN_{0.76}$. In $Ti_{1-x}Nb_xN$ films, the grains are electrical conductive and the I-V characteristics clearly show that the local resistance decreased with an increase in grain size. In both type of films, it is observed local resistance is several orders of magnitude larger than the total resistance and the value is of the order of MΩ. Electron-grain boundary scattering and the presence of native oxide states is responsible for increase the local electrical resistance of the films.

6.1 Introduction

Conductive Atomic Force Microscopy (C-AFM) is a mode of atomic force microscopy in which a conductive tip is scanned in contact with the conductive sample surface, while a dc voltage is applied between the tip and the sample, generating a current image. The electrical properties of granular materials such as thin films are strongly dependent on composition, crystallographic phase and microstructure. Microstructural features such as grain size, grain shape, grain boundary, porosity and roughness strongly affect the overall conductivity of the film. In addition, variations in local composition, electronic and electrical properties affect the overall performance and quality of nanostructures materials and devices. Conventional four-point probe method measures only the average value of electrical resistivity of a material at the macroscopic level. In contrast, conductive-atomic force microscopy (C-AFM) is a technique that can probe the local variations in the conductivity of a material (crystal or thin film) with microstructure. C-AFM has been widely used in profiling the local electronic structure and morphology of various surfaces with high spatial resolution. It is also possible to investigate quantitatively electron transport on a nm-scale by this technique [194-198].

In previous chapters IV and V, we have shown that microstructure, composition and physical properties of TiN_x and $Ti_{1-x}Nb_xN$ thin films are strongly dependent on process parameters. In this chapter, we present the C-AFM study of local electrical and electron transport properties of TiN_x and $Ti_{1-x}Nb_xN$ thin films of various compositions. A platinum thin film of thickness 40 nm was used as a standard for the topography and the C-AFM studies. The contribution of

grain interior and grain boundary to the total conductivity is clearly established by examining the current-voltage (I-V) characteristics across the scanned area.

6.2 Experimental condition

Table 6.1 Experimental conditions used to deposit TiN_x and $Ti_{1-x}Nb_xN$ thin films

Experimental parameter	TiN_x	$Ti_{1-x}Nb_xN$
Deposition method	RF magnetron sputtering	RF magnetron sputtering
Target material	2 inch diameter Ti	2 inch diameter Ti (Nb fractions was varied on the Ti surface)
Substrates	Borosilicate glass	Borosilicate glass
Ultimate pressure	3×10^{-6} mbar	3×10^{-6} mbar
Working pressure	5×10^{-2} mbar	5×10^{-2} mbar
Sputtering gas	100 % nitrogen	100 % nitrogen
RF power	100 Watt	100 Watt
IE Distance	60 mm	50 mm
Substrate temperature	200 and 350°C	250°C
Deposition time	120 min	120 min

The thickness of the films was estimated using surface profilometer and the values are 140 ±12 and 120±10 nm for TiN_x films deposited at 350 and 200°C and for $Ti_{1-x}Nb_xN$ films the value is 150±20nm. The composition of the films was determined from EDX spectra. For TiN_x films, deposited at 200 and 350°C, the composition determined as $TiN_{0.76}$ and TiN and for $Ti_{1-x}Nb_xN$ films the composition (x) values are 0, 0.26, 0.58 and 0.77 respectively. The structural properties of TiN_x and $Ti_{1-x}Nb_xN$ films are already been discussed in chapters 4 and 5.

6.3 Four probe measurement

The composition dependent sheet resistance of TiN_x and $Ti_{1-x}Nb_xN$ thin films was measured using the four probe technique at room temperature. The sheet resistance values for TiN and $TiN_{0.76}$ films are 12 kΩ/sq and 425 kΩ/sq respectively. In the case of $Ti_{1-x}Nb_xN$ thin films, the sheet resistance was calculated as a function of x and its variation depicted in figure 6.1. It is observed that the sheet resistance is decreased with increase in x value. The sheet resistance of TiN film for $x=0$ is 87 Ω/sq and this value is decreased to 72 Ω/sq for x=0.26, 27 Ω/sq at $x=0.58$ and finally 14 Ω/sq for $x=0.77$ in $Ti_{1-x}Nb_xN$ film. The detailed study of the composition dependent electrical resistivity of $Ti_{1-x}Nb_xN$ on SS substrate is already discussed in chapter-5. By comparing the sheet resistance values of TiN_x and $Ti_{1-x}Nb_xN$ thin films it is inferred that $Ti_{1-x}Nb_xN$ films are highly conductive than TiN_x films.
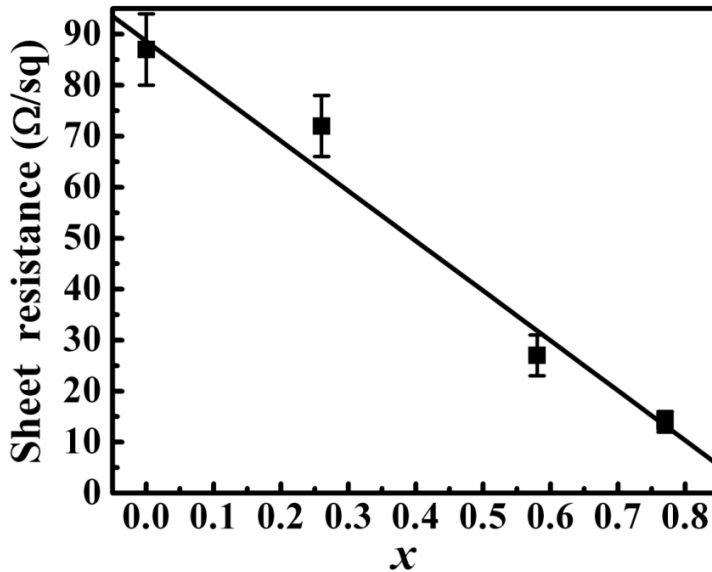

Figure 6.1 Variation of sheet resistance of $Ti_{1-x}Nb_xN$ thin films as a function of x

6.4 C-AFM measurement on the surface of TiN_x and $Ti_{1-x}Nb_xN$ thin films

6.4.1 TiN_x thin films

The 2-D and 3-D topography and current images of Pt, TiN and $TiN_{0.76}$ films are shown in figures 6.2 and 6.3. In both figures the left panel is topography image and the right panel is current image. From 2-D topography image, it is observed that the surface of the Pt film is relatively smoother (the average roughness being 0.84 nm) and less granular than that for the titanium nitride films.
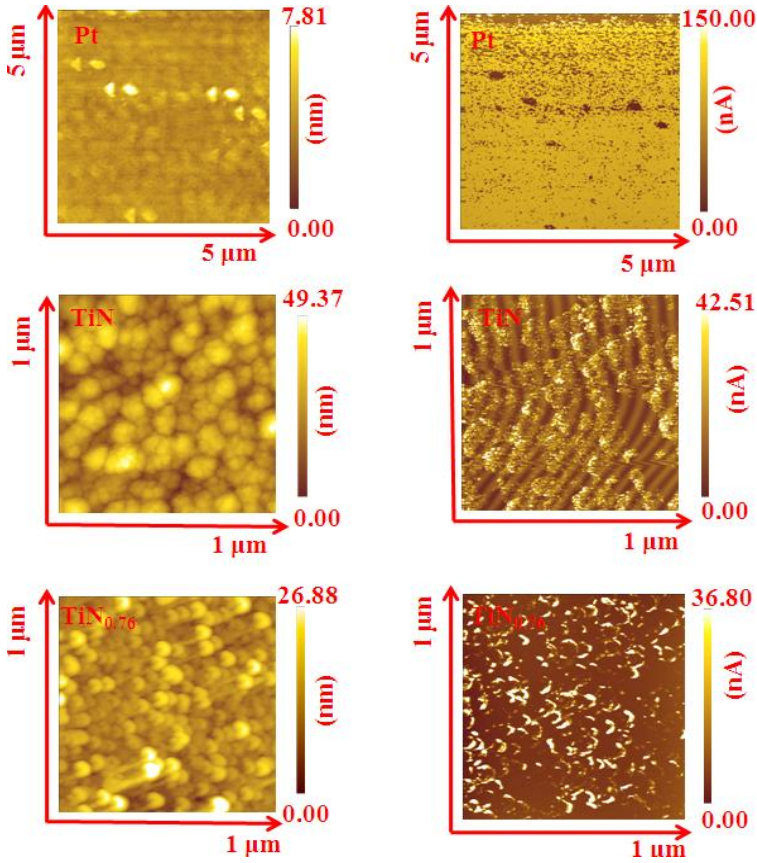

Figure 6.2: 2-D topography (left panel) and current (right panel) images of Pt, TiN and $TiN_{0.76}$ thin films

The titanium nitride films, on the other hand, were granular with some evidence for surface roughness. The grain size in the case of TiN was 73 ± 12 nm with average roughness of 4 ± 1 nm, while the grain size was 50 ± 5 nm for the $TiN_{0.76}$ films with average roughness of 2 ± 0.5 nm. In the 2-D current images bright areas correspond to regions of higher current flow.
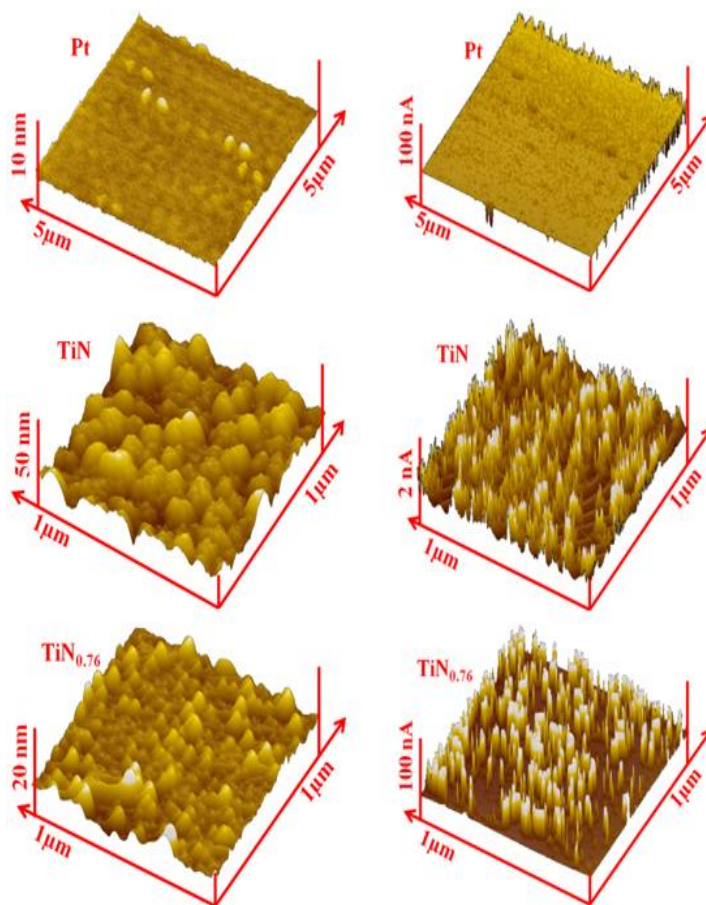

Figure 6.3: 3-D topography (left panel) and current (right panel) images of Pt, TiN and $TiN_{0.76}$ thin films

The current image was registered simultaneously with topography image at a constant voltage of 1 V applied to the sample during scanning. From 3-D current image (figure 6.3 right panel), it is observed that the current distribution across the surface of the Pt films is more uniform than that for the TiN_x films, with the maximum current (Z-axis) of ~75 nA. The mildly filamentary nature of the current distribution (especially at the edges) in this case can be attributed to the slight granularity and roughness of the surface. From the 3-D current images of the TiN and $TiN_{0.76}$ films, it is evident that the current flow across the two films is filamentary in nature, *i.e.* there are regions of high current are separated by regions of very low current. This is in sharp contrast with the current image of the Pt film which showed a uniform distribution of current across the film surface. But there is also a significant difference between the 3-D current images of the $TiN_{0.76}$ film, and that of the TiN film. Although in both the cases the current is filamentary in nature, the density of these filaments is much lower in sub-stoichiometric TiN films. Clearly, there are fewer percolation paths for conduction in $TiN_{0.76}$ than in stoichiometric TiN.

6.4.2 $Ti_{1-x}Nb_xN$ thin films

The C-AFM measurements were carried out on the surface of $Ti_{1-x}Nb_xN$ thin films similar to TiN_x films. The 2D topography images over a $1\,\mu m \times 1\,\mu m$ scan area with the corresponding grain size distribution are shown in figure 6.4. From the figure, it is evidence that the surface of all films consists of spherical grains of slightly varying diameter without voids and rugged structure. The mean grain size (D) calculated from the grain size distributions shown in the same figure

indicate that the mean grain size increased with increase in x value. The mean grain size of TiN film for $x=0$ is 30 nm and the value is increased to 90 nm for $x=0.77$ in the $Ti_{1-x}Nb_xN$ thin film. Surface roughness also follows the same trend as grains size, the value is increased from 0.5 to 3.2 nm as x increase from 0 to 0.77. The grain size and roughness of thin films follow the linear relation; therefore, the grain size is responsible for the increase of roughness of the films [199]. The frequency of grain size is summarized in the form of histograms and all the films show an almost symmetric distribution. Histogram of all film is fitted to Gaussian (normal) distribution and the central tendency of the distribution is around mean grain size of the film.

Figure 6.5 shows the 2D and 3D current image of $Ti_{1-x}Nb_xN$ thin films over a 1 μm ×1 μm scan area. In the 2D and 3D current images, bright the areas correspond to areas of higher conductivity than the darker low conductivity areas. Hence, by comparing the 2D topography and current images, the conducting/insulating paths on the surface of the films can be distinguished. There is significant variation in the 3D current images of $Ti_{1-x}Nb_xN$ film with increasing value of x. From the 3D current images it is observed that the current on the surface increased with increase in grain size. TiN film having grain size of 30 nm shows a maximum current on the surface is 15 nA (Z-axis). The current value increased to 37 nA and then to 85 nA for $Ti_{1-x}Nb_xN$ films with $x=0.26$ and 0.58 having grain sizes of 42 nm and 75 nm respectively. The maximum current of 100 nA was observed for the $Ti_{1-x}Nb_xN$ with x=0.77 and grain size 90 nm. It should be noted that the maximum current may be higher but shows saturation since the current pre-amplifier in our C-AFM system saturates at 100nA. Similar to TiN_x films, current flow in

Ti$_{1-x}$Nb$_x$N films also have filamentary nature. From figure 6.5, it is observed that the grain interiors are conductive than the grain boundary.

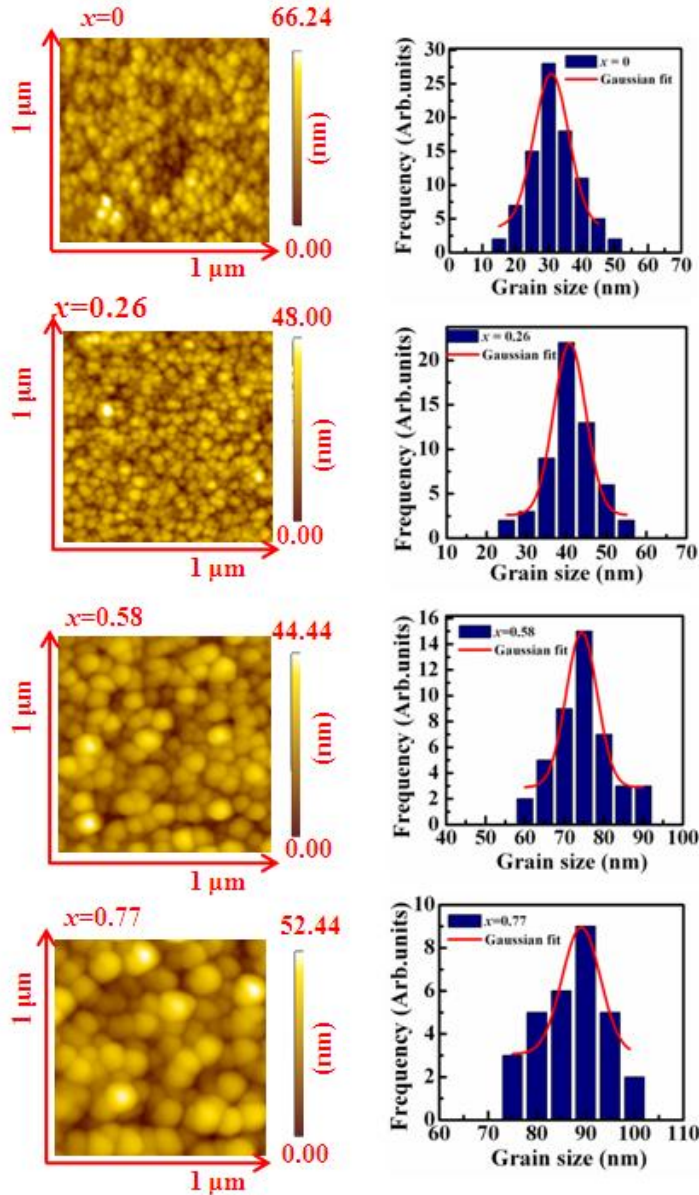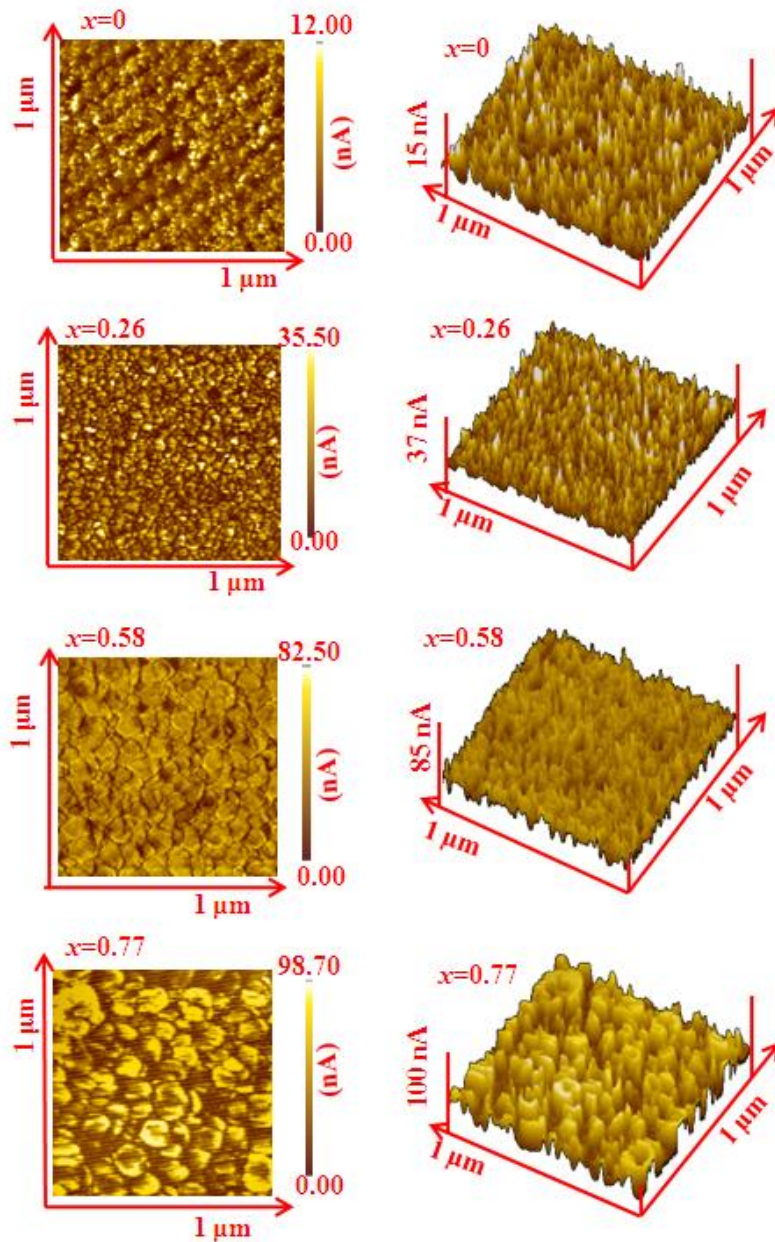Figure 6.4: 2-D topography images of Ti$_{1-x}$Nb$_x$N thin films over 1 μm ×1 μm scan area with corresponding grain size distribution.

Figure 6.5: 2-D (left panel) and 3-D (right panel) current image of $Ti_{1-x}Nb_xN$ thin films

6.5 Local electrical and electron transport properties of TiN_x and $Ti_{1-x}Nb_xN$ films

6.5.1 Local I-V characteristics of TiN_x and $Ti_{1-x}Nb_xN$ films

Local I-V characteristics of TiN_x and $Ti_{1-x}Nb_xN$ films are measured at different locations across the scanned area of each film *in-situ* after imaging. The I-V characteristics of TiN_x films along with platinum film are shown in figure 6.6. The 2-D current images with locations at which the I-V characteristics were measured are also given in these figures as insets. The I-V characteristics of the Pt film indicate that the film is uniformly conducting across the scanned area. This view is supported by the ohmic nature of the I-V plots at all locations considered. In the case of the stoichiometric TiN films, the I-V characteristics reveal that the grain interior and grain boundary conductivity is of the same order of magnitude, but non-ohmic. At a bias of 0.05 V, the current is of the order of 50 nA, leading to a local resistance of the order of 1 MΩ. In addition, the conductivity saturates at higher bias voltages (>0.1 V). For the sub-stoichiometric $TiN_{0.76}$ films the situation is completely different. The current in the grain interiors at a given bias (locations 1, 2, 3 and 4) is much lower than the current in the grain boundaries (locations 5 and 6). There is almost one order of magnitude difference in conductivity. Within the grains (locations 5 and 6) the resistance of the order of 1 MΩ, whereas across the grain boundary the conductivity is diode-like with an energy barrier (i.e., the minimum bias at which conductivity commences) of the order of 0.6 V.
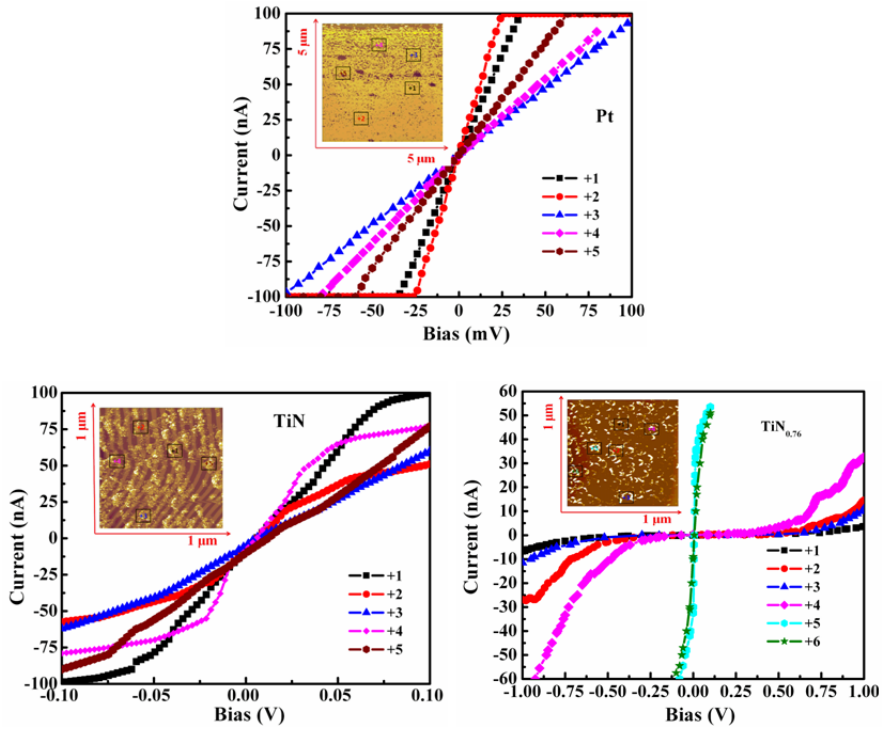
Figure 6.6 I-V characteristics of the Pt, TiN, and TiN$_{0.76}$ films taken at different locations on the current image shown in the insets

Figure 6.7 shows the local I-V characteristics of Ti$_{1-x}$Nb$_x$N films for a sweeping voltage of $\pm$ 100 mV. For TiN film (x=0), the I-V characteristics were measured at high and low conducting areas. Points selected at high conducting area (+1 and +2), I-V curve shows Ohmic behavior while the low conducting area (+3) shows non-linear behavior. The resistance (1/slope) of the curves slightly varied and the magnitude of current on the y-axis was in the range of 5-20 nA at a bias voltage of 100 mV. Since the tip diameter is 35 nm, in this case it may be in contact

with both grain and grain boundary, as the mean grains size (30nm) of the films is less than that of radius of curvature of the tip. Hence, it is not possible to distinguish the grain and grain boundary contribution to the resistance. Therefore, the resistance measured from I-V curves of TiN film is due to both grain and grain boundary contribution. In the case of $Ti_{1-x}Nb_xN$ film (x=0.26), the I-V characteristics of all points selected (+1, +2 and+3) display Ohmic behavior. The magnitude of current on y-axis is around 30 nA at a bias voltage of 100 mV. The grain size of the film is 42 nm, therefore, in this case the tip is partially in contact with grain and grain boundary. Similar variation in I-V characteristics of $Ti_{1-x}Nb_xN$ film for x=0.58 is observed. However, the magnitude of current is different with the current being about 70 nA at a bias voltage of 100 mV. In the case of $Ti_{1-x}Nb_xN$ film with x=0.77, the grain interior and grain boundary contributions can be easily separated since the size is 90 nm. It is seen that the I-V characteristics of all points selected on the grain and grain boundary shows Ohmic behavior. However, the resistance is higher for the point (+2) selected on the grain boundary compared to that of the points (+1 and +3) selected on the grain interior. The magnitude of current is of the order (100 nA) of on the grain interior and is about 70 nA on grain boundary at a bias voltage of 100 mV.
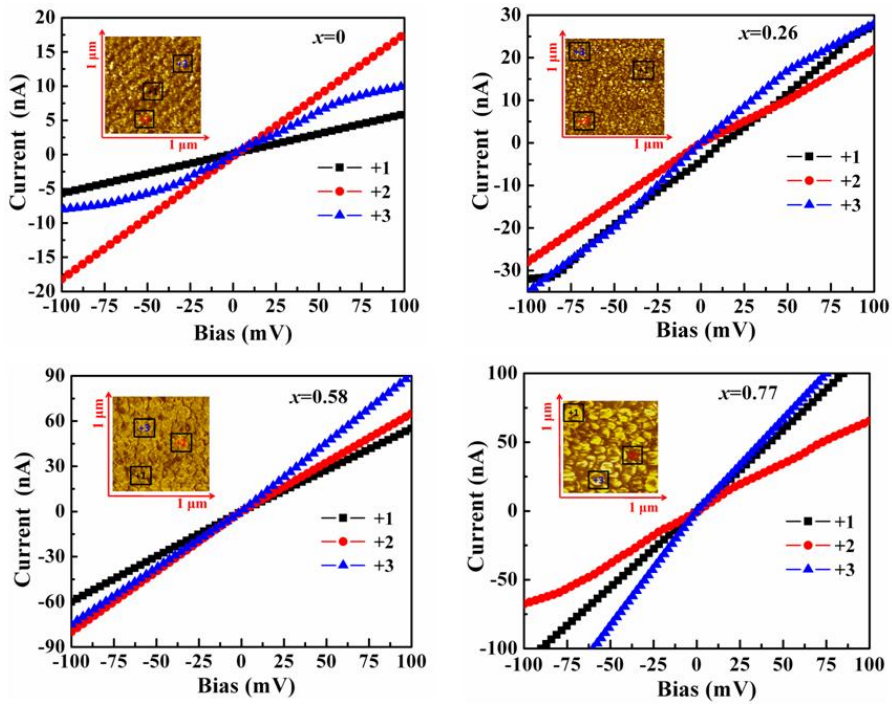
Figure 6.7 Local I-V characteristics of $Ti_{1-x}Nb_xN$ films for a sweeping voltage of ± 100 mV. The 2-D current images with locations at which the I-V characteristics were measured are given in the insets.

6.5.2 Microstructure dependent local resistance

The local resistance of TiN_x and $Ti_{1-x}Nb_xN$ films was calculated from I-V characteristics measured at different locations in each film. The measured local resistance of all films is in the range of MΩ. For $Ti_{1-x}Nb_xN$ films, the local resistance was plotted as a function of mean grains size. Figure 6.8 shows variation of local resistance of $Ti_{1-x}Nb_xN$ film with grain size. It is observed that the local resistance is decreased with an increase in grains size. The local resistance of TiN film for x=0 is 20 MΩ and the value is decrease to 0.05 MΩ for x=077 of $Ti_{1-x}Nb_xN$

163

film. As compared to the figure 6.1, the variation in local resistance is follow the same trend as composition dependent sheet resistance, but strongly dependent on the microstructure.
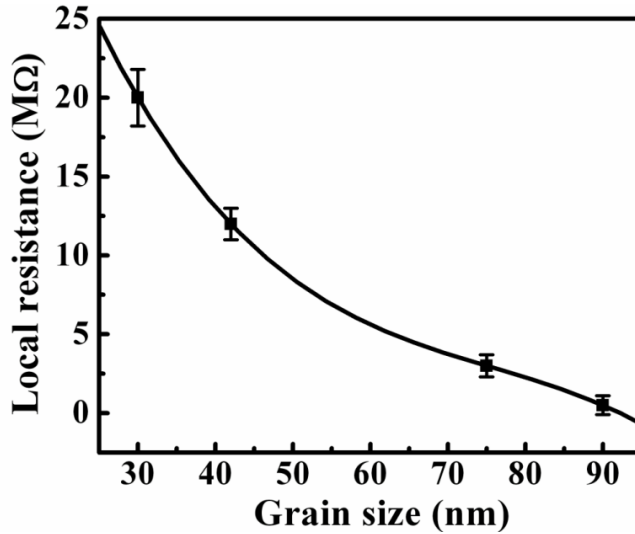

Figure 6.8 Variation in the local resistance of $Ti_{1-x}Nb_xN$ film with grain size.

It is clear from the results presented above that the conductivity in nanostructured TiN_x and $Ti_{1-x}Nb_xN$ films has two major contributors: (1) electronic structure, and (2) microstructure.

6.5.3 Electronic structure

When two materials are electrically connected, electrons flow from the material with the smaller work function to that with the higher work-function. The diffusion current builds a double layer at the interface. This results in a contact potential difference (CPD), $\Delta\Phi$,

between the two materials until the Fermi levels (E_F) for each one are equal. Schematic diagram of variation in Fermi level before and after contact between tip and film is shown in figure 6.9.
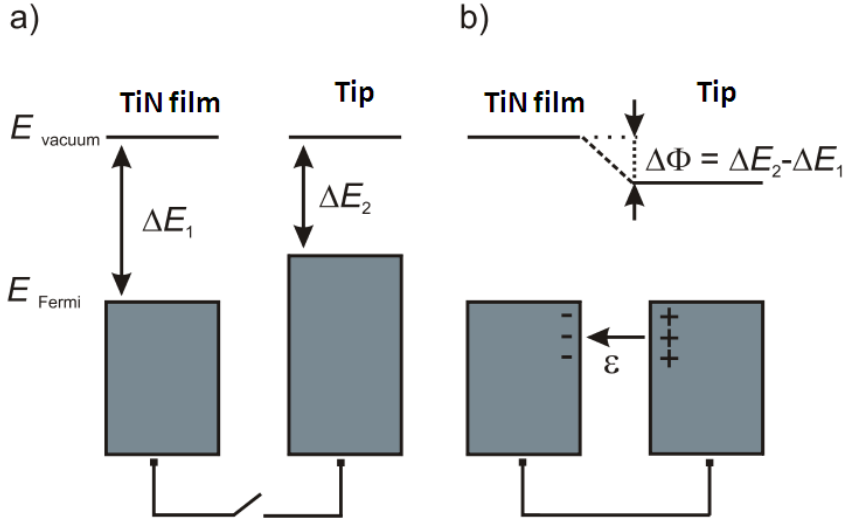
6.9 (a) difference in Fermi level between film and tip before contact (b) equalized Fermi level after contact

Conducting AFM tip and film (TiN_x and $Ti_{1-x}Nb_xN$) with different work-functions are connected, then the CPD is given by [200].

$$\Delta\Phi = \frac{\Phi_{E_2} - \Phi_{E_1}}{e} = \frac{\Phi_{tip} - \Phi_{film}}{e} \qquad (1)$$

The work function of the gold coated tip is ~5.1 eV [201] whereas that for the TiN_x film is ~4.0eV [202]. The CPD is approximately 1 eV and this value is significantly varies for tip and $Ti_{1-x}Nb_xN$ film contact.

The attractive force, *F,* between the tip and the sample takes the form

$$F = \frac{1}{2}(\Delta\Phi)^2 \frac{\partial C}{\partial z} \qquad (2)$$

Where C is the separation-dependent capacitance between the tip and sample and z is the tip-sample distance. The variations in conductivity due to the differences in electronic structure are manifested as changes in the total resistivity as a function of the chemical composition. From eqns (1) and (2) it can be inferred that the local work function can also vary due to local variations in stoichiometry [203-206].

6.5.4 Microstructure

Microstructure dependent variation in electrical resistance can be explained by considering the electron-grain boundary scattering in polycrystalline metallic films based on Mayadas and Shatzkes model. Microscopically there are two main scattering mechanisms that can lead to increase the resistivity of polycrystalline metallic films. The first one is electron-surface scattering described by Fuchs and Sondheimer (F-S) [207, 208]. The second one is electron-grain boundary scattering described by Mayadas and Shatzkes (M-S) [209]. In general, this two scattering mechanisms contributes the resistivity increase, if the films with varying thickness and mean grain size. Both theories are associated with phenomenological parameters with which the resistivity increase can be quantified. The specularity parameter (p) in the first case denotes the degree of elastic scattering at the surface and the grain boundary

reflection coefficient (R) in the second case describes the physical nature of scattering at the grain boundary. It is inferred that the grain boundary scattering is the strongest contribution to the resistance increase. In the M-S model, it is assumed that the every grain boundary as an internal surface. When an electron collides with a grain boundary, it has a probability of transmission or reflection that is quantified by a reflection coefficient, R (0<R<1). The resistivity is dependent on the reflection coefficient for electron transport at the grain boundaries and will therefore increase with an increase in the grain boundary contribution. Figure 6.10 shows the visualization picture of the grains boundary scattering in a polycrystalline thin films.
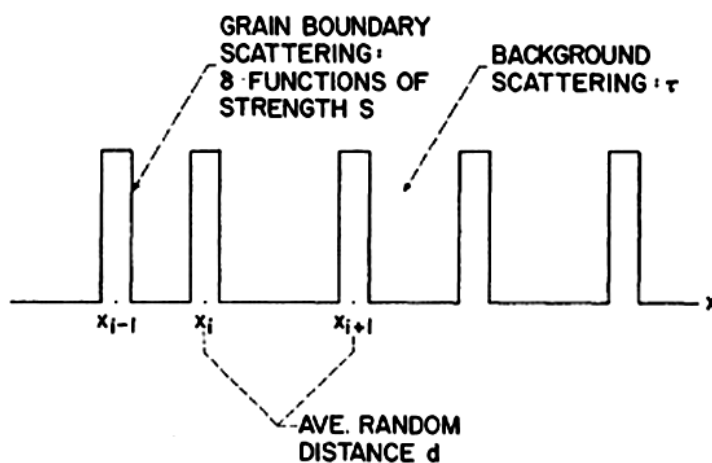

Figure 6.10 Grain boundary scattering representation in Mayadas-Shatzkes model

Clearly, in the TiN as well as the $TiN_{0.76}$ films the filamentary nature of current flow is due to the large reflection coefficients at the grain boundaries, leading to increased grain boundary scattering. Due to

this, electron transport across a grain boundary in the case of $TiN_{0.76}$ film is mainly due to tunneling. As a consequence, the number of percolation paths is low, the barrier for electron transport is high and therefore the total resistivity is high. For $Ti_{1-x}Nb_xN$ thin films, from figure 6.5, it is observed that the grain number density is high for TiN ($x=0$) film. As a consequence, it has more grain boundaries that contribute to electron scattering as compared to that for $Ti_{1-x}Nb_xN$ films. The probability of electron scattering from grain boundary is higher on TiN ($x=0$) film and is lower on $Ti_{1-x}Nb_xN$($x=0.77$) films. This argument is supported by figure 6.8 where it is seen that the local resistance of TiN ($x=0$) film having grain size 30 nm is higher than that the $Ti_{1-x}Nb_xN$ ($x=0.77$) film having grain size 90 nm. It is evident that a change in Nb concentration from 0.28 to 0.77 (roughly 2.75 times) causes less than one order of magnitude change in the resistance (figure 6.1). In contrast increase in grain size from 30 to 90 nm leads to more than two orders of magnitude decrease in the local resistance (figure 6.8). The local variations in resistance can thus be correlated with microstructural variations in the Nb substituted films rather than the variation in Nb concentration. From the figure 6.7, it is evident that the I-V characteristics of the film are not similar, even the point taken on the grain interior of respective film. Adjacent grains with equal size and height have different electrical interaction (strong or weak) depends on the grain boundary width and oxidation states present. These variations could lead to vary the local electrical characteristic of the films. Since the C-AFM measurements were performed at ambient atmosphere, it is possible to present a few nanometers native oxide states on the surface of the films. The variations in the oxidation states play a crucial role on the local electrical and

electron transport properties of the films [196]. The native oxide layer is act as a potential barrier for electron transport. In addition to the grain boundary scattering, local oxidation is also responsible for increase the local resistance.
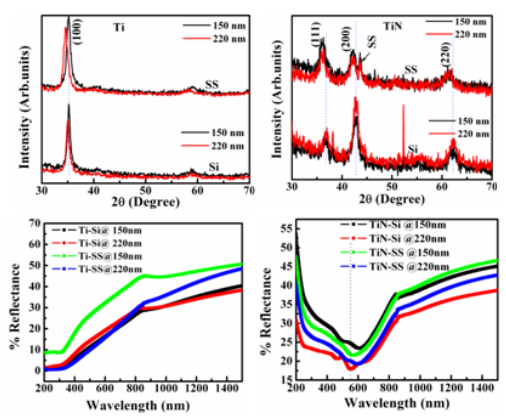
6.6 Summary

Microstructure dependent local electrical and electron transport properties in TiN_x and $Ti_{1-x}Nb_xN$ thin films studied by conductive atomic force microscopy. In both TiN_x and $Ti_{1-x}Nb_xN$ films the current flow on the surface is filamentary nature. Comparison between the topography and the current maps of TiN_x films of two compositions show that grains in stoichiometric TiN are electrically conductive but those of sub-stoichiometric $TiN_{0.76}$ film are electrically resistive. While in $Ti_{1-x}Nb_xN$ films current map on the surface of the films is varying according to the microstructure. Current on the grain interior is higher than the grain boundary and grain boundaries are act as potential barrier for electron transport. An examination of the I-V characteristics demonstrated that for TiN the I-V curve is almost linear (as for a metal), but for the sub-stoichiometric $TiN_{0.76}$ film, the I-V curve is non linear, which indicates the presence of a high barrier for electron transport across grain boundaries. I-V characteristic of $Ti_{1-x}Nb_xN$ thin films exhibits linear variation indicate that the Ohmic contact between tip and films. Local resistance of TiN_x and $Ti_{1-x}Nb_xN$ films is increased several orders of magnitude as compare to the total resistance. Microscopic electron scattering from the grain boundary and the presence of native oxide layer on the surface is giving rise to the macroscopic resistance.

CHAPTER-7

SUMMARY AND SCOPE FOR FUTURE WORK

7.1 Summary

Summarizing, the research presented in this dissertation is centered around the structure, microstructure, mechanical, optical and electrical properties of sub-stoichiometric and Nb-substituted titanium nitride thin films. The main object of the present thesis is demonstrate the multifunctional properties of TiN thin films in sub-stoichiometric and metal-substituted forms. Study the microstructure dependent local electrical and electron transport properties of these films is another aspect covered by this thesis. Films are deposited using RF magnetron sputtering on various substrates in 100% nitrogen plasma. The salient conclusions of the thesis with some of the representative figures from chapters-III, IV, V and VI are presented in the table given below.

Ti and TiN thin films	XRD pattern and optical reflectance spectra of metallic Ti and TiN thin films
1. Metallic Ti films crystallized into hexagonal structure with (100) orientation. The maximum values of hardness and Young's modulus for Ti thin films are 12 and 132 GPa, respectively. 2. TiN films crystallized into cubic structure with (111), (200) and (220) orientations and the highest values of hardness and Young's modulus are 27 and 250 GPa, respectively	

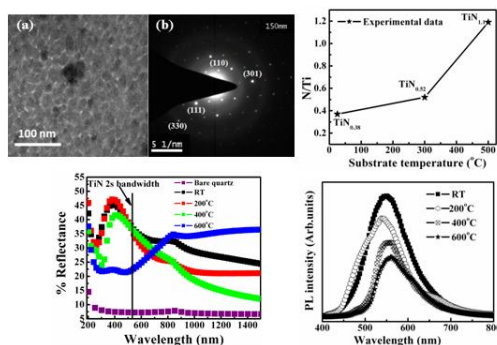| *TiN$_x$ thin films*	TEM (SAED) image of Ti$_2$N film, variation of N/Ti ratio with substrate temperature, PL spectra and reflectance spectra of TiN$_x$ thin films (Clockwise)
1. Substrate temperature dependent composition and structure change in TiN$_x$ thin films was observed. N/Ti ratio increased and the crystal structure changed from tetragonal Ti$_2$N to cubic TiN with increase in the substrate temperature. 2. The measured highest values of hardness and Young's modulus were 17.5±1GPa and 120±6 GPa for the film deposited at 600°C. 3. Optical reflectance minima of the films shifted from the ultra-violet region having energy of 4.83 eV to the visible region corresponding to energy of 2.47 eV 4. Films exhibited a single photoluminescence band in the middle of the visible region	

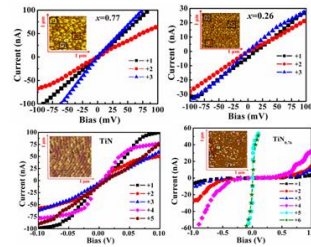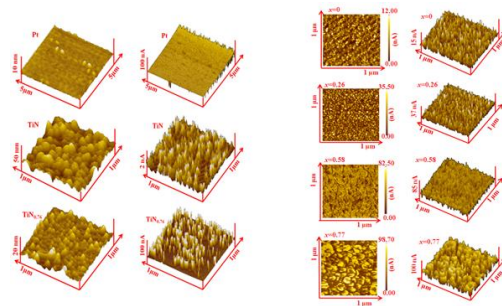|	
Ti₁₋ₓNbₓN thin films 1. X-ray diffraction studies of $Ti_{1-x}Nb_xN$ thin films revealed that the Nb is completely soluble in TiN and forms a stable ternary solid solution in cubic structure with (111) orientation. 2. The highest hardness achieved was 31GPa for x=0.77, at the same Nb concentration, the friction coefficient was 0.15 and the elastic recovery was 60%. 3. The real part of the dielectric function is characterized by screened plasma energy of 2.25 eV for values of x <0.5 and 3.2 ± 0.2 eV for x >0.5 4. The electrical resistivity of $Ti_{1-x}Nb_xN$ films decreased from 206 to 56 μΩ-cm as increase x from 0 to 0.77	XRD pattern, variation of hardness with x, real (a) and imaginary (b) parts of dielectric function and fitted reflectance spectra of $T_{i-x}Nb_xN$ films (Clockwise)
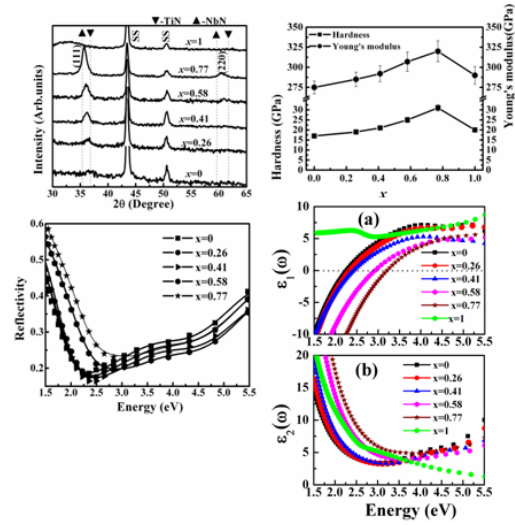
C-AFM study on TiN$_x$ and Ti$_{1-x}$Nb$_x$N films	3D current images and I-V characteristics of TiN, TiN$_{0.76}$ and Ti$_{1-x}$Nb$_x$N thin films (Clockwise)
1. C-AFM study on the surface of TiN$_x$ and Ti$_{1-x}$Nb$_x$N indicates that the grains in stoichiometric TiN are electrically conductive but those of sub-stoichiometric TiN$_{0.76}$ film are electrically resistive. In Ti$_{1-x}$Nb$_x$N films, current on the grain interior is higher than the grain boundary and grain boundaries act as potential barrier for electron transport. 2. The I-V characteristics of TiN film with grain size 73±12 nm is almost linear, but for the sub-stoichiometric TiN$_{0.76}$ film having grain size 50±5 nm, the I-V curve is non linear. 3. I-V characteristic of Ti$_{1-x}$Nb$_x$N thin films exhibits linear variation which indicates ohmic contact between tip and films.	

7.2 Scope for future work

There are many issues that still need to be resolved and could form part of future work

Ex situ annealing

The metallic Ti films exhibit a variety of microstructures which can be modified by *ex situ* annealing leading to change in their mechanical, optical and electrical properties. Annealing of $Ti_{1-x}Nb_xN$ thin films could also result in the change in structure, microstructure, mechanical, optical and electrical properties. Therefore, a study of the properties of Ti and $Ti_{1-x}Nb_xN$ thin films as a function of *ex situ* annealing temperature is a possible area for future work.

TiN/SiN and TiN/NbN multilayer

Nanostructured multilayer coatings of transition metal nitrides are an emerging class of superhard materials. These multilayers exhibit properties such as high hardness, wear resistance, high corrosion resistance and higher thermal stability. The properties exhibited by nanolayered multilayer coatings depend upon the modulation wavelength and nature of the interface structure which, in turn, can be tailored depending upon the choice, and layer thickness of the constituent materials and by judicious control of the deposition parameters. Nanocrystalline/amorphous TiN/Si_3N_4 multilayer films are one of the important candidates for next-generation materials in high temperature tribological applications. Similarly, TiN/NbN multilayer system is

technologically important since it is expected to have lower residual stresses apart from superior mechanical properties. These coatings exhibit hardness in the range 50-90 GPa, which is equal to the diamond hardness. Therefore, deposition and characterization of TiN/Si_3N_4 and TiN/NbN multilayers can be taken up in future.

Kelvin Force Microscopy (KFM)

Using conductive atomic force microscopy, the local electrical and electron transport properties of TiN_x and $Ti_{1-x}Nb_xN$ films were successfully studied. Kelvin force microscopy (KFM) is extensively used to map the local surface potential of metallic and semiconductor thin films. It is also possible to measure local work function of the surfaces at nanometer length scale. Therefore, measurement of the surface potential and work function of TiN_x and $Ti_{1-x}Nb_xN$ films using KFM could form another area of future work.

List of Publications relevant to this thesis

1. K.Vasu, M.S.R.N.Kiran, M.Ghanashyam Krishna, K.A.Padmanabhan
   "Effect of substrate on the crystallographic texture and microstructure evolution in titanium nitride thin films" *Proceedings of the DAE-SSPS-2008, 53 (2008) 681*

2. K.Vasu, M.Ghanashyam Krishna, K.A.Padmanabhan
   "Substrate temperature dependent structure and composition variations in RF sputtered titanium nitride thin film" *Appl. Surf. Sci.* **257** (2011)3069-3074

3. K.Vasu, M.Ghanashyam Krishna, K.A.Padmanabhan
   "Conductive atomic force microscopy study of local electron transport in nanostructured titanium nitride thin films" *Thin Solid Films* **519** (2011) 7702-7706

4. K.Vasu, M.Ghanashyam Krishna, K.A.Padmanabhan
   "Effect of Nb concentration on the structure, mechanical, optical and electrical properties of nanocrystalline $Ti_{1-x}Nb_xN$ thin films" *J. Mater. Sci.* **47** *(2012)* 3522

5. K.Vasu, G.M.Gopikrishnan, M.Ghanashyam Krishna, K.A.Padmanabhan
   "Optical and electronic properties of $Ti_{1-x}Nb_xN$ thin films" AIP. Conf. Proc.**1447** (2012) xxxx

6. K.Vasu, M.Ghanashyam Krishna, K.A.Padmanabhan
   "**Nanomechanical and nanotribological properties of Nb substituted TiN thin films"** AIP. Conf. Proc.**1451** (2012) xxxx

7. K.Vasu, G.M.Gopikrishnan, M.Ghanashyam Krishna, K.A.Padmanabhan
   "Reflectance, dielectric function and phonon-vibrational modes of reactively sputtered Nb substituted TiN thin filsms" (2012) (Under review)

8. K.Vasu, M.Ghanashyam Krishna, K.A.Padmanabhan

"Microstructure dependent local electrical and electron transport properties of Ti$_{1-x}$Nb$_x$N thin films" (2012) (Under review)